NMR of Dilute Sites in GaAs

Thesis by

Jack Yanchai Hwang

In Partial Fulfillment of the Requirements

for the Degree of

Doctor of Philosophy

California Institute of Technology

Pasadena, California

1994

(Submitted January 6, 1994)

Acknowledgements

I would like to thank my advisor Professor Dan Weitekamp for his support. None of this would have been possible without him. His enthusiasm and imagination has made the last few years an exciting experience I will not forget. I have had the good fortune to have many collaborations with my fellow group members. I would like to thank Herman Cho, David Shykind, Steve Buratto, John Marohn, Paul Carson and Michael Miller. Special thanks goes to David Shykind who has generously provided our lab with his technical expertise, and Paul Carson for his heroic efforts at proofreading my thesis over the Christmas holiday. I would also like to thank Dr. Frank Grunthaner of the JPL Microdevices Laboratory for providing us with GaAs samples and his advice.

What I enjoyed most was the sense of camaraderie in the Weitekamp group. The enthusiasm of the group members to help each other has made the subbasement a fun place to work. I will always remember everything from the Lucky Boy lunches to the group ski trips at Mt. Baldy. The group members and their families have also made life fun outside lab: David Shykind and Maria Giorgi (see you in Portland!), Pedro Pizarro and Monica Kohler, Paul Carson, John Marohn, Len and Shelley Mueller, Steve and Laura Buratto, Herman Cho, Narayanan (K.D.) Kurur, Dan Jones, Margat and Charlie Werner, Garett Leskowitz and Mike and Arezoo Miller. I would also like to thank the current and past members of the Zewail group for making the subbasement of Noyes a great place to be.

There are many people whose support and friendship over the past years has enriched my life at Caltech. I would like to thank Öjvind Bernander for being a great friend who has put up with me as a roomate for all these years and for sharing all the wonderful meals we have had with John Morris and Josée Morissette. Special thanks goes to Stew Fisher for his frienship and ski adventures, in addition to the the rest of the Caltech Backcountry Ski Club: Sakae Suzuki, Chris Kenyon and Peter Green. Pierre de la Noue has been a great friend and travel companion who has provided me with numerous breaks from my studies. I would like to thank Tom Zewert for his friendship and for being a great tennis partner. I would also like to thank Alex Ridgway, Tom O'Neill and Eric Belz, my Berkeley classmates who all came to Caltech for graduate school. Finally, I would like to acknowledge my late classmate Louis Boschelli who passed away in my third year at Caltech. He was a great friend who provided me with inspiration. I will always remember him for his great sense of humor.

I would express my gratitude to Dr. Donald C. Hofer of the IBM Research Center, my undergraduate research advisor, and Dr. Charles "Buddy" Mullins. These two people were instrumental in providing me with guidance at the beginning of my scientific career.

Finally, none of this would have been possible were it not for the love and encouragement of my parents. Their efforts and sacrifices have allowed me to obtain an outstanding education. This thesis is dedicated to them. I would also like to thank my sister Julie Hwang for her love and support, and her husband Kenny Lieuw for his friendship.

Abstract

The presence of a point defect in the zincblende lattice of GaAs breaks the tetrahedral symmetry and induces a range of quadrupole splittings into the NMR spectra of the surrounding Ga and As sites (all spin 3/2). Two-dimensional NMR nutation experiments are used to observe the resulting resonances in the case of an isovalent dopant. Differences in the nutation frequency of resonances near the unperturbed Zeeman frequency allow separation of the contributions from sites with large and small electric field gradients. Rotation studies allow the determination of field gradient tensor components in the crystal frame and provide clues to the assignment to specific sites. The inability to observe the NMR of the indium dopant at a concentration of $1 \times 10^{20}/\mathrm{cm}^3$ highlights the insensitivity of conventional NMR to the study of defects found at the concentrations present in device quality materials or to the low number of sites present at a single-crystal surface or interface.

Optical nuclear polarization (ONP) and optical detection (OD) of nuclear magnetic resonance (NMR) in III-V semiconductors have proven to be effective methods for increasing the sensitivity of NMR over that of conventional methods. The combination of ONP and OD into one optical NMR experiment has led to sensitivity enhancements of at least 10^5 in several GaAs-based materials. The quasi steady-state optically detected NMR (ODNMR) method used in all of these studies has resulted in NMR lineshapes which were either distorted by the high rf fields needed to see signals or broadened by the presence of spin-polarized electrons during NMR. The previous introduction of time-sequenced optical NMR (TSONMR) by the Weitekamp group, in which ONP, NMR, and OD occur in successive periods and are thus separately optimizable, has allowed the full implementation of multiple-pulse NMR. Several such methods are demonstrated on sub-ppm donor sites in epitaxial p-GaAs. These results

suggest that TSONMR may contribute to defect identification at sensitivities of technological relevance.

In conventional rf-detected Fourier transform (FT) NMR, the entire dipole-allowed spectrum is obtained from a single free induction decay. In contrast, FT time-sequenced optical NMR methods have necessarily been pointwise methods in which a period of coherent NMR evolution is incremented on successive repetitions to map out the desired interferogram. This method has the disadvantage, relative to ordinary NMR, that even simple experiments are time-consuming and susceptible to signal drift, giving rise to t_1 noise. This restriction has now been lifted by introducing a circularly-polarized transverse rf reference field so that the magnitude of the vector sum field (reference plus nuclear field of interest) is modulated at the difference frequencies of its Fourier components. The circular polarization of the luminescence is thus likewise modulated, due to the Hanle effect. This method allows real-time collection of NMR transients. To simultaneously optimize sensitivity and linearity, it is desirable to have a reference field which is larger than the signal field and comparable to the total longitudinal field. This is achieved by tuning the frequency of the applied reference field into resonance with one isotope so that the spin-locked nuclear hyperfine field, which can be orders of magnitude larger than practical applied rf fields, becomes the effective reference field. The circularly polarized luminescence signals at the difference frequencies are demodulated by a heterodyne rf spectrometer and digitized.

Table of Contents

List of Figures

Chapter 1

Chapter 2

Chapter 3

Chapter 4

Chapter 5

List of Tables

Chapter 2

Chapter 4

Chapter 1: Overview

1.1 Introduction

One of the fundamental problems of semiconductor physics is the identification and characterization of defects and epitaxial structures which determine the material's electronic and optical properties. Nuclear magnetic resonance (NMR) is nondestructive and capable of the chemical discrimination and generality needed to identify these structures. Since the three principal isotopes in GaAs all possess electric quadrupole moments, the quadrupole perturbation of the NMR spectrum provides a powerful probe for studying defects, in addition to the more familiar shifts in Zeeman energy. The GaAs lattice is a zinc-blende lattice which can be thought of as two interpenetrating face center cubic (FCC) lattices with the symmetry of the tetrahedral group (figure 1). The properties of the electric field gradient require the quadrupole interaction to vanish at all unperturbed sites since these have tetrahedral symmetry. With the introduction of defects or interfaces, the reduced symmetry results in electric field gradients (EFG's) which are fixed relative to the crystal frame. The interaction of these gradients with the nuclear quadrupole moment shifts the site specific NMR lines, allowing the determinaton of EFG's.

The magnitude of quadrupole coupling in the cases of most interest ($\approx 10^4 - 10^7$ Hz) are much larger than chemical shifts and spin-spin couplings, but smaller than the Zeeman interaction of the nuclear magnetic moment with typical high (> 1 T) applied fields. For spin 3/2 nuclei, a typical quadrupole spectrum, to first order, is a symmetric shift of the outer satellites with an unshifted central transition. Often, the satellites are unobservable because they lie outside the bandwidth for the rf excitation. For these large quadrupole interactions, second-order shifts of the central transition are often observable. The resulting observed spectrum in a sample with a distribution of quadrupole coupling will be a superposition of these, in addition to the full spectrum of weakly perturbed nuclei (figure 2).

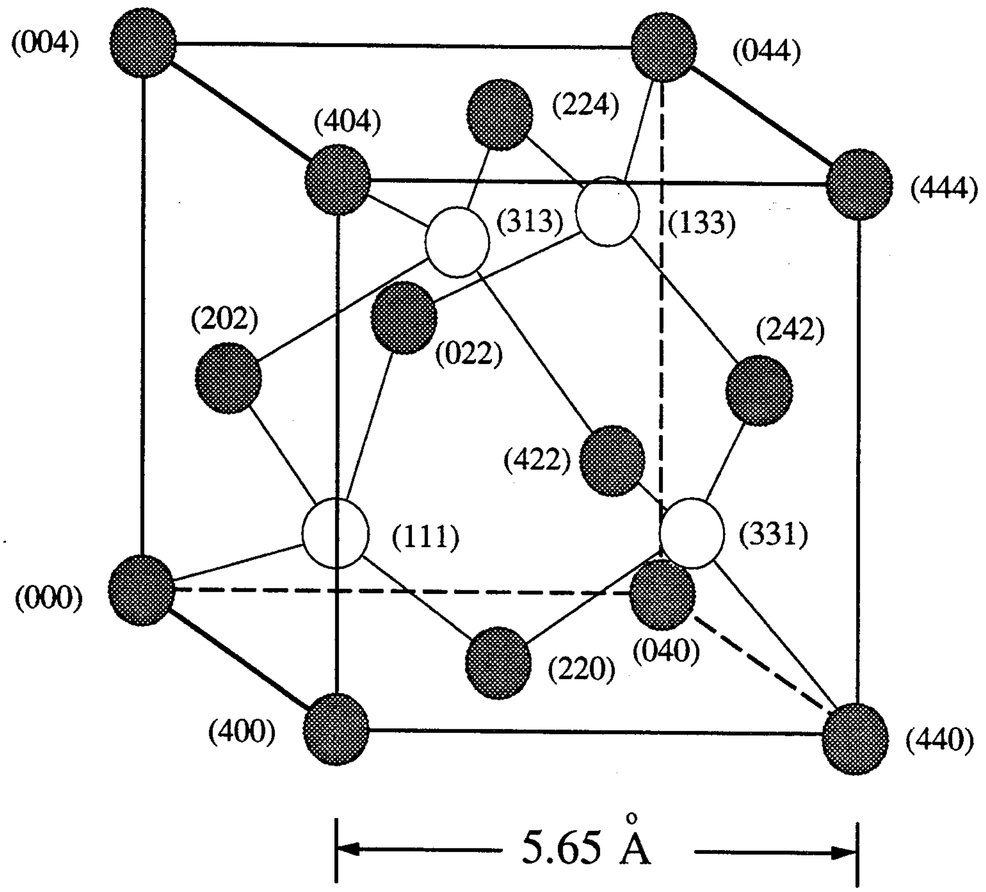

Figure 1. The GaAs lattice. The numbers are the lattice site coordinates.

Unfortunately, ordinary NMR is too insensitive to be applied to the study of defects found at the concentrations present in device quality materials or to the low number of sites present at a single-crystal surface or interface. Defect concentrations of 1 ppm.($\leq 10^{16}$/cm^3) can affect the optical properties of materials [1]. Current molecular beam epitaxy (MBE) growth techniques are able to control the growth of thin films down to a fraction of a monolayer. These new materials have properties not found in the bulk phase [2]. These properties arise from the localization of the conduction band electrons to dimensions comparable to their deBroglie wavelengths. State-of-the-art transmission electron microscopy images have a resolution of approximately 1.5 Å [3], which provides 1 atomic resolution, but this data contains limited chemical information. New

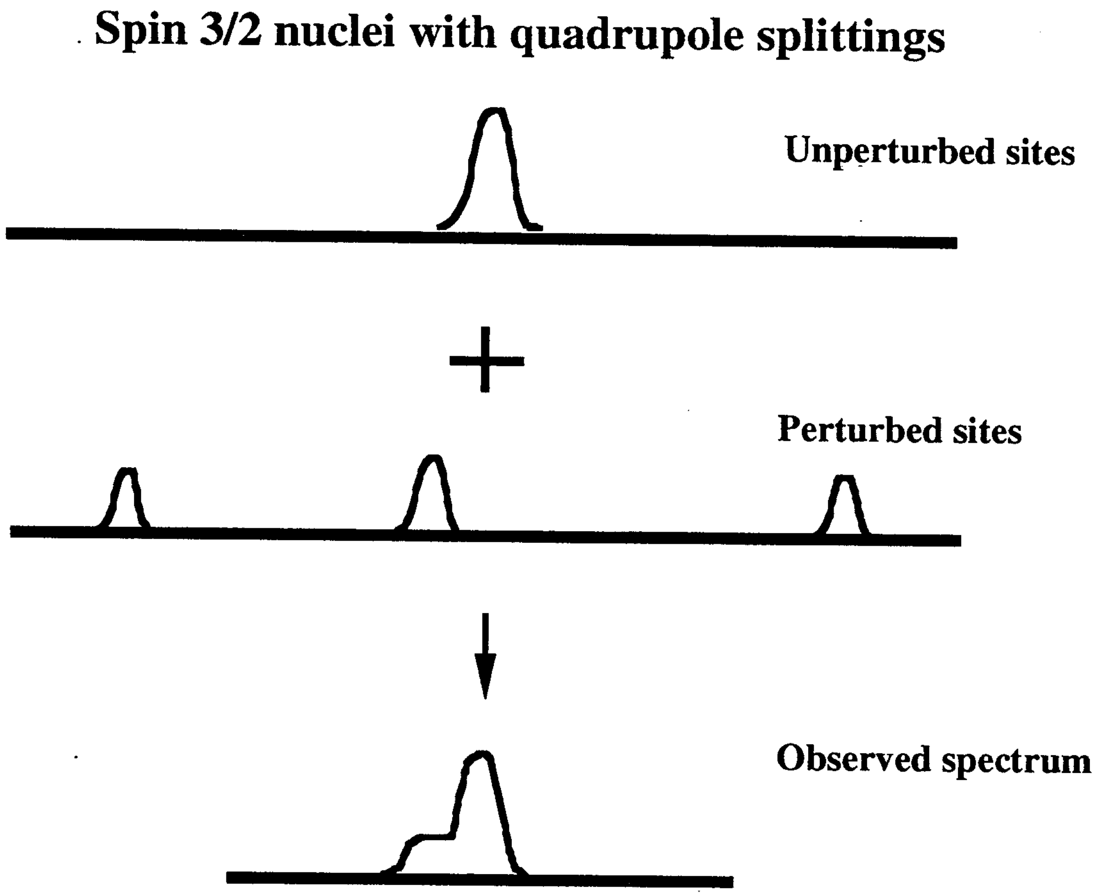

Figure 2. The NMR spectrum of GaAs in the presence of a high concentration of defects. The resulting spectrum is the superposition of spectra from perturbed and unperturbed sites.

spectroscopic techniques are needed to characterize the finer details of electronic and atomic structure.

Optical nuclear polarization (ONP) [4] and optical detection (OD) of nuclear magnetic resonance (NMR) in III-V semiconductors [5] have proven to be effective methods for increasing the sensitivity of NMR over that of conventional methods [6]. These two processes address the fundamental problems responsible for the low sensitivity of conventional NMR: the small population difference between nuclear spin levels and the difficulty in detecting radiofrequency photons above the thermal noise. Figure 3 illustrates the acquisition of an ODNMR spectrum. The sample is first irradiated with

Page 5 is nonexistent.

circularly polarized light near the bandgap which generates spin-polarized photoelectrons, which can polarize the nuclei. The electron-nuclear system is a tightly coupled system so when a radio frequency (rf) field is swept through the resonance frequencies of the nuclei, the electron polarization "feels" the state of nuclear polarization. The NMR can be seen by monitoring the polarization of the emitted light, which is a direct measure of the electron spin polarization.

The combination of ONP and OD into one optical NMR experiment has led to sensitivity enhancements of at least 10^5 in several GaAs-based materials such as epitaxially grown $Ga_{1-x}Al_xAs$ [5] and GaAs [7], as well as $GaAs/Ga_{1-x}Al_xAs$ [8] heterojunctions and quantum wells [9,10]. Over the past 25 years, through the efforts of groups at the A.F. Ioffe Physico-Technical Institute in St. Petersburg, Russia, and at the Ecole Polytechnique in Paris, the mechanism of ODNMR has been worked out [6]. However, the quasi steady-state, optically detected NMR (ODNMR) method used in all of these studies has resulted in NMR line shapes which were either distorted by the high rf fields needed to see signals or broadened by the presence of spin- polarized electrons during NMR. The innovation of TSONMR by the Weitekamp group [11-13] in which the three processes of ONP, NMR and OD are separated into three distinct periods which can be separately optimized, allows for an unprecedented combination of optical sensitivity with the resolution of modern time-domain multiple pulse NMR experiments. In ordinary FT-NMR experiments, the entire dipole-allowed spectrum is obtained from a single free induction decay. In contrast, FT-time-sequenced NMR involves the point-wise acquisition of the NMR transient through successive experiments. The key innovation which lifts this restriction and allows for the real-time optical detection of NMR has been accomplished, and real-time optically detected NMR signals have been observed in GaAs.

1.2 Outline

The manufacture of electronic grade single crystals of GaAs is difficult because of the formation of dislocations. These defects can have an adverse effect on the electrical and optical properties of the crystal. It has been found that the addition of In to the crystal in high concentrations ($\leq 10^{20}$) as an isovalent dopant leads to a significant decrease in the dislocation density [14] while maintaining the semi-insulating properties of the material. Indium is known to be an isoelectronic dopant, substituting at sites normally occupied by gallium [15]. The reduction in the symmetry for sites in the neighborhood of the dopant are manifested in the NMR spectrum as quadrupole perturbations of the NMR lines. Unfortunately, the overlapping signals from different sites complicates the interpretation of the results [16].

Chapter 2 presents NMR nutation studies of lattice distortions in GaAs heavily doped with indium ($9 \times 10^{19}/\mathrm{cm}^3$ or one part in 250 of the Ga sites). These studies are complementary to previous NMR studies of indium doped GaAs in which well resolved second order shifts of the central transition were observed [16]. Based on the orientation dependence of the frequency shift, these signals have been assigned to the next nearest neighbors of indium. However, the resonance lines of perturbed sites were obscured by signals from the central transition attributed to unperturbed sites. A 2D NMR nutation experiment is shown to allow spectral separation by the size of the quadrupole interaction thereby yielding the distribution of quadrupole couplings, and hence the strain. This has aided in the assignment of the orientation and magnitude of the best-resolved EFG tensors, found to be different from those observed in previous investigations [16], and hypothesized to be due to a different site. The 2D experiments also conclusively determine that the broad underlying peak in the 1D NMR spectrum is attributable to first order satellites of a quasi-continuum of weakly perturbed sites. Although this experiment gives good discrimination of the chemical environment, it is insensitive. The indium doping concentration is $10^{20}/\mathrm{cm}^3$, but the indium was unobservable at 4.7 Tesla. This provided the impetus for pursuing the application of these NMR experiments in conjunction with ODNMR.

Chapter 3 reviews ODNMR theory and extensions of TSONMR [11] developed by the Weitekamp group. These developments have allowed order of magnitude increases in sensitivity over the ODNMR technique and have allowed the application of multiple-pulse NMR experiments to the study of GaAs [11,12,13,17]. TSONMR experiments are presented for several samples of GaAs. This work serves as the foundation for the goal of determining the electron wave function confined in a GaAs quantum well [17]. This work will be based on the accurate measurements of the optical Knight shift, which probes the photoelectron density at a nuclear position when the sample is irradiated with light. The normal NMR linewidths of GaAs do not allow the desired resolution so a 16-pulse multiple-pulse line-narrowing NMR experiment, SWW-16, originally developed by the Weitekamp group [18,19] for imaging of solids with rf gradients, will be used with the optical Knight shift replacing position in the field gradient as the source of line shift. The sequence SWW-16 eliminates all static contributions to NMR linewidth, but allows the possibility of selectively re-introducing interactions into the NMR spectrum by imposing a time-dependence to the interaction. This will be accomplished with pulses of laser light.

The application of these multiple-pulse line-narrowing NMR sequences requires high rf powers. However, at the low (0.1 T) fields which were implemented for the original TSONMR experiments, the high rf powers, needed for line narrowing, resulted in Rabi frequencies comparable to the Larmor frequency, and a breakdown of the rotating wave approximation. Exact calculation (P. Carson, personal communication) indicated that fields of ≥ 0.1 T would be adequate for line-narrowing to succeed and still allow the sensitivity advantages of relatively low fields for TSONMR. A new apparatus with superconducting magnets was thus constructed for experiments to be performed at liquid helium temperatures. The lower temperature also improves the ONP and OD processes for epitaxial structures.

Chapter 4 describes the development of the liquid helium ONMR spectrometer. In these experiments, the liquid helium is cooled to the λ-point, at which it becomes a superfluid, to eliminate light scattering by the boiling helium. The construction of the cryogenic NMR probe with superconducting magnets is documented along with details of the optical excitation and detection apparatus. The point-wise acquisition of NMR transients which is inherent in optimized TSONMR designs, has the disadvantage relative to ordinary NMR that even simple experiments are time-consuming and susceptible to signal drift, giving rise to t_1 noise. This inspired the development of real-time optically detected NMR in which the transients are acquired in a single shot. Chapter 5 presents the results of this new development and the theoretical foundations for the experiment. The technique is based on the addition of a circularly-polarized transverse rf reference field so that the magnitude of the vector sum field (reference plus signal) is modulated at the difference frequencies of its Fourier components [20]. Data will be presented on the experimental observation of these transients. This work will serve as the basis for the implementation of real-time optically detected FT-pulsed NMR for the study of semiconductor nanostructures.

1.3 References

[1] Spaeth, J.-M., Niklas, J.R., and Bartram, R.H., *Structural Analysis of Point Defects in Solids* (Springer-Verlag, Berlin Heidelberg, 1992).

[2] Esaki, L., *A Bird's-Eye View on the Evolution of Semiconductor Superlattices and Quantum Wells,* IEEE Journal of Quantum Electronics, **QE-22**, 56 (1986).

[3] Fisher, R.M., in *Proceedings of the 49th Annual Meeting of the Electron Microscopy Society of America, San Francisco,* edited by G. W. Bailey (San Francisco Press, Inc.), 500, 1991.

[4] Lampel, G., *Nuclear Dynamic Polarization by Optical Electronic Saturation and Optical Pumping in Semiconductors,* Phys. Rev. Lett., **20**, 491 (1968).

[5] Ekimov, A.I., and Safarov, V.I., *Optical electron-nuclear resonance in semiconductors,* JETP Letters, **15**, 319 (1972).

[6] *Optical Orientation*, edited by Meier, F., and Zakharchenya, B.P. (North-Holland, Amsterdam, 1984), Vol. 8.

[7] Paget, D., *Optical Detection of NMR in high-Purity GaAs Under Optical Pumping: Efficient Spin-Exchange Averaging Between Electronic States,* Phys. Rev. B, **24**, 3776 (1981).

[8] Krapf, M., Denninger, G., Pascher, H., Weimann, G., and Schlapp, W., *Optically Detected Nuclear Magnetic Resonance and Knight Shift in* $Al_xGa_{1-x}As/GaAs$ *Heterostructures,* Solid State Communications, **78**, 459 (1991).

[9] Flinn, G.P., Harley, R.T., Snelling, M.J., Tropper, A.C., and Kerr, T.M., *Optically detected nuclear magnetic resonance of nuclei within a quantum well,* Semicond. Sci. Technol., **5**, 533 (1990).

[10] Kalevich, V.K., Korenev, V.L., and Fedorova, O.M., *Optical Polarization of Nuclei in GaAs/AlGaAs Quantum Well Structures,* JETP Letters, **52**, 349 (1990).

[11] Buratto, S.K., Shykind, D.N., and Weitekamp, D.P., *Time-sequenced optical nuclear magnetic resonance of gallium arsenide,* Phys. Rev. B, **44**, 9035 (1991).

[12] Buratto, S.K., Hwang, J.Y., Kurur, N.D., Shykind, D.N., and Weitekamp, D.P., *Fourier-Transform Time-Sequenced Optical Nuclear Magnetic Resonance of Gallium Arsenide,* Bulletin of Magnetic Resonance, **15**, 190 (1993).

[13] Buratto, S.K., Hwang, J.Y., Kurur, N.D., Shykind, D.N., and Weitekamp, D.P., *Time-sequenced optical nuclear magnetic resonance of GaAs,* J. Chem. Phys., **to be submitted**, (1993).

[14] Jacob, G., Duseaux, M., Farges, J.P., Boom, M.M.B.v.d., and Roksnoer, P.J., *Dislocation-Free GaAs and InP Crystals by Isoelectronic Doping,* J. Cryst. Growth, **61**, 417 (1983).

[15] Mikkelsen, J.C., and Boyce, J.B., *Extended x-ray-absorption fine-structure study of* $Ga_{1-x}In_xAs$ *random solid solutions,* Phys. Rev. B, **28**, 7130 (1983).

[16] Carlos, W.E., Bishop, S.G., and Treacy, D.J., *Nuclear-magnetic-resonance studies of strain in isovalently doped GaAs,* Phys. Rev. B, **43**, 12512 (1991).

[17] Buratto, S.K., Shykind, D.N., and Weitekamp, D.P., *Can Nuclear Magnetic Resonance Resolve Epitaxial Layers?,* Journal of Vacuum Science and Technology B, **10**, 1740 (1992).

[18] Werner, M.H., NMR Imaging of Solids with Multiple Pulse Line Narrowing and Radiofrequency Gradients, 1993.

[19] Cho, H.M., Lee, C.J., Shykind, D.N., and Weitekamp, D.P., *Nutation Sequences for Magnetic Resonance Imaging in Solids,* Phys. Rev. Lett., **55**, 1923 (1985).

[20] Carson, P.J., Hwang, J.Y., Marohn, J.A., Miller, M.A., Shykind, D.N., and Weitekamp, D.P., *Larmor Frequency Modulation of Photon Polarization by Transverse Nuclear Magnetization in Gallium Arsenide.,* Bull. Am. Phys. Soc. (Abstract), (1994).

Chapter 2: Nutation NMR Studies of Isovalently Doped GaAs

The nutation experiment, originally proposed by Torrey [1], monitors the precession of the magnetization about the resonant radio frequency (rf) field. The resulting oscillatory transient contains interesting information in the case of quadrupolar nuclei. When only the central transition of a half-integral nucleus is effectively irradiated, as in the limit of large quadrupole couplings, the nutation frequency, ω_1, is equal to $(I+1/2)\ \omega_{rf}$ where I is the nuclear spin quantum number and ω_{rf} is the nutation frequency of the unperturbed nucleus [2]. At intermediate sizes of quadrupole couplings, the unequal excitation of the different transitions leads to several nutation frequencies. The Fourier transform of this spectrum provides information on the strength of the quadrupole interaction. Because of the sensitivity of the nutation experiment to the size of the quadrupole coupling, it is used in ^{75}As 2D NMR nutation experiments to separate the NMR spectra based on the size of quadrupole coupling. This chapter presents the results of 2D NMR nutation experiments on GaAs heavily doped with indium (a part per thousahd) to aid in the analysis of spectra due to a distribution of sites.

2.1 Introduction to In doped GaAs

Understanding how the lattice incorporates the isovalent dopants is an area of active interest. In the high-concentration regime, isovalent dopants such as Al in $Ga_{1-x}Al_xAs$ have been studied with x-ray Bragg scattering and have been found to have average lattice constants that varied linearly between that of GaAs and AlAs [3]. These results have led to the virtual-crystal approximation (VCA) in which all atoms, including the isovalent impurities, are thought to be located on sites in the average unit cell [4]. $Ga_{1-x}In_xAs$ has been found to exhibit this behavior [5], but because x-ray Bragg scattering measures average lattice spacing, these results may not be indicative of local effects. X-ray absorption fine structure (EXAFS) studies have been used to measure nearest neighbor and next nearest neighbor distances [6]. While next nearest neighbor

Ga-Ga distances were constant, and approximated the VCA model, the As-As distances possessed a bimodal distribution corresponding to bond lengths found in GaAs and InAs crystals. These results indicate that some lattice relaxation must be necessary to accommodate the different bond lengths. NMR is an ideal technique for the study of such a system since distortions from the ideal lattice give rise to electric field gradients (EFG), manifested by quadrupole splittings of the NMR lines. Carlos and co-workers studied a single crystal of GaAs highly doped with indium possessing well resolved NMR resonance lines, attributed to the next nearest neighbors surrounding an indium atom, separate from those of the bulk sites [7]. The NMR spectrum exhibited orientation dependence consistent with assignments to the next nearest neighbor arsenic atoms surrounding an indium atom.

Unfortunately, the orientation dependence of several sites could not be measured because the signals were obscured by the main resonance of the unperturbed sites. This data is necessary for more precise information about the symmetry of these sites. A 2D NMR nutation experiment can help to resolve the orientation dependence of these lines by separating them from the bulk unperturbed sites. This experiment is applied to a sample of GaAs highly doped with indium, similar to those of Carlos and co-workers. In this sample, well resolved resonances exhibiting correlated orientation dependence were observed and fitted to 12 chemically equivalent sites with a quadrupole coupling constant$\nu_q = 3e^2qQ/2I(2I-1)\,h = 0.9 \pm 0.1$ MHz and asymmetry parameter of $\eta = 0.0 \pm 0.2$. The discrepancy between these values and those of Carlos et al. ($\gamma_Q = 2.5$ MHz, $\eta = 0.2$) is explicable if the present experiment observes a site more distant from the indium center, but with the same symmetry properties. Interference effects between the signals from sites with different resonance frequency has led to uncertainty in the asymmetry parameter. Taking advantage of symmetry, the analysis of the rotation pattern was simplified by using group theory methods established in ENDOR studies of point-defects in silicon [8] to place constraints on the possible orientations of the tensor. The resulting

2D spectrum also resolves the continuum of first order quadrupole satellites from more distant As sites. These experiments show that a significant fraction of sites experience lattice distortion as measured by their quadrupole coupling.

2.2 The Quadrupole Interaction

The quadrupole interaction is a probe of defect structure because it is sensitive to electric field gradients resulting from distortions of the ideal lattice. In a magnetic field, the energy shift of the nuclear Zeeman states is due to the reorientation of an asymmetric nuclear charge distribution in an electric field gradient produced by distortions in the lattice. The quadrupole interaction is illustrated in figure 1 with the graphical representation of an elliptical positive charge distribution placed in the electric field gradient produced by four charges [9].

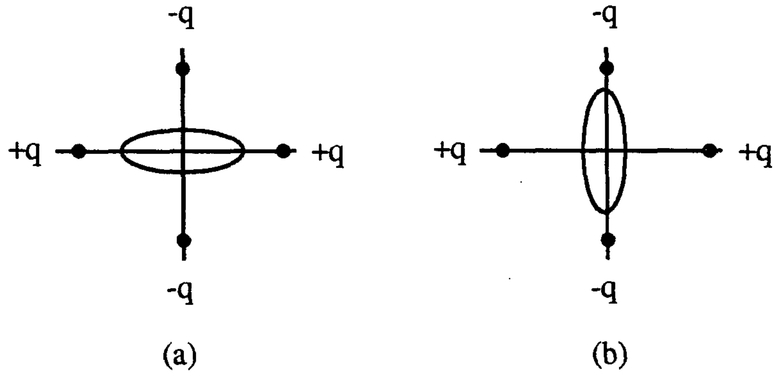

Figure 1. Illustration of a positively charged ellipse in a quadrupole field. The configuration in figure 1b is at a lower energy.

The quadrupole interaction does not cause a frequency shift for spin 1/2 (spherical charge distribution) because the inversion of the charges leaves the potential unchanged. For spins with $I > 1/2$, each spin state corresponds to a different orientation in the quadrupole field, resulting in unequal perturbations of the transition energies. These shifts can be large, in some instances approaching the Zeeman energy of nuclear transitions at high field. The three principal isotopes in GaAs ($I = 3/2$) all possess quadrupole moments. If $\underline{\underline{V}}$ is the electric field gradient tensor with components defined by equation (1)

$$V_{ij} = \left(\frac{\partial^2 V}{\partial x_i \partial x_j} \right) \tag{1}$$

then following the established convention [9,10], the quadrupole interaction may be uniquely characterized by the following parameters

$$\begin{aligned} V_{zz} &= eq \\ \eta &= \frac{V_{yy} - V_{xx}}{V_{zz}} \leq 1 \\ |V_{zz}| &> |V_{yy}| > |V_{xx}| \end{aligned} \tag{2}$$

here η is the asymmetry parameter, e is the charge on the electron, and q parametrizes the largest principal component of the electric field gradient [11]. Since $\mathrm{Tr}(\underline{\underline{V}}) = 0$, specifying the asymmetry parameter and the principal component eq uniquely determines the field gradient tensor.

The full quadrupole Hamiltonian is [9]

$$H_Q = \frac{eQ}{4I(2I-1)} \left[\begin{aligned} V_0\left(3I_z^2 - I^2\right) + V_{+1}\left(I_- I_z + I_z I_-\right) + V_{-1}\left(I_+ I_z + I_z I_+\right) + V_{+2}\left(I_-\right)^2 \\ + V_{-2}\left(I_+\right)^2 \end{aligned} \right] \tag{3}$$

where eQ is the nuclear electric quadrupole moment, known for any isotope, and

$$\begin{aligned} V_0 &= V_{zz} \\ V_{\pm 1} &= V_{zx} \pm i V_{zy} \\ V_{\pm 2} &= \frac{1}{2}\left(V_{xx} - V_{yy}\right) \pm i V_{xy} \end{aligned} \tag{4}$$

are the electric field gradient components expressed in the irreducible spherical tensor basis.

When the quadrupole interaction is much smaller than the Zeeman interaction and can thus be considered as a perturbation, the energy to second order is

$$E_n = E_n^0 + \langle \phi_n | H_Q | \phi_n \rangle + \sum_{p \neq n} \frac{\left| \langle \phi_p | H_Q | \phi_n \rangle \right|^2}{E_n^0 - E_p^0} + O(3) \tag{5}$$

where $|\phi_m\rangle = |I, m\rangle$ are the unperturbed Zeeman eigenstates with magnetic quantum number m and spin I.

The quadrupole Hamiltonian (eq. 3) is a product of spatial and spin terms. The spin matrix elements are calculated with the spin operators of Eq. 3:

$$\begin{aligned} &\langle m | \, 3I_z^2 - I^2 \, | m \rangle = \left[3m^2 - I(I+1) \right] \\ &\langle m \pm 1 | \, I_\pm I_z + I_z I_\pm | m \rangle = (2m \pm 1) \left[(j \mp m)(j \pm m + 1) \right]^{1/2} \\ &\langle m \pm 2 | \, I_\pm^2 | m \rangle = \left(\left[j(j+1) - (m \pm 1)(m \pm 2) \right] \left[j(j+1) - m(m \pm 1) \right] \right)^{1/2} \end{aligned} \tag{6}$$

Substitution of these matrix elements into equation 3 gives the energy to second order as

$$\begin{aligned} E_m = -m\gamma\hbar B + A\left[3m^2 - I(I+1)\right]V_0 + \frac{2A^2 V_{+1} V_{-1}}{\gamma\hbar B} m\left[4I(I+1) - 1 - 8m^2\right] \\ - \frac{2A^2 V_{+2} V_{-2}}{\gamma\hbar B} m\left[2I(I+1) - 1 - 2m^2\right] + O(3) \end{aligned} \tag{7}$$

where $A = \frac{eQ}{4I(2I-1)}$, γ is the gyromagnetic ratio, and B is the magnetic field.

The Zeeman energy levels illustrated in figure 2 show the effects of (a) no perturbation, (b) first order quadrupole shifts and (c) second order quadrupole shifts. When specifying the quadrupole coupling constant, care must be used because several different conventions exist. For this discussion, the definition of the quadrupole coupling constant in Hz as

$$\nu_Q = \frac{3eQV_0}{2I(2I-1)h} = \frac{6AV_0}{h} \tag{8}$$

is convenient because ν_Q is equal to the frequency shift of the first order satellite for nuclear spin $I = 3/2$.

The first and second order shifts are illustrated in figure 2. From an examination of the energies from the perturbation result (eq. 8), it can be seen that the first order shifts of the energy are even in magnetic quantum number. The ± 3/2 Zeeman states are both shifted upwards and the ± 1/2 Zeeman states both move downwards by equal amounts. Thus, the resulting spectrum has a central transition that is unshifted to first order, and two symmetric satellites. However, the central transition is shifted to second order.

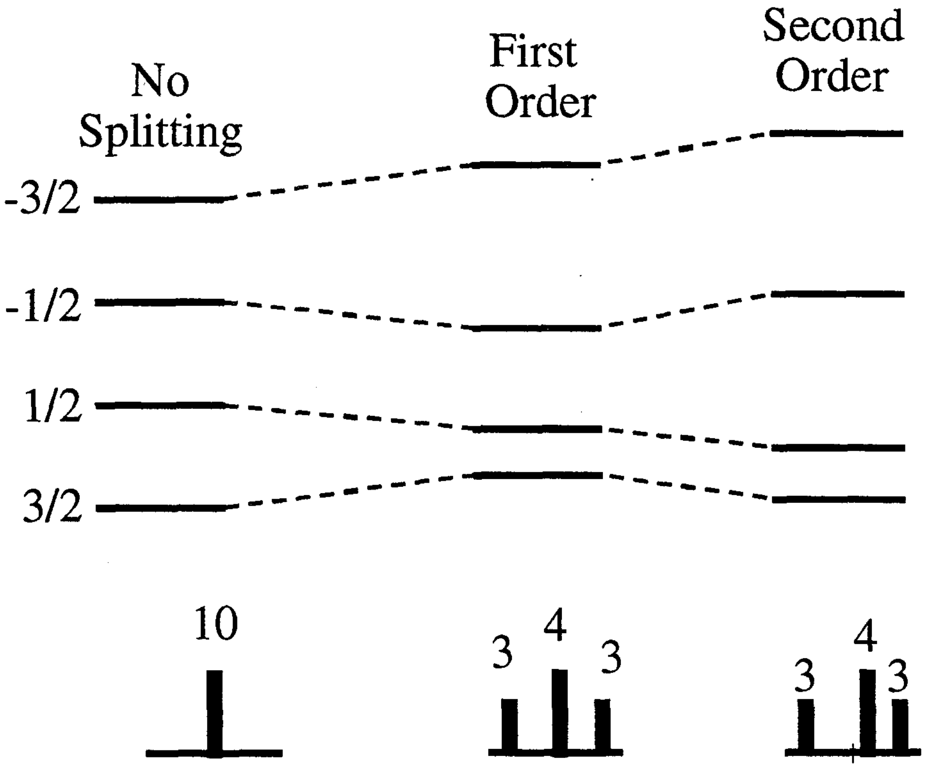

Figure 2. Energy level diagram for the quadrupole interaction of a spin 3/2. The numbers in the stick representation of the spectrum represent the relative intensities of the signals.

The spatial portion of the quadrupole interaction is determined by the orientation of the electric field gradient tensor (EFG) relative to the external magnetic field. By performing rotations of the sample along various axes, one can determine the symmetry of the EFG. The analysis reduces to determining the eigenvalues of the EFG tensor and the orientation of its PAS (principal axis system) (figure 3). If the EFG is expressed in the irreducible spherical tensor basis (eq. 4), whose elements transform like the spherical harmonics, rotations can be performed with the Wigner rotation matrices [11]. The rotation from the PAS *XYZ* to the lab system *xyz* requires the Euler angles α,β,γ.

$$V'_{kq} \equiv R(\alpha\beta\gamma)V_{kq}R^{-1}(\alpha\beta\gamma) \equiv \sum_{p=-k}^{+k} V_{kp}\, D^{(k)}_{pq}(\alpha\beta\gamma). \tag{9}$$

where the $D^{(k)}_{pq}$'s are the Wigner rotation matrices. The Euler angles α,β,γ are defined as follows: rotate the coordinate axes about the z axis by angle α followed by a rotation about the new y' axis by angle β, and then a rotation about the resulting z'' axis by γ. The EFG is a second rank tensor, so $k = 2$.

There are two conventions for performing rotations. It is important to make the distinction between an active and passive rotation. An active rotation is one in which the object is rotated about a fixed origin. Let $A(\alpha,\beta,\gamma)$ be the transformation matrix of the active rotation. The coordinate $\bar{r}$ in the original frame is related to $\bar{r}'$ in the transformed frame by

$$\bar{r}' = A(\alpha,\beta,\gamma)\,\bar{r} \tag{10}$$

If $M(\alpha)$ equals $A(\alpha,0,0) = A(0,0,\alpha)$ and $N(\beta) = A(0,\beta,0)$, then these rotations can be represented by the individual rotations about fixed axes

$$A(\alpha,\beta,\gamma) = M(\alpha)N(\beta)M(\gamma) \tag{11}$$

There is an isomorphism between the matrices of active rotations, G_A, and the active rotations about the different axes in space.

In a passive rotation, the coordinates are rotated while the object is fixed. The corresponding matrix operator is denoted as $P(\alpha,\beta,\gamma)$.

$$\bar{r}' = P(\alpha,\beta,\gamma)\,\bar{r} \tag{12}$$

$P(\alpha,\beta,\gamma)$ can also be expressed as a product of rotations about fixed axes

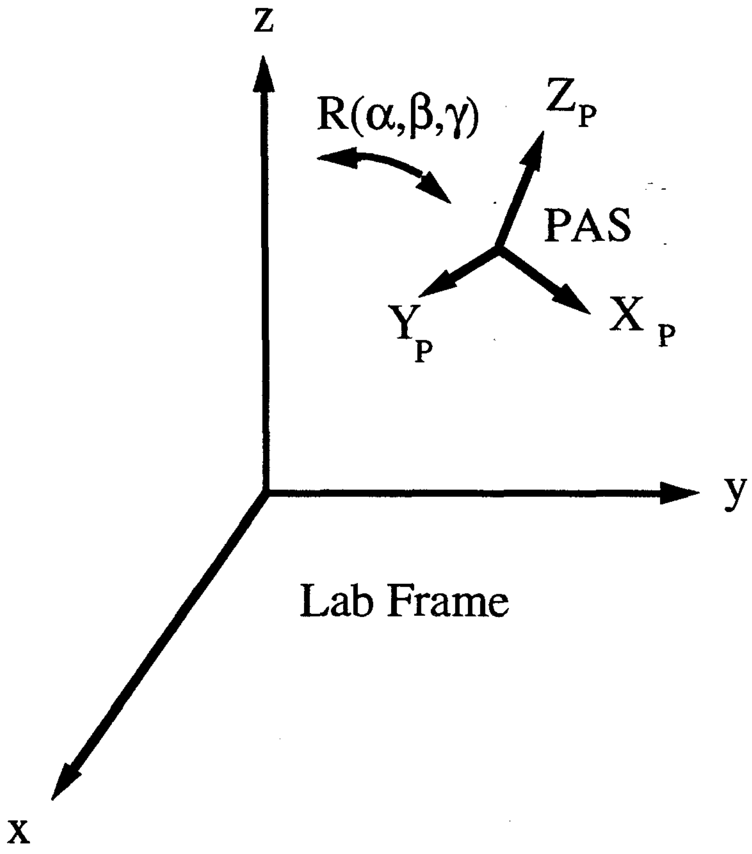

Figure 3. Transformation from the PAS to the lab frame. It is most convenient to express the tensor in the PAS frame, but in order to relate the tensor to an external magnetic field, the Euler angles α,β,γ are needed to perform the rotation from the PAS frame to the lab frame.

$$P(\alpha,\beta,\gamma) = M(-\gamma)N(-\beta)M(-\alpha) \tag{13}$$

In this rotation, the coordinate axes are not fixed, and no isomorphism exists between the matrices of passive rotations, G_P, and the passive rotations about different axes in space. In fact, an anti-isomorphism exists. For example, while

$$A(\alpha,0,0)A(0,\beta,\gamma) = A(\alpha,\beta,\gamma) \tag{14}$$

$$P(\alpha,0,0)P(0,\beta,\gamma) = P(0,\beta,\gamma+\alpha) \tag{15}$$

This subtlety is the cause of many errors in classic textbooks [12]. A simple relationship exists between the passive and active rotations (eq. 16).

$$P(\alpha,\beta,\gamma) = A(-\gamma, -\beta, -\alpha) = A^{-1}(\alpha,\beta,\gamma) \tag{16}$$

For the calculations used in this chapter, passive rotations are used. In the experiment, the sample is held by a goniometer and rotated relative to the magnetic field. The transformation of the EFG tensor from the PAS frame to the lab frame takes place in three steps as indicated in fig. 4.

$$\begin{tikzcd} \begin{array}{c}\tilde{A}''\\ (X,Y,Z)\\ \text{PAS}\end{array} \arrow[r, "R''(\alpha'',\beta'',\gamma')"] & \begin{array}{c}\tilde{A}^{*}\\ (a,b,c)\\ \text{CRS}\end{array} \arrow[r, "R^{*}(\alpha*,\beta*,\gamma*)"] & \begin{array}{c}\tilde{A}\\ (x_g,y_g,y_g)\\ \text{goniometer}\\ \text{Frame}\end{array} \arrow[r, "R_g(\alpha,\beta,\gamma)"] & \begin{array}{c}\tilde{A}'\\ (x,y,z)\\ \text{LAB}\end{array} \end{tikzcd}$$

Figure 4. Rotation sequence to transform from the PAS to CRS (crystal) to lab frame.

The sequential rotations can be combined into a single composite rotation

$$R_{\text{total}} = R_g(\alpha,\beta,\gamma)R^*(\alpha*,\beta*,\gamma*)R''(\alpha'',\beta'',\gamma') \tag{17}$$

These composite rotations are used in simulations of the rotation patterns. In order to generate the rotation pattern from all sites related by symmetry operations, the specification of the Euler angles for all the sites would be cumbersome. Using the group operations on the EFG is a far easier method for generating the EFG for all sites. The following section will describe the approach to be used.

2.3 Application of Symmetry to Rotation Patterns

GaAs possesses a zincblende structure which can be viewed as two interpenetrating face centered cubic (fcc) structures of gallium and arsenide ions (figure 5). Each site of the lattice possesses tetrahedral symmetry (T_d), a subset of the cubic group, and thus lacks inversion symmetry. The tetrahedral group possesses 24 elements. Permutation of the axes leaves the lattice unchanged, and, as a consequence of the Laplace equation for electrostatic potential, the electric field gradients are equal to zero at every site in the lattice. In the presence of defects, however, this symmetry is broken and the electric field gradients may differ from zero.

The symmetry property of GaAs allows the generation of the EFG tensor at chemically equivalent sites around a substitutional point defect (taken as the origin) of related symmetry once its value is known at one site. The EFG tensor can be represented by a 3×3 matrix. Let V_{ij} be the electric field gradient tensor components of a particular site. To represent this tensor, there are 3 principal axis components and 3 Euler angles with the condition that the tensor is traceless, i.e., Tr $(\underline{\underline{V}}) = 0$, due to property of the electric fields in the absence of charges. The resulting tensor possesses 5 degrees of freedom. By applying the rotation

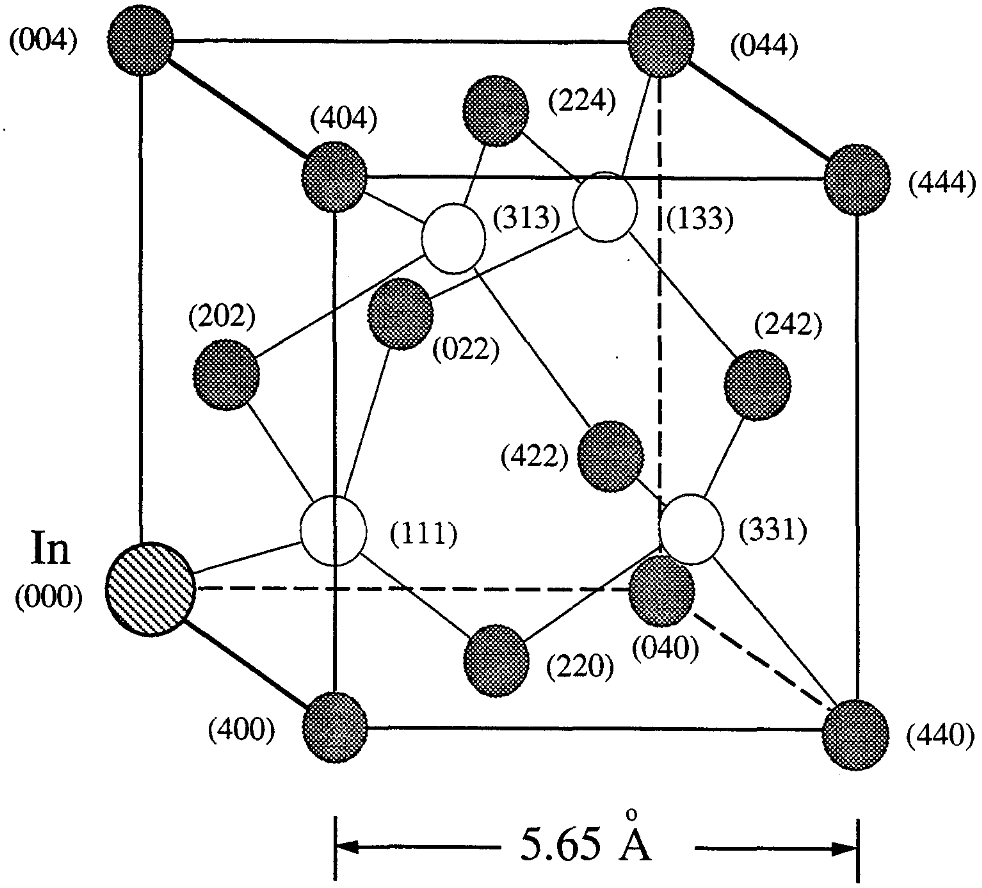

Figure 5. The GaAs lattice is composed of two interpenetrating face centered cubic lattices (fcc). The numbers specify the coordinates of sites relative to the origin (0, 0, 0).

operators corresponding to the elements of the tetrahedral group to a quantity related to one site, up to 23 distinct symmetry-related quantities can be generated. The distinct occupied sites generated in this way will be a set of 24 or fewer atoms, called a shell, which are equidistant from the origin. Equating the EFG tensor resulting from the operations of two different elements of the tetrahedral group will place restrictions on the elements of the EFG, and hence, the degrees of freedom. This will place restrictions on the possible orientation of the principal axes. For sites with the highest symmetry, the principal axes are uniquely determined.

Based on symmetry, an analysis of sites surrounding an isovalent dopant allows for only five classes (irreducible representations) of shells (Table 1) [8]. The following discussion will determine the constraints on possible orientation of the electric field gradient tensor that may be used for both gallium and arsenic.

Class	Number of distinct sites	Symmetry
1	24	Unique Class
2	12	(110) Plane Class
3	4	[111] Axis Class
4	6	[001] Axis Class
5	1	Origin

Table 1. The five classes of possible shells around a site with tetrahedral symmetry.

The tetrahedral group consists of 24 operations grouped into five classes consisting of E, the identity operator, C_3, a 120° rotation about a [111]-type axis, C_2, a 180° rotation about a [100]-type cube axis, σ_d, a reflection in a (110)-type plane, and S_4, a 90° rotation about a [110]-type axis followed by reflection about the plane perpendicular to the rotation axis. The elements of the group are listed in Table 2.

The EFG tensor possesses 5 independent components when there are no restrictions on the orientation of the principal axes. The elements V_{ij} will transform as the product ij. By finding the eigenvectors of the resulting matrix, restrictions may be

Number	Class	[Rotation Axis] or (Reflection Plane)	xyz->
1	E		x, y, z
2	C_3	[111]	z, x, y
3	C_3	[$\bar{1}\bar{1}\bar{1}$]	y, z, x
4	C_3	[$\bar{1}11$]	$-y, z, -x$
5	C_3	[$1\bar{1}\bar{1}$]	$-z, -x, y$
6	C_3	[$1\bar{1}1$]	$-y, -z, x$
7	C_3	[$\bar{1}1\bar{1}$]	$z, -x, -y$
8	C_3	[$\bar{1}\bar{1}1$]	$-z, x, -y$
9	C_3	[$11\bar{1}$]	$y, -z, -x$
10	C_2	[100]	$x, -y, -z$
11	C_2	[010]	$-x, y, -z$
12	C_2	[001]	$-x, -y, z$
13	σ_d	(110)	$-y, -x, z$
14	σ_d	($1\bar{1}0$)	y, x, z
15	σ_d	(101)	$-z, y, -x$
16	σ_d	($10\bar{1}$)	z, y, x
17	σ_d	(011)	$x, -z, -y$
18	σ_d	($01\bar{1}$)	x, z, y
19	S_4	[$\bar{1}00$]	$-x, z, -y$
20	S_4	[100]	$-x, -z, y$
21	S_4	[010]	$z, -y, -x$
22	S_4	[$0\bar{1}0$]	$-z, -y, x$
23	S_4	[$00\bar{1}$]	$y, -x, -z$
24	S_4	[001]	$-y, x, -z$

Table 2. The elements of the tetrahedral group [8].

placed on the possible orientation of the principal axes. The following summarizes the restrictions on the orientation of the principal axes for the 5 possible classes.

Class 1: These sites do not possess additional symmetry so no additional constraints are placed on the EFG. For class 1 sites, the EFG tensor has 5 independent components.

Class 2: (110) plane sites.

These sites possess mirror planes about the (110) planes. For example, a σ_d about $(1\bar{1}0)$ will transform xyz to yxz, leaving the EFG tensor unchanged so that $V_{xx} = V_{yy}$, $V_{xz} = V_{yz}$. The resulting tensor can be put into block diagonal form and diagonalized by rotating the coordinates about the z axis by 45 degrees and has the form

$$\underset{\approx}{V} = \begin{pmatrix} V_{xx}+V_{xy} & 0 & 2V_{xz} \\ 0 & V_{xx}-V_{xy} & 0 \\ V_{xz} & 0 & -2V_{xx} \end{pmatrix} \tag{19}$$

For a site on the (110) plane, one principal axis lies along the [110] axis with no restrictions on the other two axes (figure 6).

Class 3: [111] axis sites

These sites possess symmetry about a [111] axis. A C_3 rotation about such an axis will leave these sites invariant. This permutation of $xyz \rightarrow zxy$ results in setting $V_{xx} = V_{yy} = V_{zz} = 0$, and $V_{xy} = V_{xz} = V_{yz}$. Thus the EFG tensor has the form

$$\underset{\approx}{V} = V_{xy}\begin{pmatrix} 0 & 1 & 1 \\ 1 & 0 & 1 \\ 1 & 1 & 0 \end{pmatrix} \tag{20}$$

There is one principal axis along the [111] axis, and the two orthogonal axes are equivalent principal axes (figure 7).

Class 4: [001] axis sites

These sites possess C_2 symmetry about the [001] axis. A C_2 rotation about the [001] axis gives $xyz \rightarrow -x-yz$ so that $V_{xz} = -V_{xz} = 0$ and $V_{yz} = -V_{yz} = 0$. Thus

$$\underset{\approx}{V} = \begin{pmatrix} V_{xx} & V_{xy} & 0 \\ V_{xy} & V_{yy} & 0 \\ 0 & 0 & -(V_{xx} + V_{yy}) \end{pmatrix}. \tag{21}$$

There is one principal axis along the [001] axis with other 2 axes along the (110) mirror planes (fig. 8).

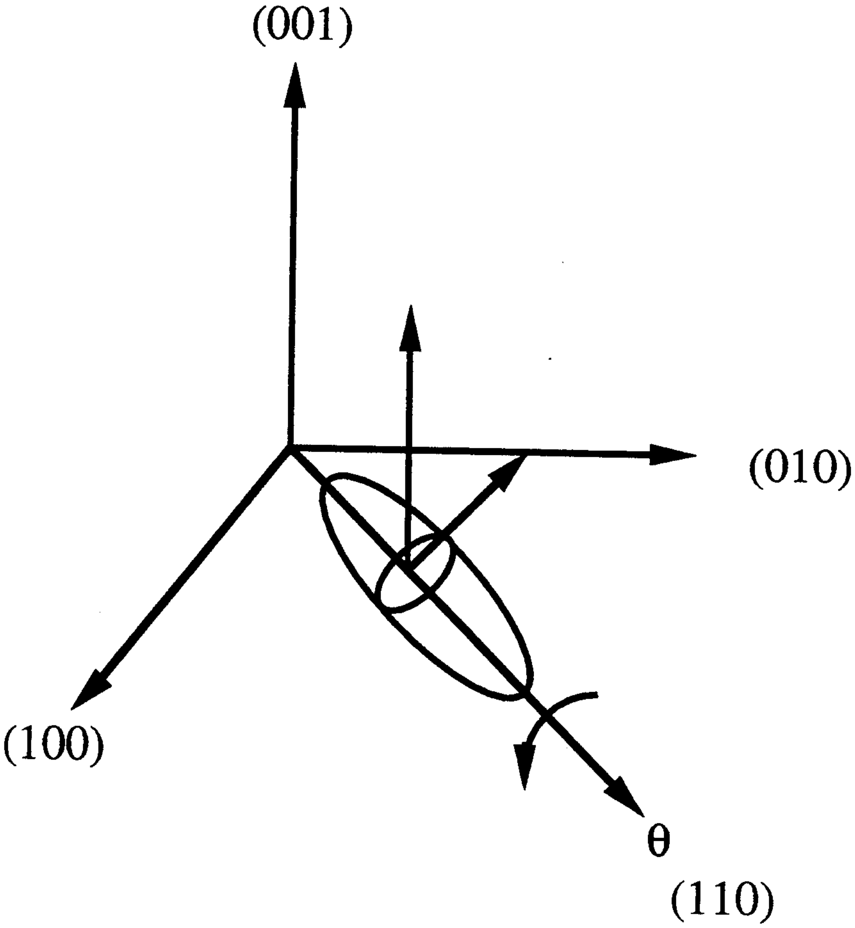

Figure 6. Constraints on the EFG for sites on (110) mirror planes.

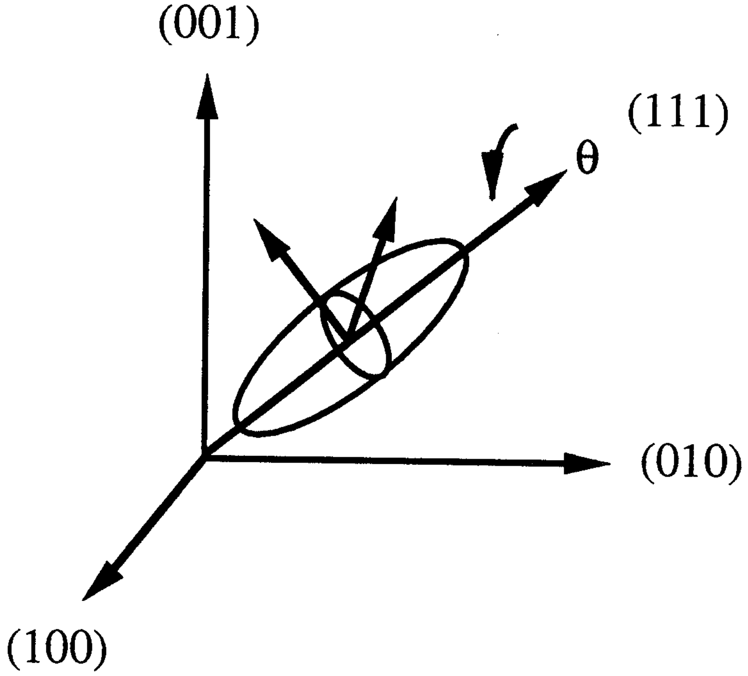

Figure 7. Constraints placed upon sites along the (111) axes.

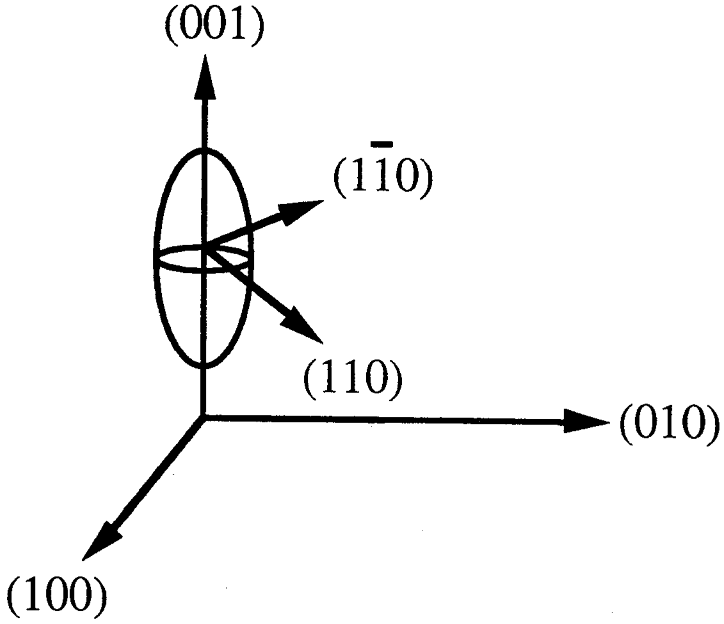

Figure 8. Constraints on EFG tensors along (100) cube axis.

2.4 Theory of NMR Nutation Studies

An NMR nutation transient is the time dependence of a component of the magnetization as it precesses about the rf field in the resonant rotating frame [1]. For spin $I = 1/2$ nuclei, there is a single precession frequency equal to $-\gamma B_1$, but for $I > 1/2$, several frequencies exist when there is unequal excitation of the allowed transitions by the rf field. This can occur when a large quadrupole interaction is present, moving the satellites outside of the rf bandwidth. In this limit, only the central transition is excited and the resulting nutation frequency is $\omega_{\mathrm{nutation}} = (I+1/2)\,\omega_1$ (fig. 9) [2]. The Fourier transform of this transient yields a great deal of information about the distribution of the magnitude of quadrupole couplings in solids. Samoson and Lippmaa incorporated this as the evolution period t_1 of a 2D experiment which separates the free evolution NMR spectra obtained in t_2 according to the size of the quadrupole coupling [15]. These 2D nutation experiments have been combined with techniques such as magic angle spinning [13] to further increase the resolution of the NMR spectrum and rotary echoes [14] to distinguish between ions possessing different relaxation rates. Until now, these 2D experiments have not been applied to single crystals of semiconductors. A sample of GaAs heavily doped with indium has been studied and the results indicate that this technique is well suited to studying the environment of dilute point defects and providing information on the degree of dopant clustering in single crystals. This technique has also been able to show that the broad shoulder in the 1D NMR spectrum [7,15] is attributable to first order satellites of more distant sites.

The exact analytical derivation for spin 3/2 was derived by Janssen and Veeman [16] and will be used to analyze the 2D nutation spectra. Assuming that $\omega_z >> \omega_Q$ and the irradiation is on resonance, the nonsecular terms in the Hamiltonian for a spin 3/2 in the rotating frame are discarded. The truncated (rotating frame) nutation Hamiltonian is (in rad/sec)

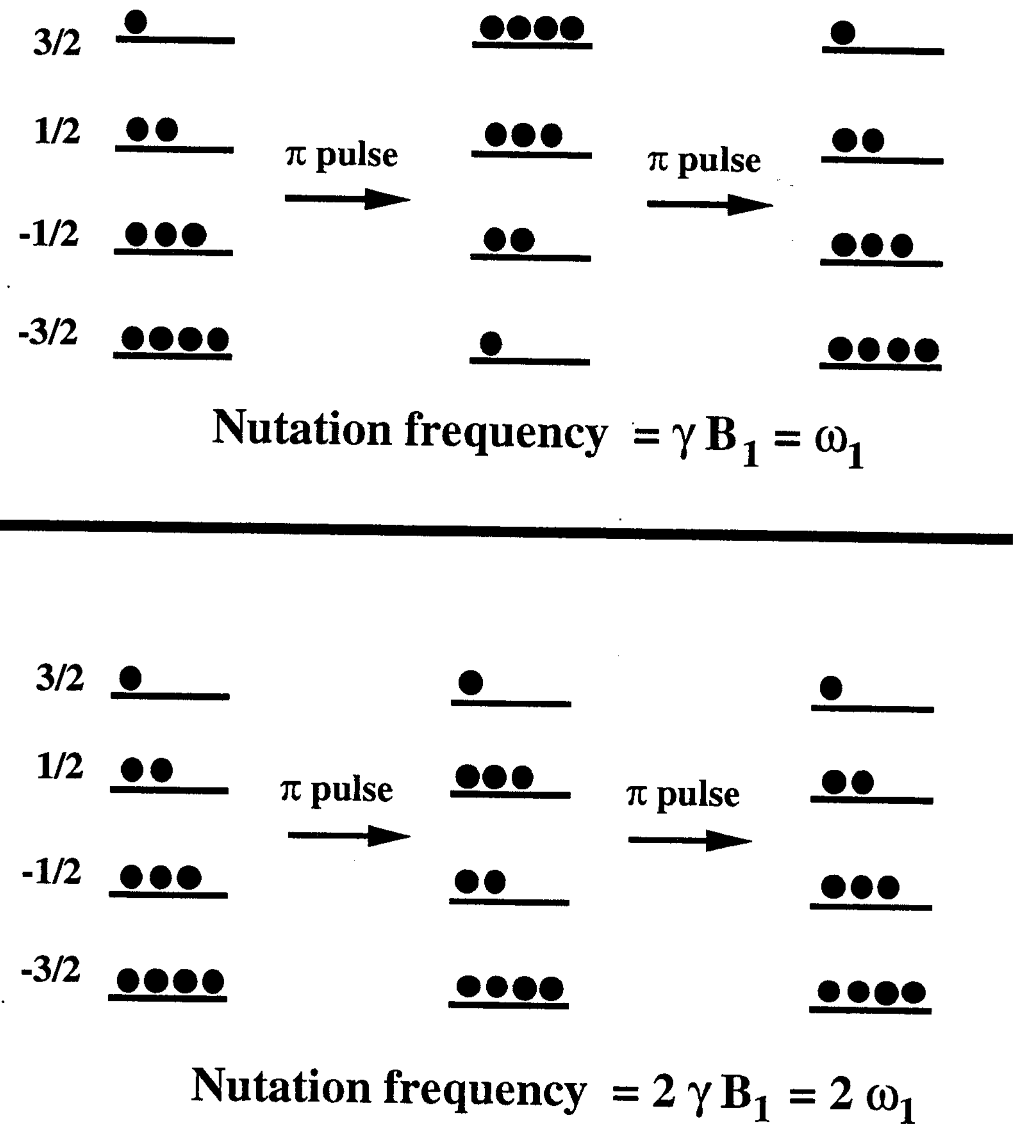

Figure 9. Nutation with small and large quadrupole coupling. For small quadrupole couplings (top), all the transitions are excited, and the nutation frequency is ω_1. For large quadrupole couplings (bottom), only the central transition is excited and the resulting nutation frequency is equal to $2\omega_1$.

$$H_1 \;=\; \omega_1 I_x + \omega_Q'(\, I_z^2 - 5/4\,) \qquad (22)$$

where ω_q' is related to the quadrupole coupling defined in equation (8) by (23)

$$\omega_Q' = \frac{3eQV_0}{4I(2I-1)\hbar} = 2\pi\left(\frac{1}{2}\nu_Q\right) \qquad (23)$$

Since the irradiation is on resonance, the proper quantization axis is about I_X. In this frame, the spin operators are

$$I_x = \begin{pmatrix} 3/2 & 0 & 0 & 0 \\ 0 & 1/2 & 0 & 0 \\ 0 & 0 & -1/2 & 0 \\ 0 & 0 & 0 & -3/2 \end{pmatrix}$$

$$I_Y = \hbar \begin{pmatrix} 0 & \sqrt{3}/2 & 0 & 0 \\ \sqrt{3}/2 & 0 & 1 & 0 \\ 0 & 1 & 0 & \sqrt{3}/2 \\ 0 & 0 & \sqrt{3}/2 & 0 \end{pmatrix} \tag{24}$$

$$I_z = i \begin{pmatrix} 0 & -\sqrt{3}/2 & 0 & 0 \\ \sqrt{3}/2 & 0 & -1 & 0 \\ 0 & 1 & 0 & -\sqrt{3}/2 \\ 0 & 0 & +\sqrt{3}/2 & 0 \end{pmatrix}.$$

Combining these expressions, we obtain the matrix form of the Hamiltonian for the nutation experiment

$$H_1^{(x)} = \frac{\omega_1}{2} \begin{pmatrix} 3-x & 0 & -\sqrt{3}x & 0 \\ 0 & 1+x & 0 & -\sqrt{3}x \\ -\sqrt{3}x & 0 & -1+x & 0 \\ 0 & -\sqrt{3}x & 0 & -3-x \end{pmatrix} \tag{24}$$

where $x = \frac{\omega_Q'}{\omega_1}$.

The matrix of $H_1^{(x)}$ can be put into a block diagonal form with the matrix $\boldsymbol{B}$, given by

$$B = \begin{pmatrix} cos(\alpha) & -sin(\alpha) & 0 & 0 \\ sin(\alpha) & cos(\alpha) & 0 & 0 \\ 0 & 0 & cos(\beta) & -sin(\beta) \\ 0 & 0 & sin(\beta) & cos(\beta) \end{pmatrix} \tag{26}$$

where $\tan(2\alpha) = -\frac{\sqrt{3}}{2}\frac{\omega_Q'}{\omega_1 - \frac{1}{2}\omega_Q'}$ and $\tan(2\beta) = -\frac{\sqrt{3}}{2}\frac{\omega_Q'}{\omega_1 + \frac{1}{2}\omega_Q'}$. The eigenvalues are

$$\begin{aligned} E_{x1} &= \frac{1}{2}\omega_1 + D_- \\ E_{x2} &= \frac{1}{2}\omega_1 - D_- \\ E_{x3} &= -\frac{1}{2}\omega_1 + D_+ \\ E_{x4} &= -\frac{1}{2}\omega_1 - D_+ \end{aligned} \qquad (27)$$

where $D_- = \left(\omega_1^2 - \omega_1\omega_Q' + \omega_Q'^2\right)^{1/2}$ and $D_+ = \left(\omega_1^2 + \omega_1\omega_Q' + \omega_Q'^2\right)^{1/2}$. These are the eigenvalues which govern the evolution while the nutation pulse is on. Figure 10 is a plot of the dimensionlesseigenvalues E_i/ω_1 as a function of the dimensionless quadrupole coupling ω'_Q/ω_1. Taking differences of the nutation eigenvalues, the allowed nutation frequencies and their asymptotic values for large ω_Q ($\omega_1 << \omega_Q << \omega_0$) are found to be

$$\omega_{\text{nut}}^{(1)} = \omega_1 + D_- - D_+ \qquad (\omega_{\text{nut}}^{(1)} \to 0) \qquad (28)$$

$$\omega_{\text{nut}}^{(2)} = \omega_1 - D_- + D_+ \qquad (\omega_{\text{nut}}^{(2)} \to 2) \qquad (29)$$

$$\omega_{\text{nut}}^{(3)} = -\omega_1 + D_- + D_+ \qquad (\omega_{\text{nut}}^{(3)} \to \infty) \qquad (30)$$

The nutation frequencies are plotted in figure 11. For large quadrupole couplings, the satellites are outside the rf bandwidth. As a result, only oscillations of the central transitions are present, asymptotically approaching a single component at twice the Rabi frequency. The columns of the matrix ***B*** are the eigenvectors in the basis of $|m_x\rangle$. To facilitate the interpretation of the oscillations, it is simpler to convert to the basis of $|m_z\rangle$ with the matrix ***A***, where A is defined as

$$|m_z\rangle = A|m_x\rangle \qquad (31)$$

so that

$$A = \frac{\sqrt{2}}{4}\begin{pmatrix} 1 & \sqrt{3} & \sqrt{3} & 1 \\ \sqrt{3} & -1 & 1 & -\sqrt{3} \\ \sqrt{3} & -1 & -1 & \sqrt{3} \\ 1 & \sqrt{3} & \sqrt{3} & -1 \end{pmatrix} \tag{32}$$

and

$$T = AB = \frac{1}{\sqrt{2}}\begin{pmatrix} \cos\theta_- & \sin\theta_- & \cos\theta_+ & \sin\theta_+ \\ \sin\theta_- & -\cos\theta_- & \sin\theta_+ & -\cos\theta_+ \\ \sin\theta_- & -\cos\theta_- & -\sin\theta_+ & \cos\theta_+ \\ \cos\theta_- & \sin\theta_- & -\cos\theta_+ & -\sin\theta_+ \end{pmatrix} \tag{33}$$

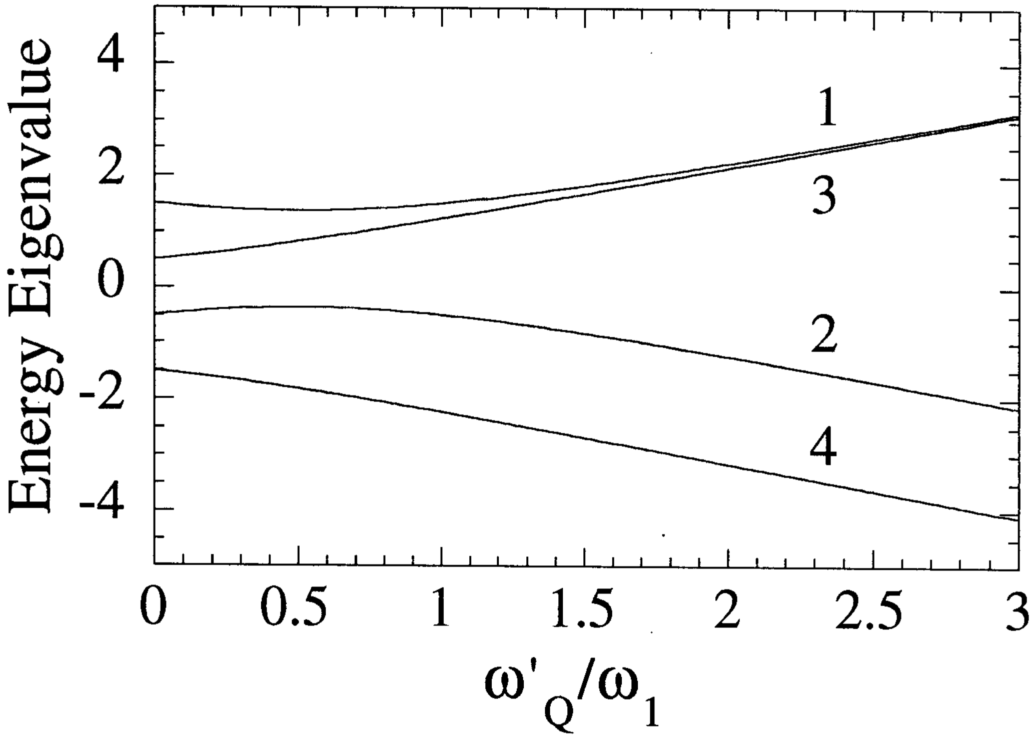

Figure 10. The nutation eigenvalues.

where

$$\begin{aligned}
&\cos\theta_- = \cos\alpha + \sqrt{3}\sin\alpha \\
&\sin\theta_- = \sqrt{3}\cos\alpha - \sin\alpha \\
&\cos\theta_+ = \sqrt{3}\cos\beta + \sin\beta \\
&\sin\theta_+ = \cos\alpha - \sqrt{3}\sin\beta \\
&\tan 2\theta_- = \frac{1}{2}\sqrt{3}\omega_1 / (\omega'_Q - \frac{1}{2}\omega_1) \\
&\tan 2\theta_+ = \frac{1}{2}\sqrt{3}\omega_1 / (\omega'_Q + \frac{1}{2}\omega_1)
\end{aligned} \tag{34}$$

In the limit as ω_Q becomes much larger than ω_1, only the central transition is excited. This can be seen by noting that the eigenvectors in the $|m_z\rangle$ basis which correspond to the

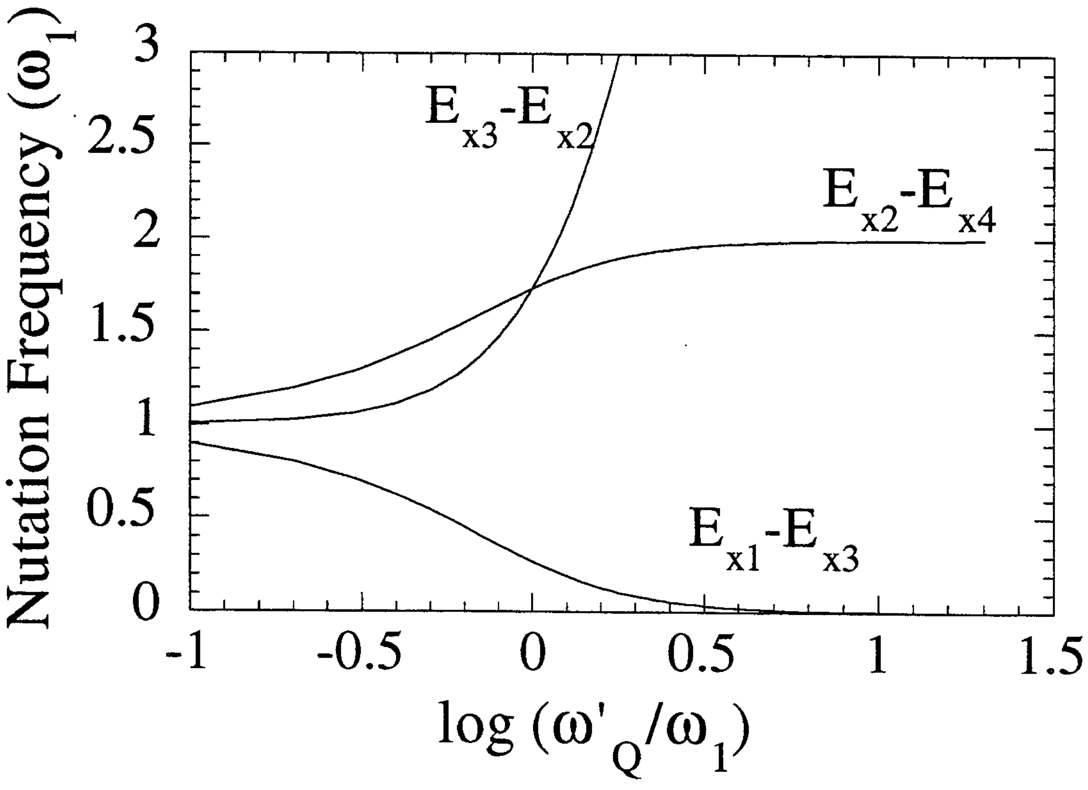

Figure 11. Nutation frequency versus ratio of quadrupole coupling and rf field strength.

eigenvalues E_{x2} and E_{x4} are in the second and fourth columns of the matrix ***T***. For large quadrupole couplings, both θ_+ and $\theta_- = 0$. This leaves the eigenvectors

$$|2\rangle = \begin{pmatrix} 0 \\ -1 \\ -1 \\ 0 \end{pmatrix} \quad \textit{and} \quad |4\rangle = \begin{pmatrix} 0 \\ -1 \\ 1 \\ 0 \end{pmatrix} \tag{35}$$

which correspond to superpositions of unperturbed central states in coherent superposition at twice the nutation frequency.

2.5 Experiment

All of the following experiments were performed on a homebuilt spectrometer in the Weitekamp group with a 4.7 Tesla wide-bore magnet from Nalorac. Samples of indium doped GaAs, grown by the liquid encapsulated Czochralski (LEC) method, were obtained from Sumitomo Electronics. The indium doping concentration is $9.0 \times 10^{19}/\text{cm}^3$. The resistivity of this sample is > $7.9\text{x}10^7$ ohm-cm and Hall mobility is 5.1×10^3 (cm^2/Volt-sec). The original wafer was 450 μm thick and 50 mm in diameter. The surface orientation is (100), the primary flat is $(0\bar{1}\bar{1})$, and the secondary flat is $(0\bar{1}1)$. Samples used in the experiment were 0.5 cm wide cut along the $(0\bar{1}1)$ axis with a diamond tipped saw 1.5 cm long, while stacked three high. For comparison, NMR spectra were taken of a sample of undoped GaAs.

2.5.1 NMR Sample Characterization

The interactions responsible for the linewidth of GaAs are dipole-dipole, exchange, pseudo-dipolar, and when defects are present, quadrupolar. The observed line width is larger than expected from dipole-dipole interactions and has been attributed to the indirect nuclear exchange interaction between unlike nuclei [17] of the form $A\vec{I}_1 \bullet \vec{I}_2$ resulting from hyperfine contact with electrons [18]. Figures 12, 13, 14 show NMR spectra of the three principal isotopes of undoped bulk GaAs resulting from Fourier transforms of free induction decays (fid) sampled beginning at a spin-echo (all references to spin echoes are π/4 – τ – π/2 sequences to optimize sensitivity to perturbed central transitions and are indistinguishable from spectra obtained from the fid after a simple π/2 pulse. The indium doped samples exhibited similar linewidths, although a broad shoulder was observable in the echo experiment [7,15] which was attributed to first order quadrupolar satellites. These linewidths are slightly narrower than those measured in powders, which has additional defects induced by the grinding process [19].

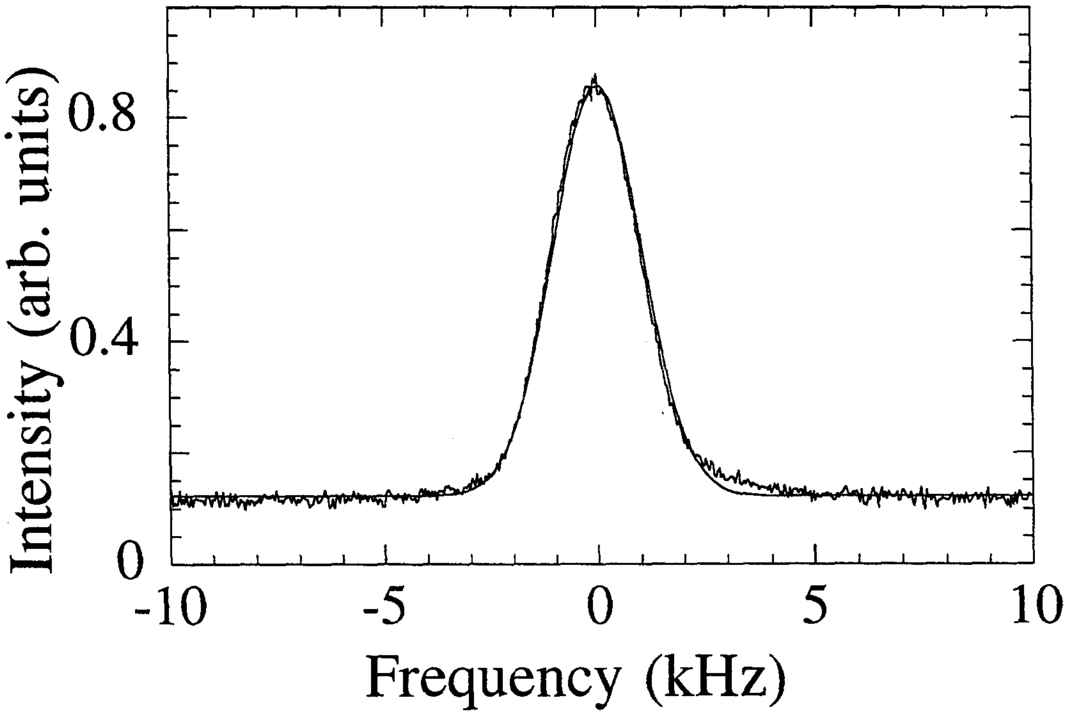

Figure 12. ^{69}Ga NMR echo spectrum of undoped GaAs. The linewidth is 2.4 kHz.

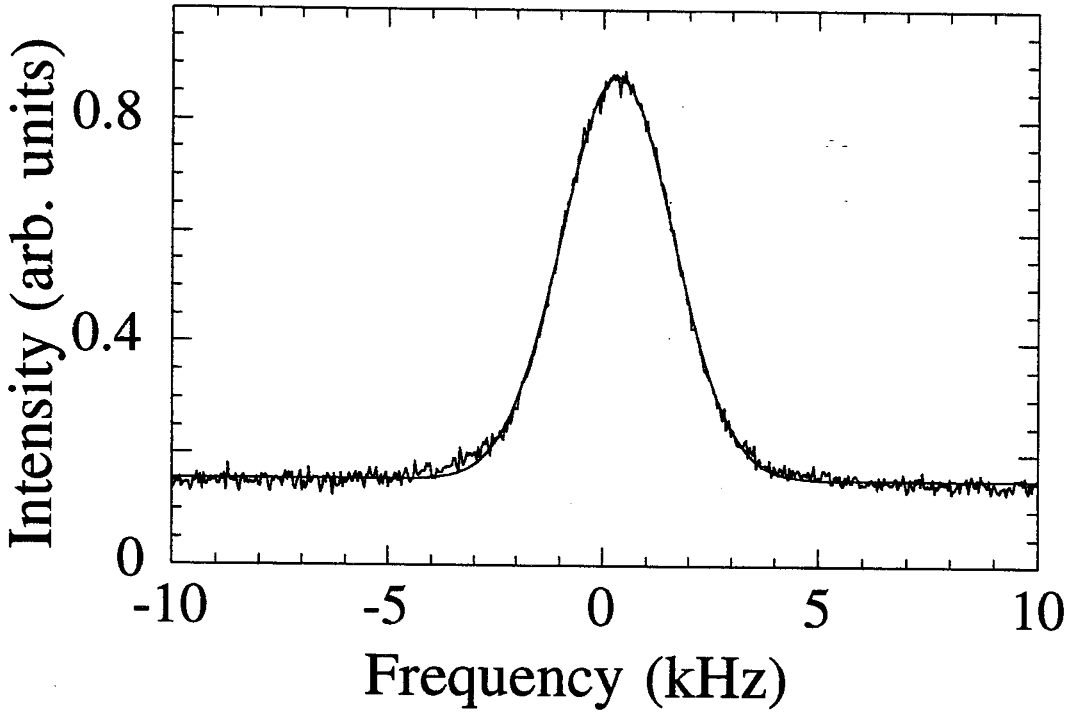

Figure 13. ^{71}Ga echo detected spectrum of undoped GaAs. The linewidth = 3.1 kHz.

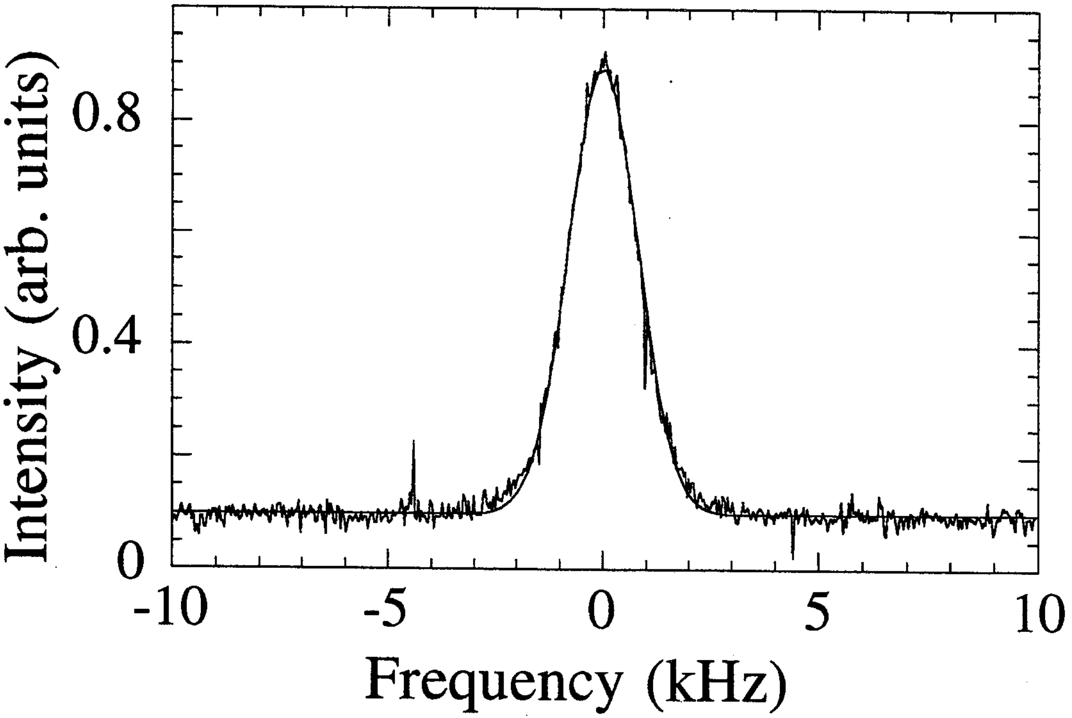

Figure 14. ^{75}As spectrum of undoped GaAs. The linewidth = 1.9 kHz.

T_1 (seconds)	Nucleus
0.34	^{69}Ga
0.73	^{71}Ga
0.22	^{75}As

Table 3. T_1 of the three principal isotopes in GaAs. The values were obtained by inversion recovery at room temperature.

Figure 15 is a 1D spin echo spectrum of ^{75}As with pulse times optimized to accentuate the signal from the second order shifted peaks. There are peaks on either side of the central transition at zero frequency offset which correspond to second order shifts of the central transition. These sites are not observable by an FT experiment with only a $\pi/2$ pulse because for strongly perturbed nuclei, this corresponds to a π pulse which inverts the longitudinal magnetization, but gives no signal. In addition, the broad 30 kHz line is unobservable with the simple FT experiment because of the 12 μsec deadtime necessary to allow for probe and receiver ringing.

This broad shoulder has been attributed to first order satellites [7] and fit with intensities corresponding to a $1/r^3$ distribution of strain about an indium site. The resulting lineshapes were found to be in agreement, but are not conclusive.

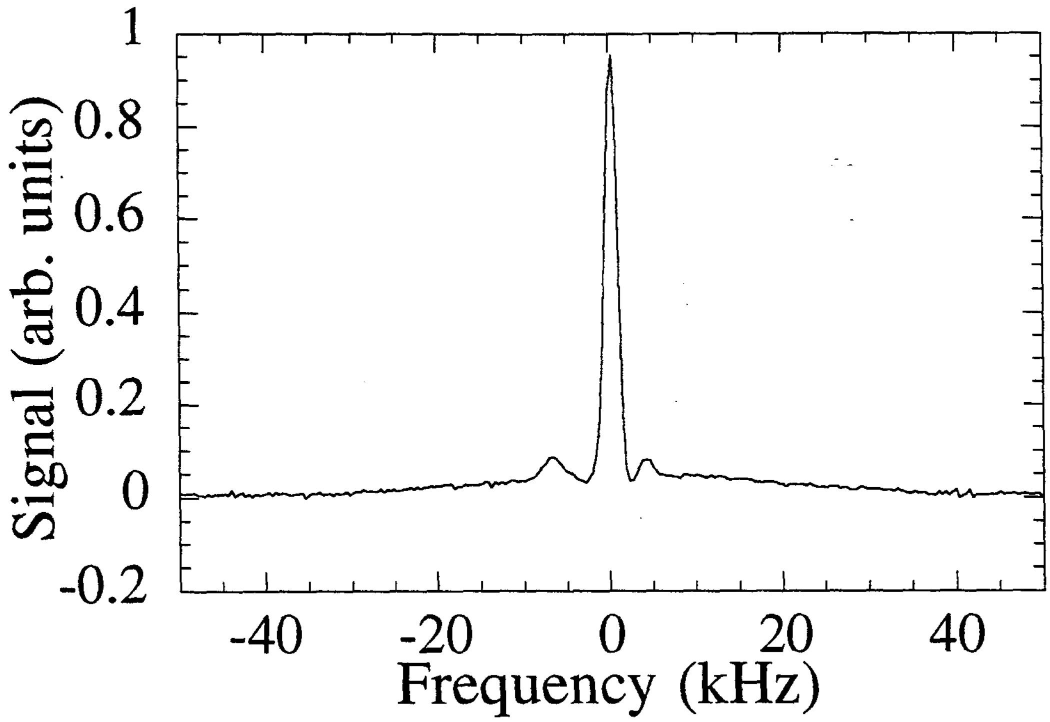

Figure 15. ^{75}As echo spectrum in In doped GaAs.

2.6 1D Nutation Experiments in Indium Doped GaAs

Figure 16 shows the nutation transient of ^{75}As in an undoped sample of GaAs. The signal is well fit by a single Rabi frequency which indicates that all measurable intensity is from atoms at undistorted sites. To exclude the interpretation of a single nutation frequency at $2\omega_1$ with half the rf field amplitude, a nutation transient of ^{23}Na was obtained in NaBr, which is expected and observed to nutate at ω_1, having only weak quadrupole interactions. Nutation spectra for ^{69}Ga and ^{71}Ga exhibit the same overriding feature and are not shown.

Figure 17 is a 1D transient nutation spectrum of ^{75}As nuclei in the indium doped GaAs sample and figure 18 is the resulting FT nutation spectrum. There are two distinct peaks at ω_1 and $2\omega_1$ where $\omega_1 = -\gamma B_1$. The nutation spectrum for doped GaAs exhibits a

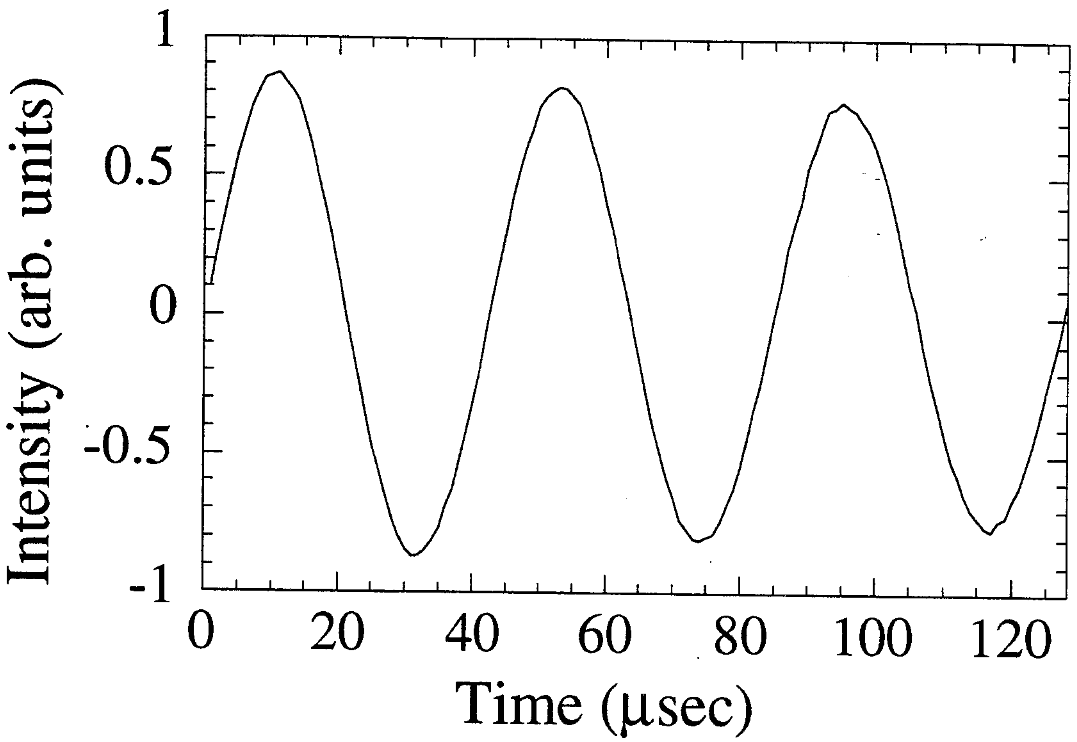

Figure 16. ^{75}As nutation transient in undoped GaAs.

significant amount of damping compared to the undoped sample. Dissipation of the applied rf could possibly lead to broadening of the Fourier transformed signal, but the resulting FT nutation spectrum exhibits two distinct peaks of comparable intensity which are not at the unperturbed Rabi frequency ω_1 in addition to a dominant peak at ω_1. These new frequencies are due to sites experiencing substantial quadrupole couplings. ^{71}Ga nutation experiments exhibit similar behavior, but these studies have not been pursued. The results of the ^{75}As NMR nutation studies will be presented.

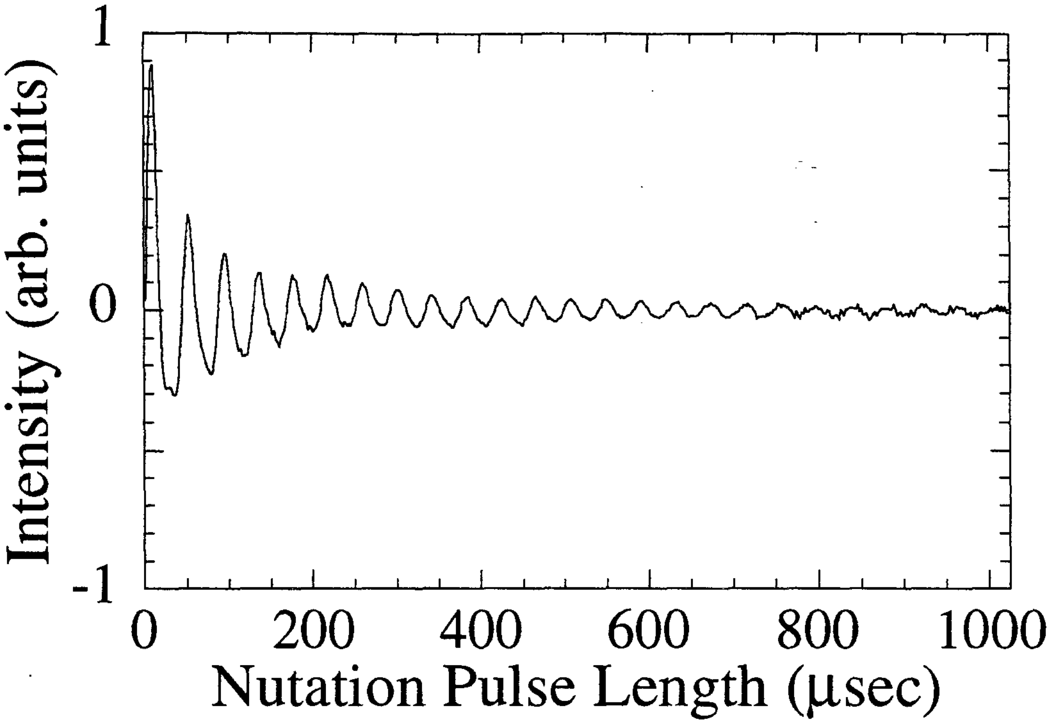

Figure 17. ^{75}As nutation transient in In doped GaAs. 512 points were acquired with 2 μsec steps.

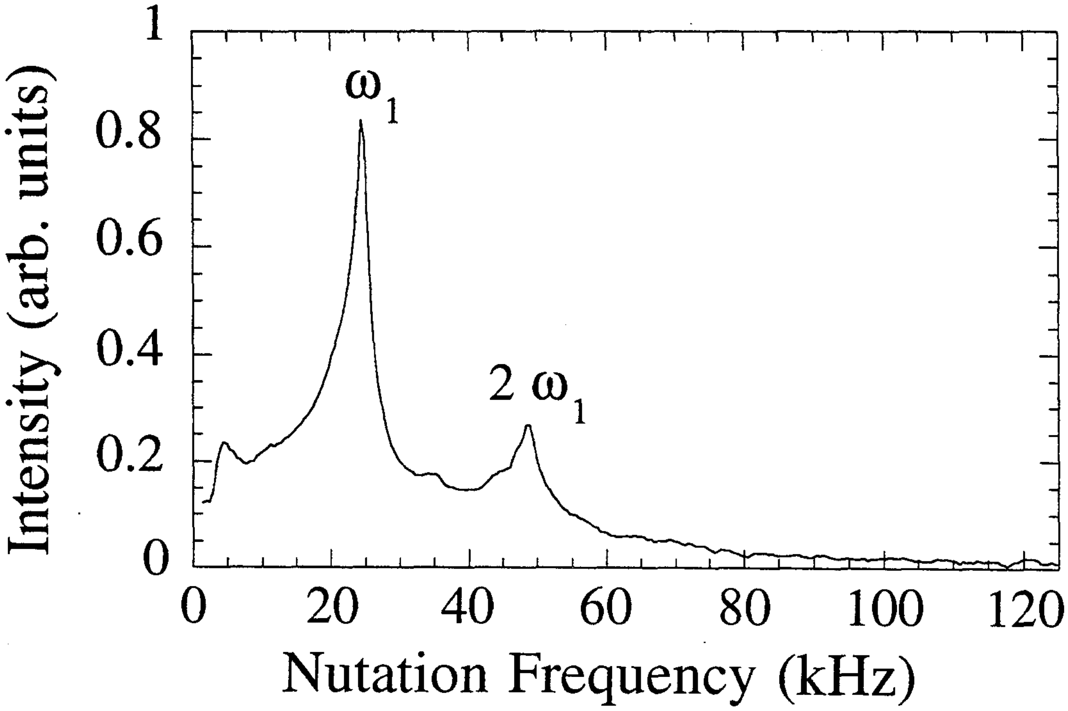

Figure 18. ^{75}As FT nutation spectrum (magnitude spectrum).

2.7 2D Nutation Experiment

A 2D nutation experiment (fig. 19) was used to separate the resonances of various lattice sites according to both nutation and free evolution frequencies. The intensity of the signal in t_2 is modulated as a function of the irradiation time t_1. The differential nutation in the t_1 dimension allows for the separation of the perturbed and unperturbed sites. The ^{75}As Larmor frequency was 33.9 MHz in a 4.7 T magnetic field. The nutation pulse was stepped from 550 nsec in 4 μsec increments, followed by a dephasing delay Δ of 20 msec. A total of 256 increments were used. The resulting z-magnetization was detected by the spin echo sequence $\pi/4 - \tau - \pi/2$ to accentuate the central transition, with $\tau = 200$ μsec. During the t_2 transient, 256 points were detected with a bandwidth of 100 kHz. The recycle delay was 1.3 seconds. Four phase-cycle steps were used in the echo detection to correct for receiver and transmitter quadrature errors with 32 scans per phase cycle step. Experiments were performed at 19 °C.

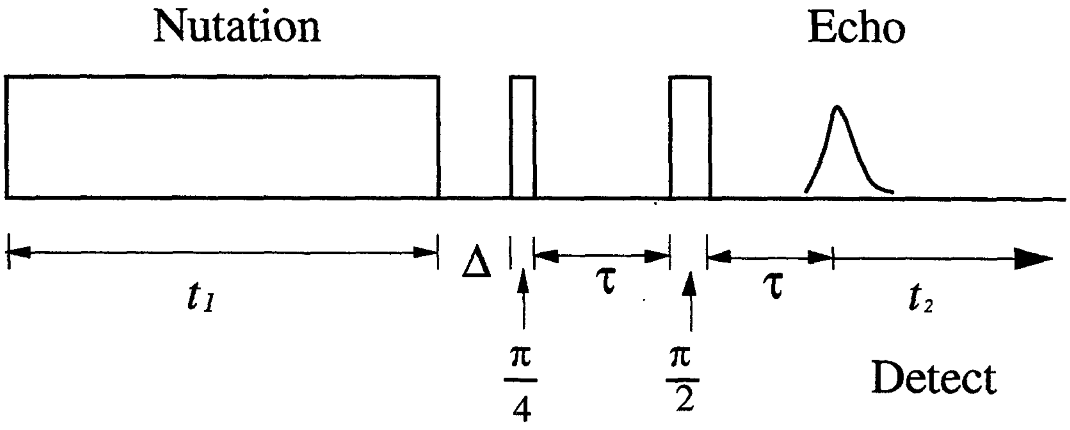

Figure 19. Pulse sequence for 2D nutation sequence. The nutation pulse is followed by a dephasing delay of 20 msec denoted as Δ. The resulting component along I_Z is detected by a spin echo pulse sequence with pulse times selected to enhance sites with large quadrupole coupling. The free evolution period takes place in t_2.

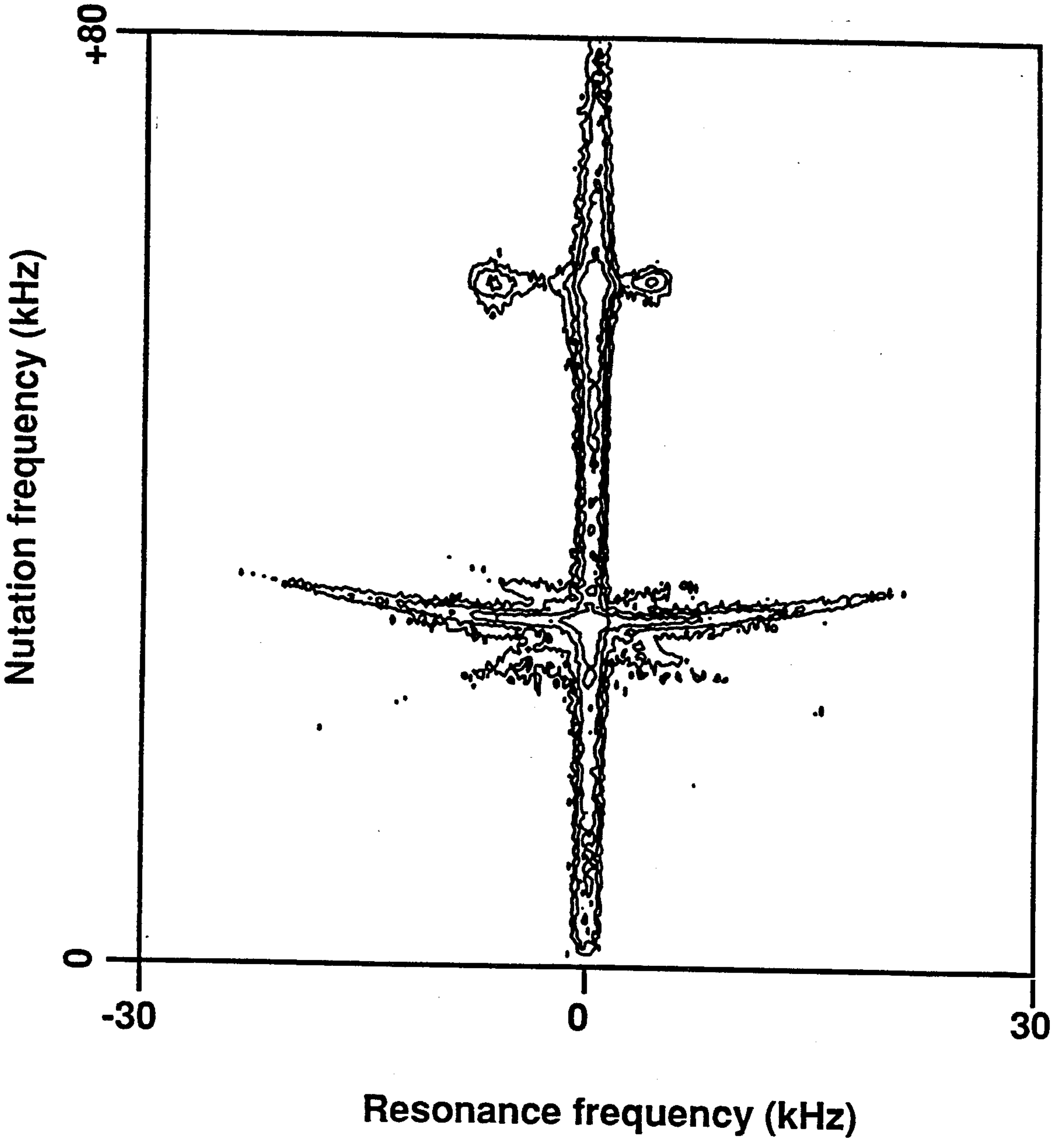

Figure 20. Magnitude spectrum of the 2D NMR FT nutation spectrum of indium-doped bulk GaAs.

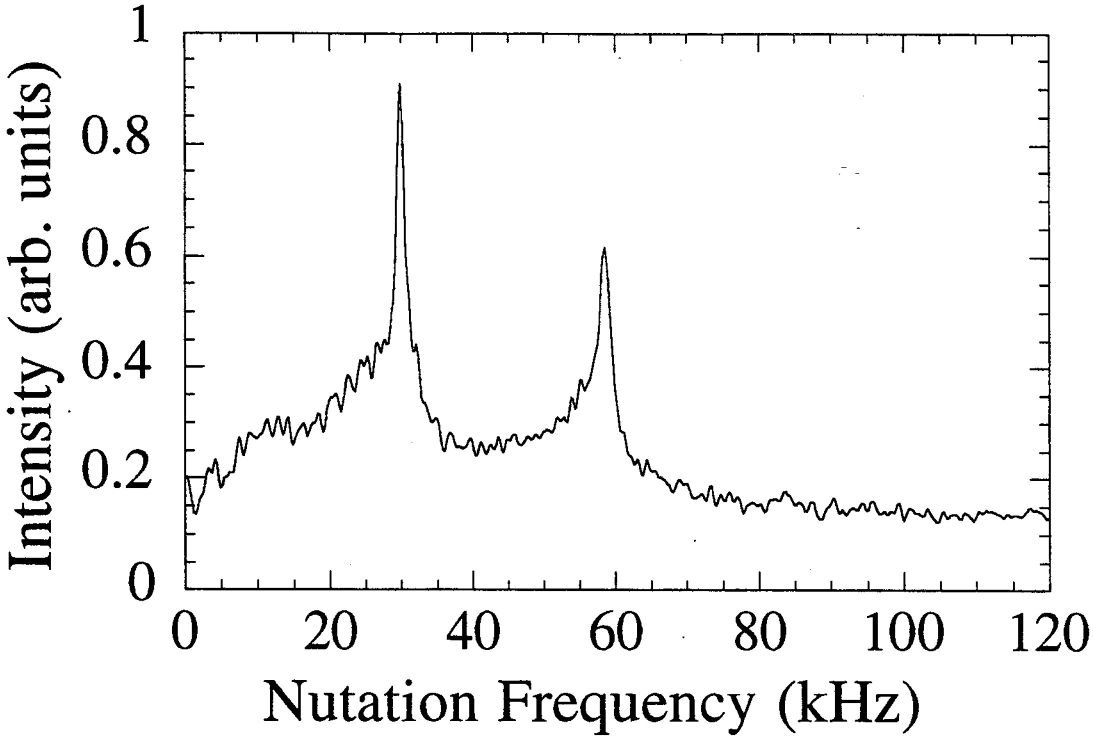

Figure 21. Projection of 2D nutation spectrum along the axis of the NMR resonance frequency. The features correspond to the spectrum observed in the 1D experiment (fig. 17), but with greater relative intensity for the $2\omega_1$ peak.

The nutation spectrum (magnitude) is shown in figure 20 and a projection of the peaks at $2\omega_1$ is shown in figure 21 with greatly improved isolation of the defect-site. The broad underlying intensity is from sites with $\omega_Q >> \omega_1$, but not large enough to have resolved second-order shifts.

2.8 Rotation Studies

The second order shift of the resolved central transitions was measured as a function of sample orientation with respect to the magnetic field. Starting out with the [100] axis parallel to the magnetic field, the sample was rotated about the $[0\bar{1}1]$ axis by 90° in 10 degree increments. The ^{75}As shifts observed here at 4.7 Tesla (T) are distinct from those seen previously [7] at 12 T by ordinary echo detection. No evidence of those sites attributed to a second nearest neighbor ^{75}As was seen at the frequencies expected in our field on the basis of the reported [7] spin Hamiltonian. Figure 22 illustrates the orientation of the crystal axes relative to the lab frame. In this case, the goniometer frame is fixed to the crystal frame.

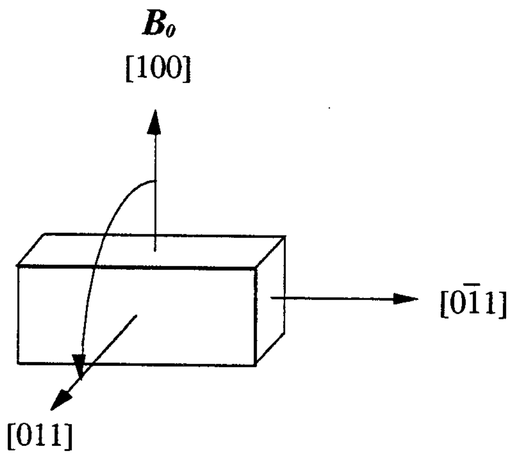

Figure 22. Orientation of crystal axes relative to rotation axes in the lab frame.

The orientation dependence of the peaks at twice the rf nutation frequency were fit based on the pattern expected of the (110) symmetry class. The other possible sites attributed to [111] axis sites were eliminated because only one peak is expected when the magnetic field is parallel to the [001] axis while two peaks are actually observed. There are no ^{75}As sites with [100] symmetry, so this possibility may be eliminated. However, there are many shells with (110) symmetry so that this assignment will not uniquely specify a site. Table 4 tabulates the symmetry of the first few shells [8].

To improve sensitivity, the 1D spectra used in the fits were obtained by projecting the signal along the nutation frequency axis for 7 rows where the second-order shifted peaks are located at twice the nutation frequency. It is not yet understood, but the signals from the unshifted central transition are 90° out of phase from the second-order shifted peaks which allows us to use spectra from the latter component. This has both simplified and complicated the fitting procedure. By removing additional signals, sites close to the

Atom Type	Shell Number	Shell Class	Location of One Site
In	0	5	(0,0,0)
As	1	3	(1,1,1)
Ga	2	2	(2,2,0)
As	3	2	$(\bar{1},\bar{1},\bar{3})$
Ga	4	4	(0,0,4)
As	5	2	(3,3,1)
Ga	6a	2	(2,2,4)
Ga	6b	2	$(\bar{2},\bar{2},\bar{4})$
As	7and	3	$(\bar{3},\bar{3},\bar{3})$
As	8	2	(1,1,5)
Ga	9	2	(4,4,0)
As	10	1	$(1,\bar{3},5)$
Ga	11	1	(0,2,6)
As	12	2	(3,3,5)
Ga	13a	3	(4,4,4)
Ga	13b	3	$(\bar{4},\bar{4},\bar{4})$
As	14 and	2	(5,5,1)
As	15	2	$(\bar{1},\bar{1},\bar{7})$
Ga	16a	1	(6,4,2)
Ga	16b	1	$(\bar{6},\bar{4},\bar{2})$
As	17 and	1	(1,3,7)
As	18	2	$(\bar{5},\bar{5},\bar{3})$
Ga	19	4	(0,0,8)
Ga	20	2	$(\bar{3},\bar{3},\bar{7})$
As	21 and	2	(6,6,0)
As	22a	2	(2,2,8)
As	22b	2	$(\bar{2},\bar{2},\bar{8})$
Ga	23 and	3	(5,5,5)
Ga	24	1	$(1,\bar{5},7)$
As	25	1	(0,4,8)
Ga	26	1	(3,5,7)
As	27	2	(1,1,9)
Ga	28a	2	(6,6,4)
Ga	28b	2	$(\bar{6},\bar{6},\bar{4})$
As	29	1	$(1,\bar{3},9)$
Ga	30a	2	(4,4,8)
Ga	30b	2	$(\bar{4},\bar{4},\bar{8})$

Table 4. Tabulation of the first 30 shells in GaAs about a site of tetrahedral symmetry. In the table, "and" refers to sites at the same distance and "a" and "b" refer to sites related by inversion symmetry (table from [8]).

central transitions can be resolved, but the resulting phase shifts have distorted the line positions and intensities, which has led to errors for fitting peaks with the larger second order shift. Since it is a phase error, this does not exceed the linewidth of the resonance.

The expected spectrum was simulated by generating a rotation pattern for the (110) symmetry sites and fitting the line position by least squares about a local minimum. The algorithm used is as follows:

Step 1. Rotate the EFG tensor from the PAS to the CRS (crystal frame).

Step 2. Generate tensor for all sites by permuting matrix elements according to symmetry operations.

Step 3. Rotate the EFG from the CRS to the LAB frame coincident with the external magnetic field.

Step 4. Rotate from the LAB frame to the goniometer frame.

Step 5. Rotate sample in the goniometer frame.

A program, ROT.C, has been written to generate rotation patterns for all sites in a particular shell. Using the fitted data, rotation patterns are generated for each site.

To reduce the number of free parameters used in the fit, the linewidths used correspond to the intrinsic linewidth of ^{75}As measured previously in the bulk sample. There are a total of five fitted parameters. The first is the amplitude of the signal at zero frequency offset, presumably due to sites with large quadrupole coupling, but with unresolved second order shifts. The other four free parameters are the peak positions corresponding to the four expected lines. Because the peak positions are not unique, a global fit is not used because it allows the possibility of swapping the peak positions. Determining the structure of the defect directly from the rotational dependence of the data is not possible [20]. The only method is to make a guess about the expected model, and then to compare these predictions with the data. Figures 23 through 32 are the fitted spectra, and figure 33 presents the results of the fit as a function of orientation.

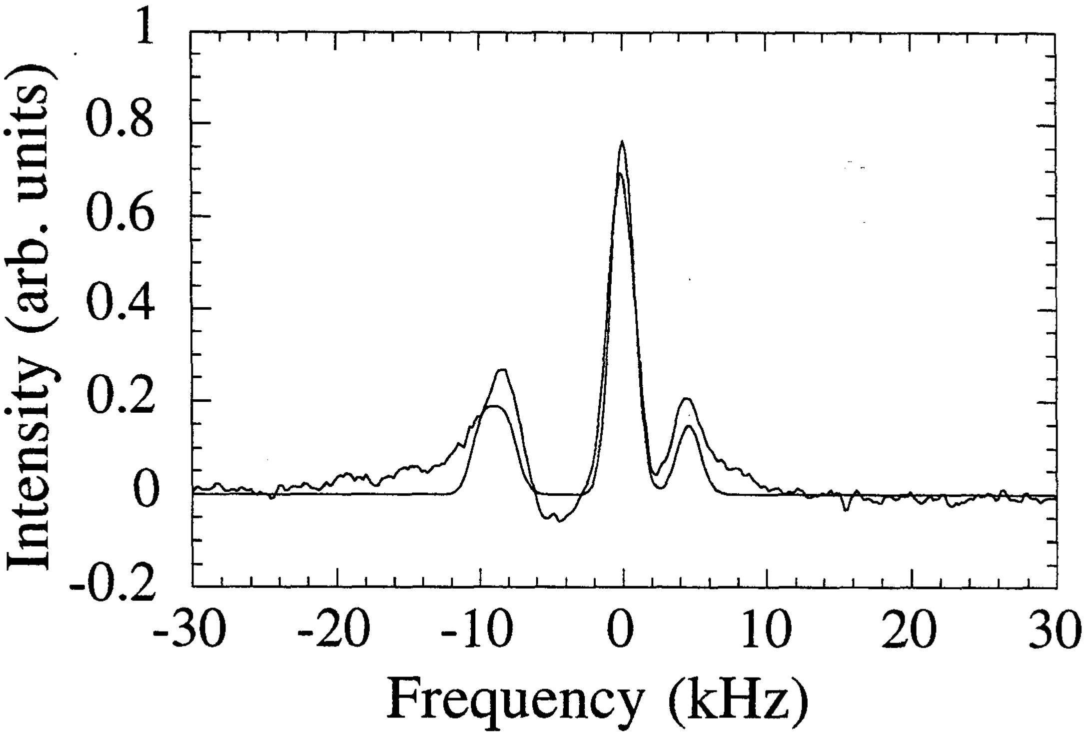

Figure 23. 0° orientation.

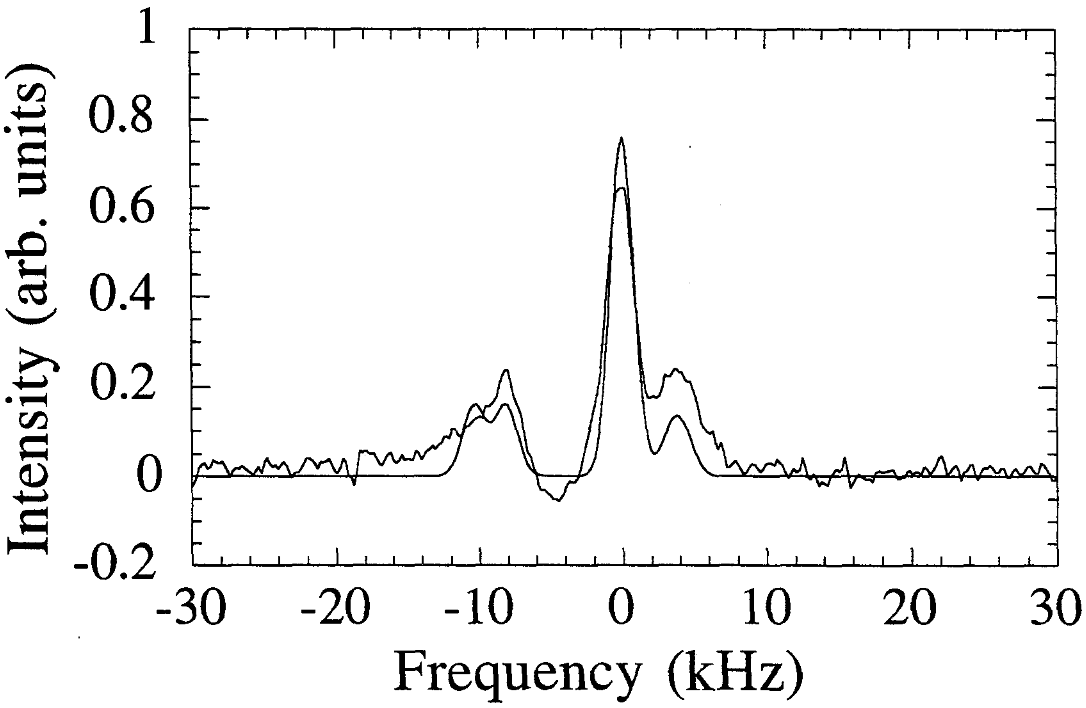

Figure 24. 10° orientation.

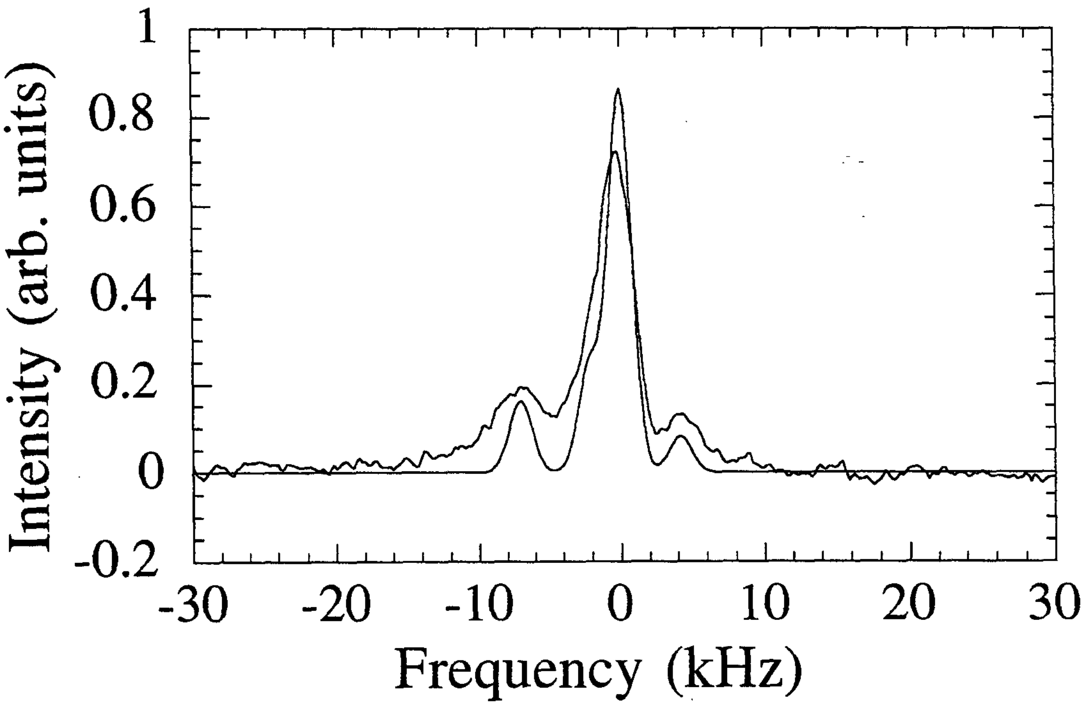

Figure 25. 20° orientation.

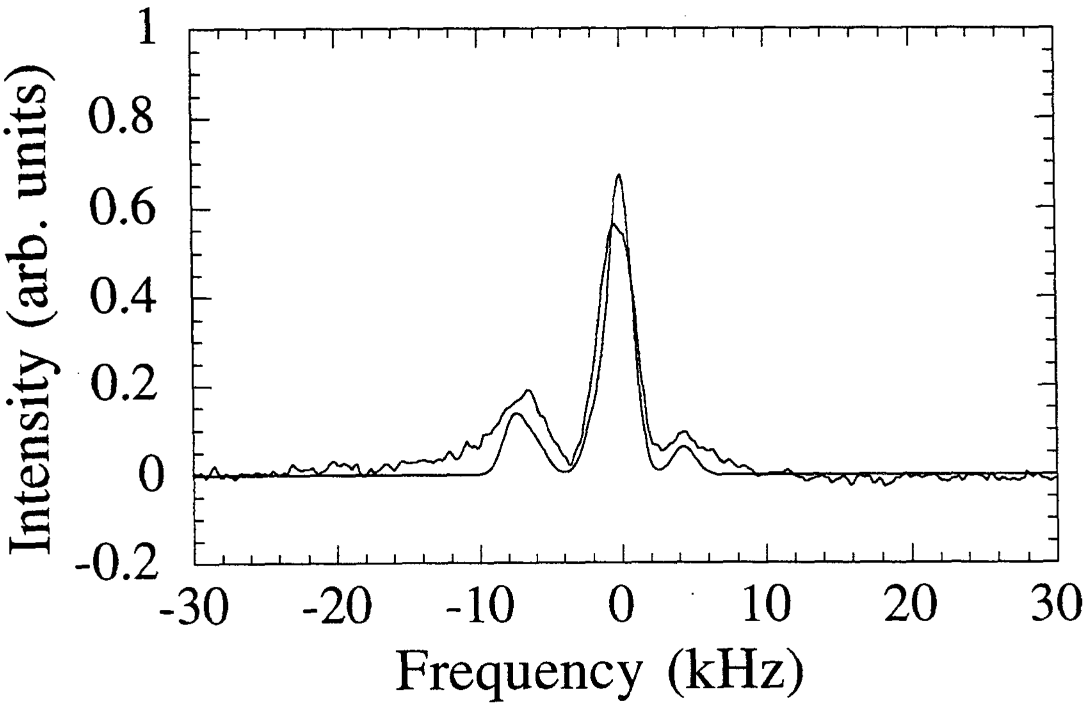

Figure 26. 30° orientation.

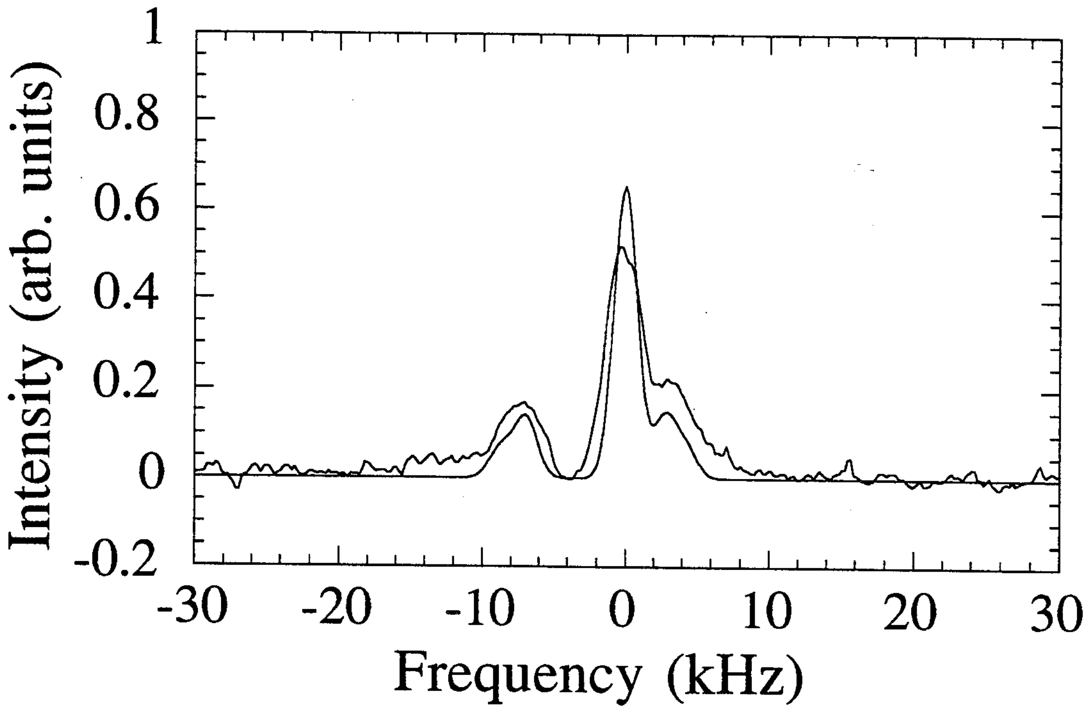

Figure 27. 40° orientation.

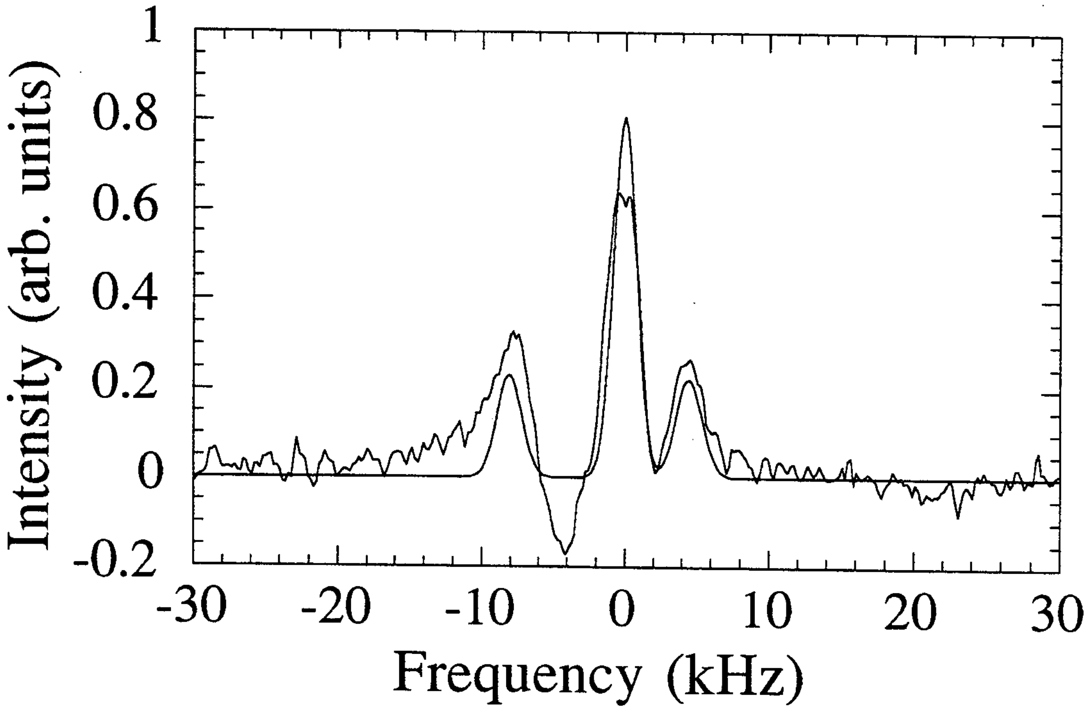

Figure 28. 50° orientation.

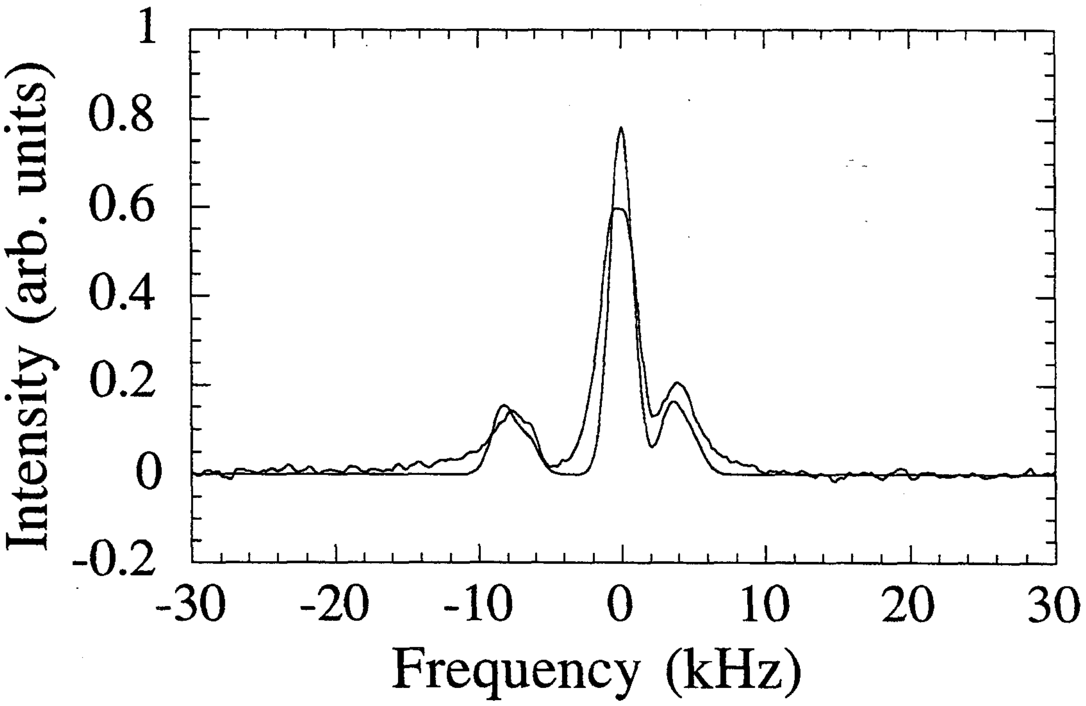

Figure 29. 60° orientation.

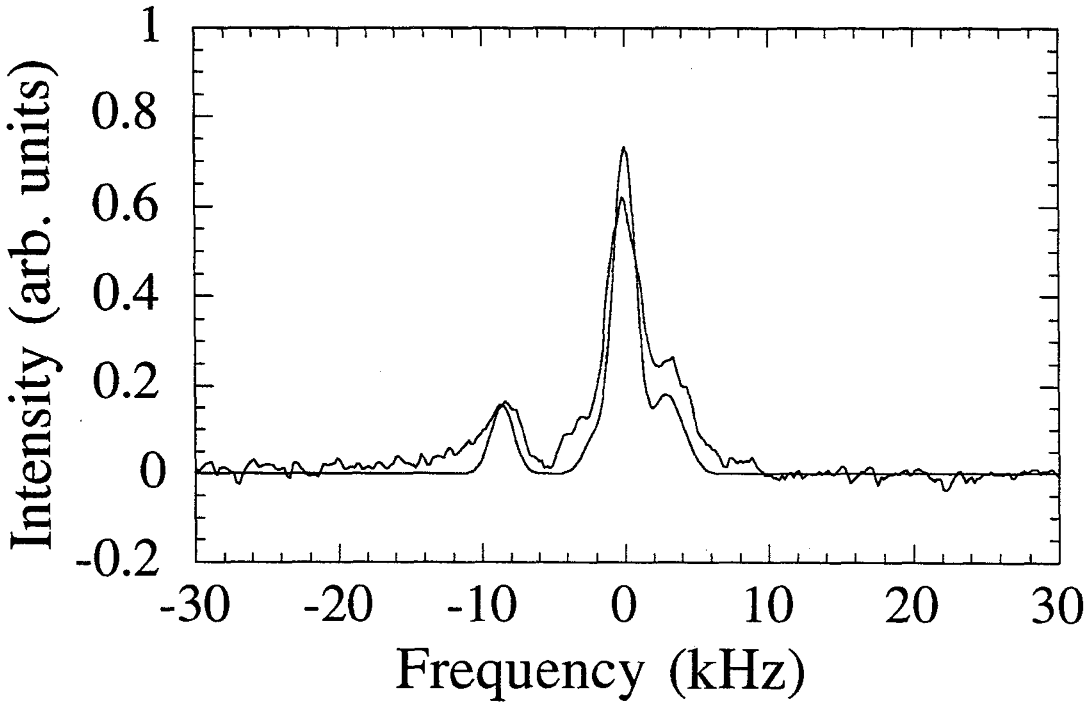

Figure 30. 70° orientation.

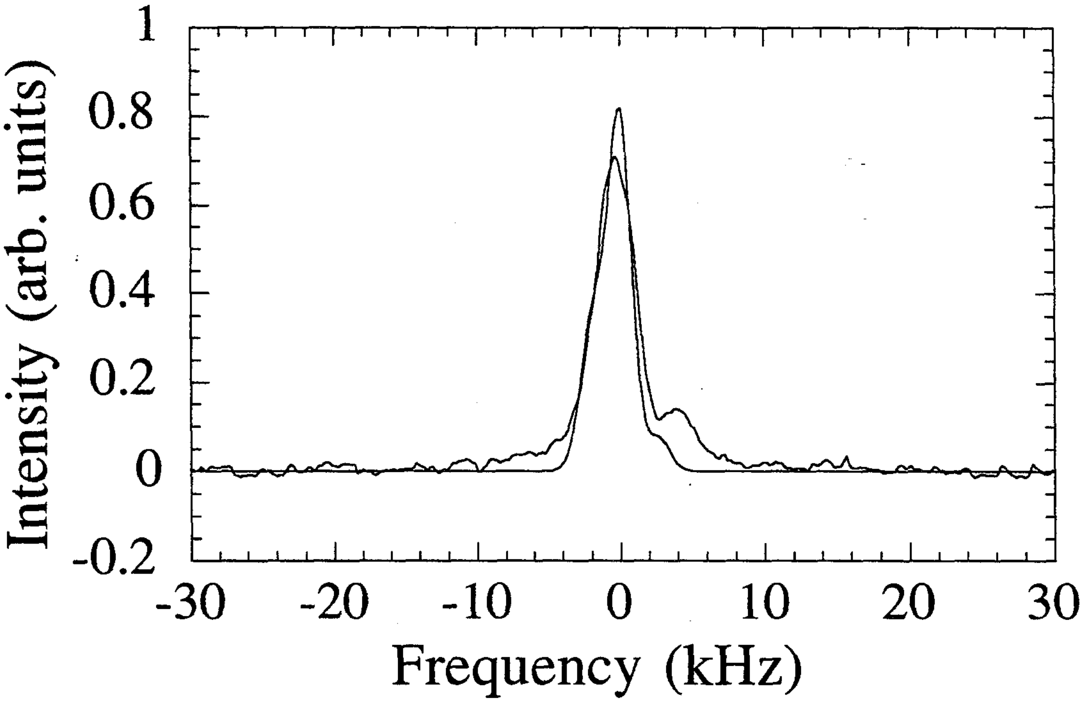

Figure 31. 80° orientation.

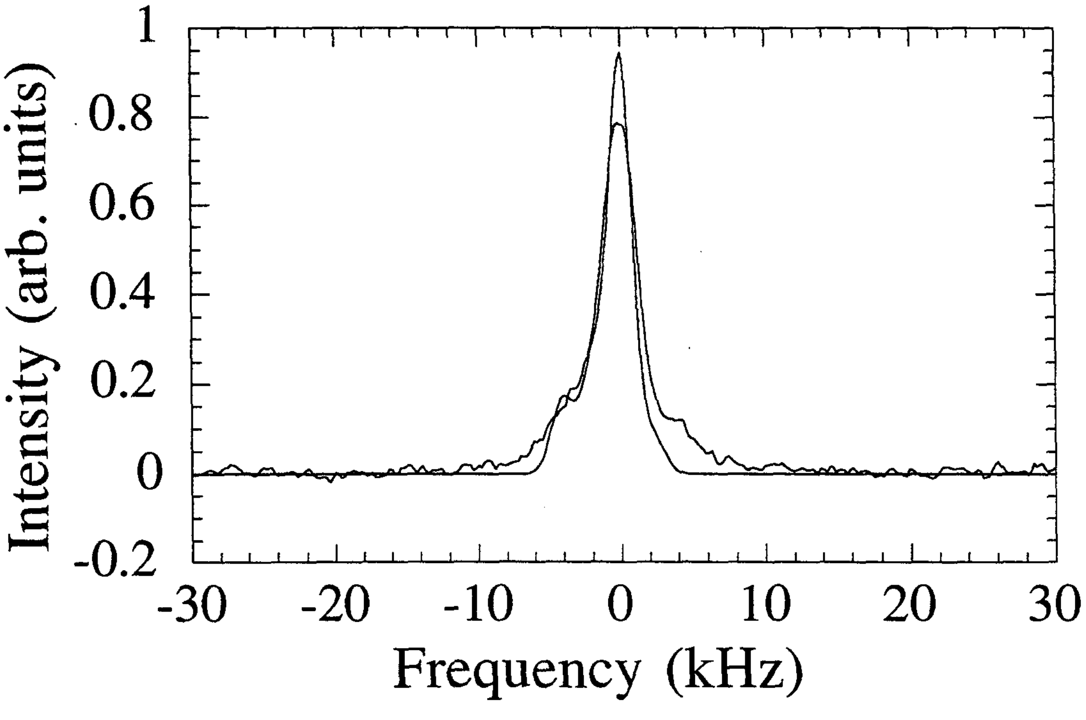

Figure 32. 90° orientation.

2.9 Error Estimate

The fit of the line positions at negative frequencies were worse because of the offset-dependent phase distortion. However, this error will not give errors larger than the linewidth of the resonance. The error in the fit is assumed to be uniform for all four peaks at a single orientation and is based on the root mean square (rms) error of the fitted spectrum to the experimental one, normalized by the intensity of the calculated spectrum. The estimated error at each orientation is used in a weighted least squares fit of the quadrupole parameters for the rotation patterns. The resulting fits yield a value of $3e^2qQ/2I(2I-1)\,h = 0.9 \pm 0.1$ MHz with asymmetry parameter 0.0 ± 0.2. Carlos and co-workers [7] performed their experiments at 12.0 T and obtained a quadrupole coupling parameter of 2.5 MHz with an asymmetry parameter of 0.2, assigned to the next nearest neighbors. The next next nearest neighbor As atoms (NNNN) also possess the same symmetry properties. The ratio of the distance between the indium atom to the NNNN and NNN is 1.3. The $1/r^3$ dependence of the quadrupole coupling constant [7] results in an expected quadrupole coupling constant of 1.1, satisfactorily close to the obtained value of 0.9 MHz, since this radial dependence is derived from continuum arguments and is only approximate.

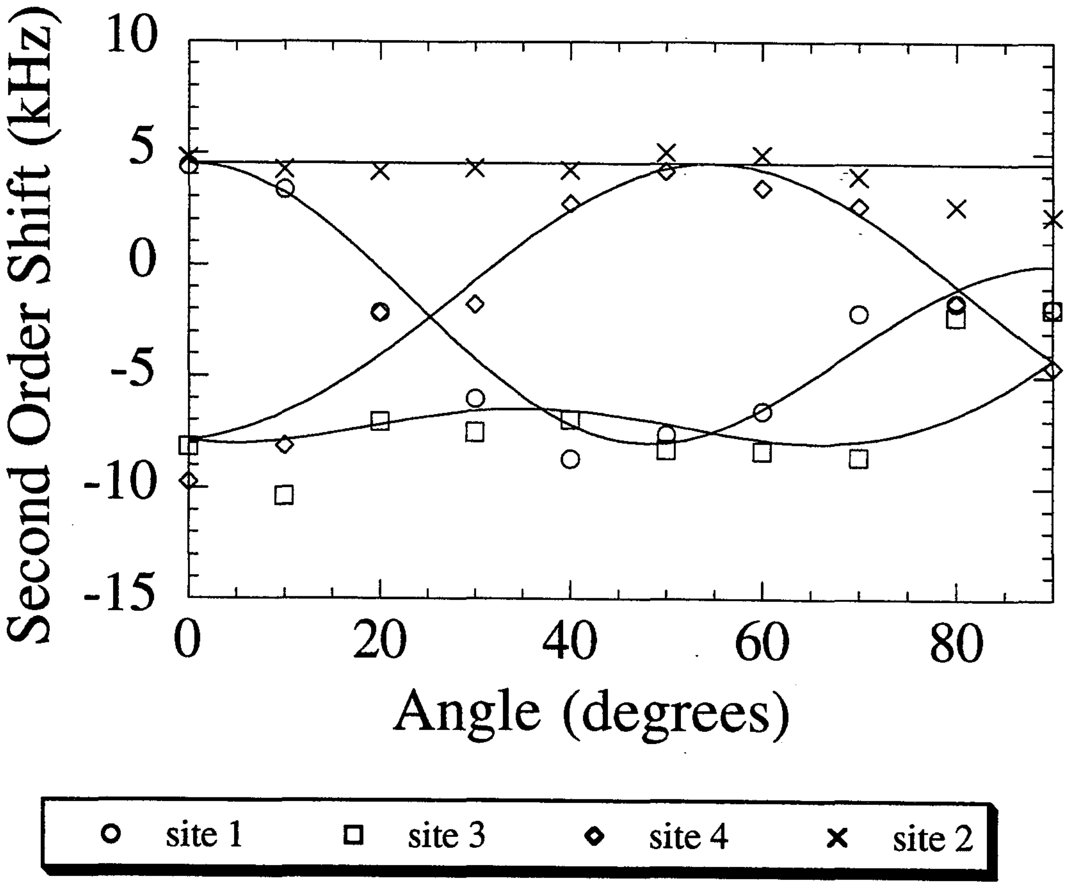

Figure 33. The peak positions have been fitted to the (110) sites. Based on error estimates in the line widths, a weighted least squares fit has been performed yielding a quadrupole coupling constant of $3e^2Q/2I(2I-1)\,h = 0.9 \pm 0.1$ MHz with asymmetry parameter 0.0 ± 0.2.

2.10 Observation of Additional Quadrupole Perturbed Sites

NMR nutation is a promising technique for studying semiconductors because it is possible to separate signals based on the size of the quadrupole coupling. The broad underlying peak has been indirectly attributed to first order quadrupole satellites from sites of intermediate distance experiencing strain from the indium dopant. Analysis of the 2D nutation data show that the diagonal lines radiating from the central transition at the nutation frequency of ω_1 are first order quadrupole satellites (figure 34).

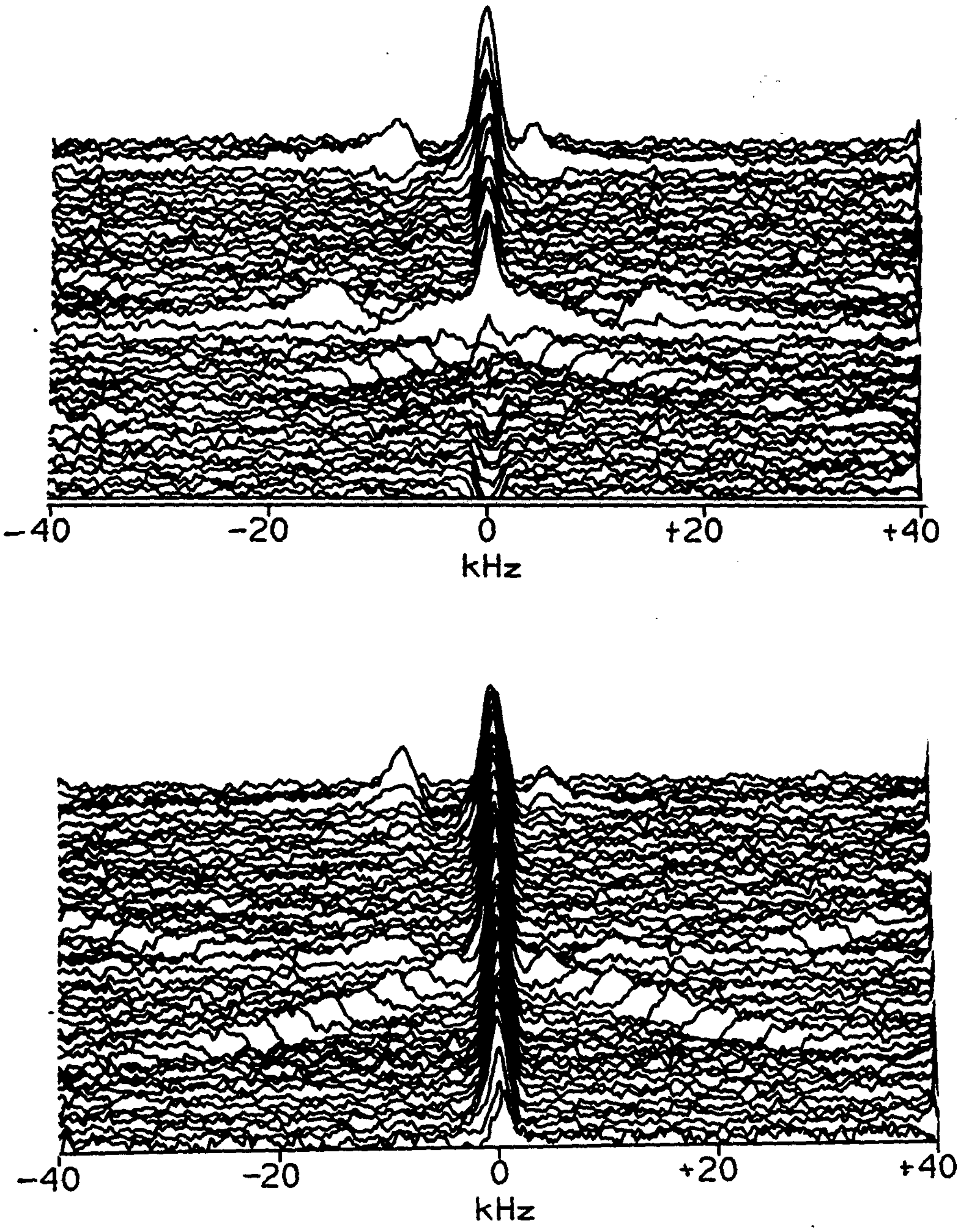

Figure 34. Stacked plot of real and imaginary components of 2D nutation spectrum.

As an example, two NMR spectra corresponding to nutation frequencies of 15 kHz and 35 kHz are analyzed with the formalism developed in the previous section. Figure 35 is the free evolution spectrum at a nutation frequency equal to half of ω_1. Using the observed value ofν_Q = 34 kHz, equation 28 yields $\omega_{nut}/2\pi$ = 17 kHz which is close to the experimental value of 15 kHz. For other nutation frequencies less than ω_1, the observed quadrupole splittings agree with the those calculated with equation 28.

For nutation frequencies greater thanω_1, two peaks are predicted and are observed. Figure 36 is a slice from $\omega_{\mathrm{nut}}/2\pi$ = 35 kHz with two sets of quadrupole satellites at 8 and 25 kHz marked by arrows 1 and 2. The nutation frequency is 5 kHz above $\omega_1/2\pi$. Using the observed quadrupole splittings, a nutation frequency of 33.8 kHz is calculated with

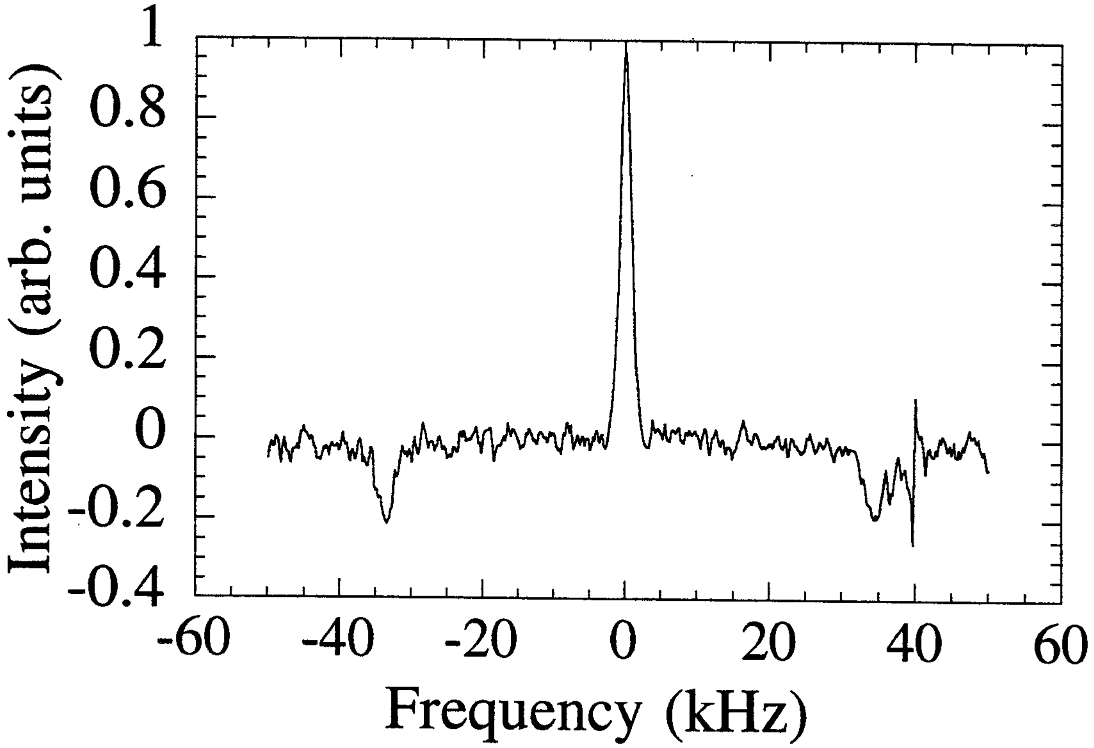

Figure 35. ^{75}As spectrum at nutation frequency of 15 kHz. The peaks at ± 34 kHz correspond to first order quadrupole satellites. The signal at 34 kHz is distorted by a sharp signal at 40 kHz possibly due to rf leakage into the receiver of the spectrometer.

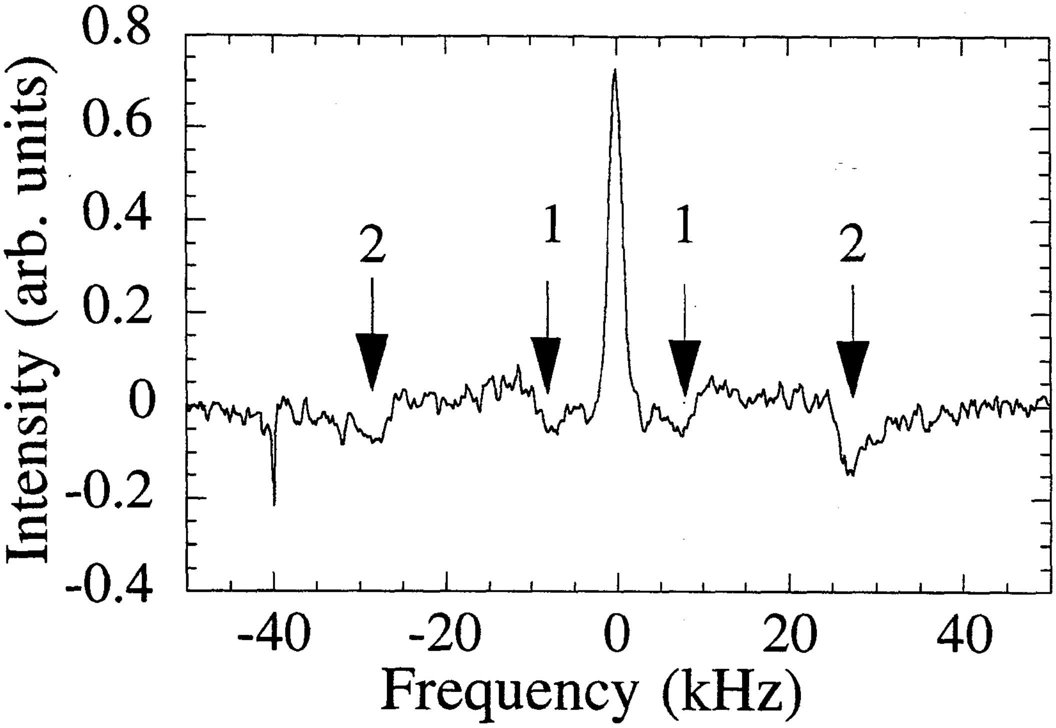

Figure 36. Nutation slice at 35 kHz, 5 kHz higher than $\omega_1/2\pi$.

equation 29 (transition $\Delta E_{2\text{-}4}$) for peak 1 and 33.6 kHz with equation 30 (transition $\Delta E_{3\text{-}2}$) for peak 2 which agrees with the observed nutation frequency. In general, the quadrupole satellite positions agree with the corresponding nutation frequencies for both ω_{nut} greater than ω_1 and for ω_{nut} less than ω_1.

To verify that NMR excitation is taking place throughout the entire spectral width, a one-dimensional echo spectrum was performed for various offset frequencies. A 50 kHz offset still results in approximately the same signal intensity shown in figure 37.

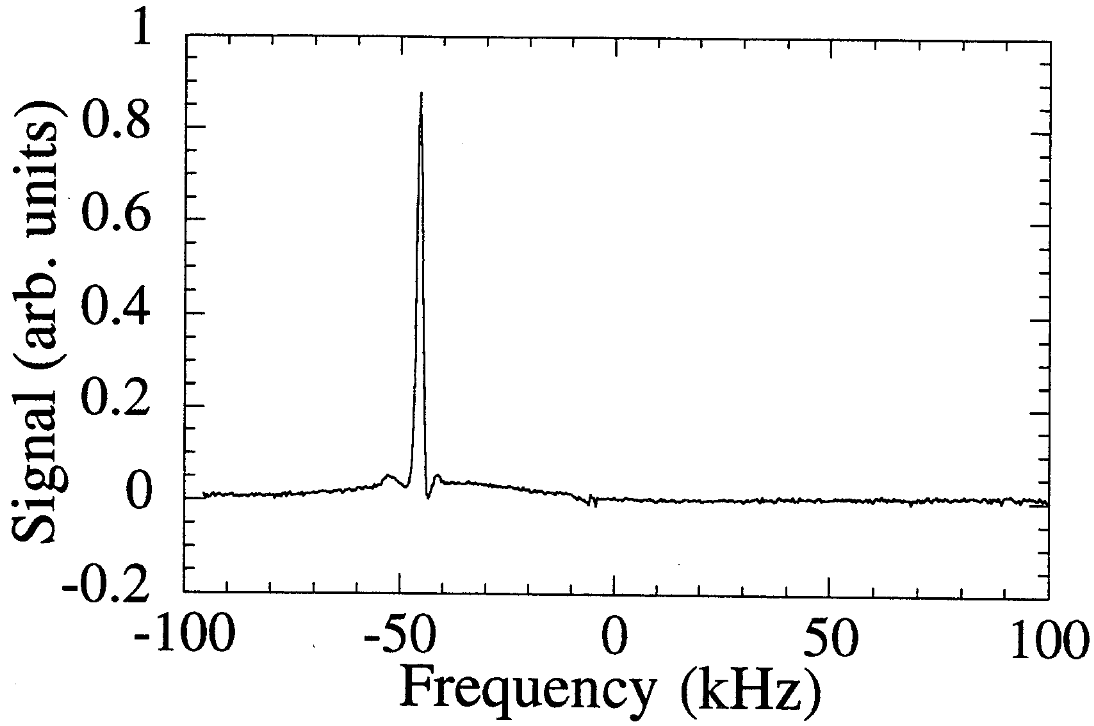

Figure 37. Verification of NMR excitation at 50 kHz offset.

2.11 Estimates of the Extent of Clustering

The 2D nutation spectrum can yield information about the extent of indium clustering. For a dopant concentration of 9×10^{19} indium atoms/cm^3, each indium atom occupies an average volume contained in a sphere of radius 14 Å. According to table 4, the 30th shell is 13.8 Å from the indium atom. Based on the symmetry of the EFG responsible for the well resolved second order shifted peaks nutating at $2\omega_1$, these peaks correspond to 12 sites posessing (110) symmetry. The data indicate that only a few percent of the sites possess quadrupole splittings which are smaller than the intrinsic spin-spin linewidth of ^{75}As. These sites are considered to be unperturbed by the indium atoms. Using the continuum approximation, the quadrupole splitting is expected to fall off as $1/r^3$. If the NNN sites possess a quadrupole splitting of 2.5 MHz, then the outermost atoms will have a splitting of 97 kHz. In this model of uniformly distributed indium atoms, no sites are left unperturbed. Experimentally, the indium atoms are expected to be distributed randomly so that some sites will be significantly farther from any indium atom than that calculated with the uniform distribution model. The small percentage of unperturbed sites indicates that clustering is unlikely. The presence of a large fraction of unperturbed ^{75}As nuclei would indicate a significant amount of indium clustering.

2.12 Conclusions

The 2D NMR nutation spectrum has been shown to be a powerful tool for studying solids with distributions of quadrupole splittings. Previously, a distribution of well resolved first order quadrupole satellites have been observed in 2D nutation NMR experiments on powdered salts. This results from the high number of defects found in powdered samples. In these investigations, quadrupole satellites in a single crystal has been resolved with a 2D nutation experiment. These satellites result from the strain field resulting from the distortion necessary to accomodate the indium atoms into the lattice. These signals were observable because of the relatively high (part per thousand) concentration of the dopant. The resolution provided by the 2D nutation spectrum has allowed the unambiguous determination of the origin of the broad underlying peak in the NMR spectrum as being due to the first order satellites. The relative intensity of the lines provide information about the extent of clustering of the indium atoms. Comparison of the NMR intensity of the unperturbed and strongly perturbed sites reveals that only a few percent of the sites are unperturbed. Assuming that the indium atoms are primary responsible for the observed lattice perturbation, the clustering is not significant.

The 2D nutation experiment was able to improve the resolution of the second order shifts of the central transitions, thus aiding the assignment to sites possessing (110) symmetry. The results of the fit yield a quadrupole coupling constant $\nu_Q = 0.9 \pm 0.1$ MHz with an asymmetry parameter $\eta = 0.0 \pm 0.2$. This differs from the value of $\nu_Q =$ 2.5 MHz and asymmetry parameter $\eta = 0.2$ obtained by other researchers at higher field

[7]. The difference in quadrupole coupling constants indicates that different sites possessing the same symmetry are observed in the two experiments. The uncertainty in the measurement of the asymmetry parameter is due to the offset dependent phase distortion.

Unfortunately, this technique is limited by sensitivity. Even though the indium concentration was $9 \times 10^{19}/\text{cm}^3$, the In NMR signal was unobservable. To study defects and dopants common in device grade materials, a much more sensitive technique is necessary. This is a motivation for pursuing the development of novel techniques for the optical detection of NMR in GaAs.

2.13 References

[1] Torrey, H.C., *Transient Nutations in Nuclear Magnetic Resonance,* Phys. Rev., **76,** 1059 (1949).

[2] Samoson, A., and Lippmaa, E., *Excitation phenomena and line intensities in high-resolution NMR powder spectra of half-integer quadrupolar nuclei,* Phys. Rev. B, **28**, 6567 (1983).

[3] Vegard, L., *Die Konstitution der Mischkristalle und die Raumfüllung der Atome,* Z. Phys., **5**, 17 (1921).

[4] Nordheim, L., *Zur Elektronentheorie der Metalle. I,* Ann. Phys. (Leipz.), **9**, 607 (1931).

[5] Wooley, J.C., and Smith, B.C., *Solid Solution in* $A^{\mathrm{III}}B^{\mathrm{V}}$ *Compounds,* Proc. Phys. Soc. London, **72**, 241 (1958).

[6] Mikkelsen, J.C., and Boyce, J.B., *Extended x-ray-absorption fine-structure study of* $Ga_{1-x}In_xAs$ *random solid solutions,* Phys. Rev. B, **28**, 7130 (1983).

[7] Carlos, W.E., Bishop, S.G., and Treacy, D.J., *Nuclear-magnetic-resonance studies of strain in isovalently doped GaAs,* Phys. Rev. B, **43**, 12512 (1991).

[8] Boyd, H.E., *An Investigation of Shallow Donor Impurities in Silicon by Endor*, Thesis, 1968.

[9] Slichter, C.P., *Principles of Magnetic Resonance* (Springer-Verlag, Berlin Heidelberg, 1989).

[10] Abragam, A., *Principles of Nuclear Magnetism* (Clarendon Press, Oxford, 1961).

[11] Zare, R.N., *Angular Momentum* (John Wiley and Sons, New York, 1988).

[12] Bouten, M., *On The Rotation Operators in Quantum Mechanics,* Physica, **42**, 572 (1969).

[13] Engelhardt, G., Buhl, J.-C., and Felsche, J., *Resolution Improvement of Solid-State Two-Dimensional* ^{23}*Na Nutation NMR Spectra by Magic Angle Spinning,* Chemical Physics Letters, **153**, 332 (1988).

[14] Janssen, R., Tijink, G.A.H., and Veeman, W.S., *Rotary Echo Nutation NMR,* J. Chem. Phys., **88**, 518 (1988).

[15] Kushibiki, N., Tsukamoto, M., and Erata, T., *Solid-State High Resolution NMR Studies on Gallium Arsenide and Indium Gallium Arsenide Semiconductors,* Chemical Physics Letters, **129**, 303 (1986).

[16] Janssen, R., and Veeman, W.S., *Quadrupole Nutation Nuclear Magnetic Resonance in Solids,* J. Chem. Soc., Faraday Trans. 1, **84**, 3747 (1988).

[17] Shulman, R.G., Wyluda, B.J., and Hrostowski, H.J., *Nuclear Magnetic Resonance in Semiconductors. III. Exchange Broadening in GaAs and InAs,* Phys. Rev., **109**, 808 (1958).

[18] Bloembergen, N., and Rowland, T.J., *Nuclear-Spin Exchange in Solids:* Tl^{203} *and* Tl^{205} *Magnetic Resonance in Thallium and Thallic Oxide,* Phys. Rev., **97**, 1679 (1954).

[19] Han, O.H., Timken, H.K.C., and Oldfield, E., *Solid-state "magic-angle" sample-spinning nuclear magnetic resonance spectroscopic study of group III-V (13-15) semiconductors,* J. Chem. Phys., **89**, 6046 (1988).

[20] Spaeth, J.-M., Niklas, J.R., and Bartram, R.H., *Structural Analysis of Point Defects in Solids* (Springer-Verlag, Berlin Heidelberg, 1992).

Chapter 3: Applications of ODNMR to Semiconductor Studies

It has been nearly 25 years since Lampel discovered that irradiating semiconductors with circularly polarized light at band-gap energies, results in optical nuclear polarizations which can be detected with conventional NMR [1]. Since then, the pioneering work by groups at the A.F. Ioffe Physico-Technical Institute in St. Petersburg, Russia, and at the Ecole Polytechnique in Paris have allowed the resulting nuclear polarizations to be detected optically by measuring the luminescence polarization in GaAs [2]. This is a novel technique, with unprecedented sensitivity enhancements of 10^5 due to the large nuclear polarization, which has made possible the observation of NMR in single quantum wells [3]. Unfortunately, the restriction to quasi-steady state continuous wave (cw) methods has resulted in NMR line shapes which were either distorted by the high rf fields needed to see signals or broadened by the presence of spin-polarized electrons during NMR. These limitations inspired the development of time-sequenced optical NMR (TSONMR) by the Weitekamp group [4] which makes possible time-domain experiments, putting all of the well established techniques of multiple-pulse and multi-dimensional NMR at the disposal of optical NMR [5].

This chapter will review the development of the optical detection of NMR (ODNMR) in GaAs, and the recent developments in the Weitekamp group. TSONMR multiple-pulse experiments on bulk samples of GaAs at 77 K will be presented. Extension of this technique to multiple pulse line-narrowing experiments, at the low magnetic fields initially implemented, reveals that the rotating-wave approximation breaks down. This results from the neglect of the counter-rotating wave in linearly-polarized rf. The motivation for constructing a new ODNMR spectrometer at higher field and lower temperature will be discussed. The details of the cryogenic design will be presented in chapter 5 and experimental data with this spectrometer, in chapter 6.

3.1 Theory of Optical Orientation

GaAs is a direct band-gap semiconductor with a conduction band which is at an energy $E_g = 1.5$ eV (828 nm) above the top of the valence band (fig. 1). There is a valence band degeneracy ($J = 3/2$) at k = 0 between the heavy hole ($m_j = \pm 3/2$) and light hole ($m_j = \pm 1/2$) sub-bands. J is the total angular momentum quantum number, and m_j is

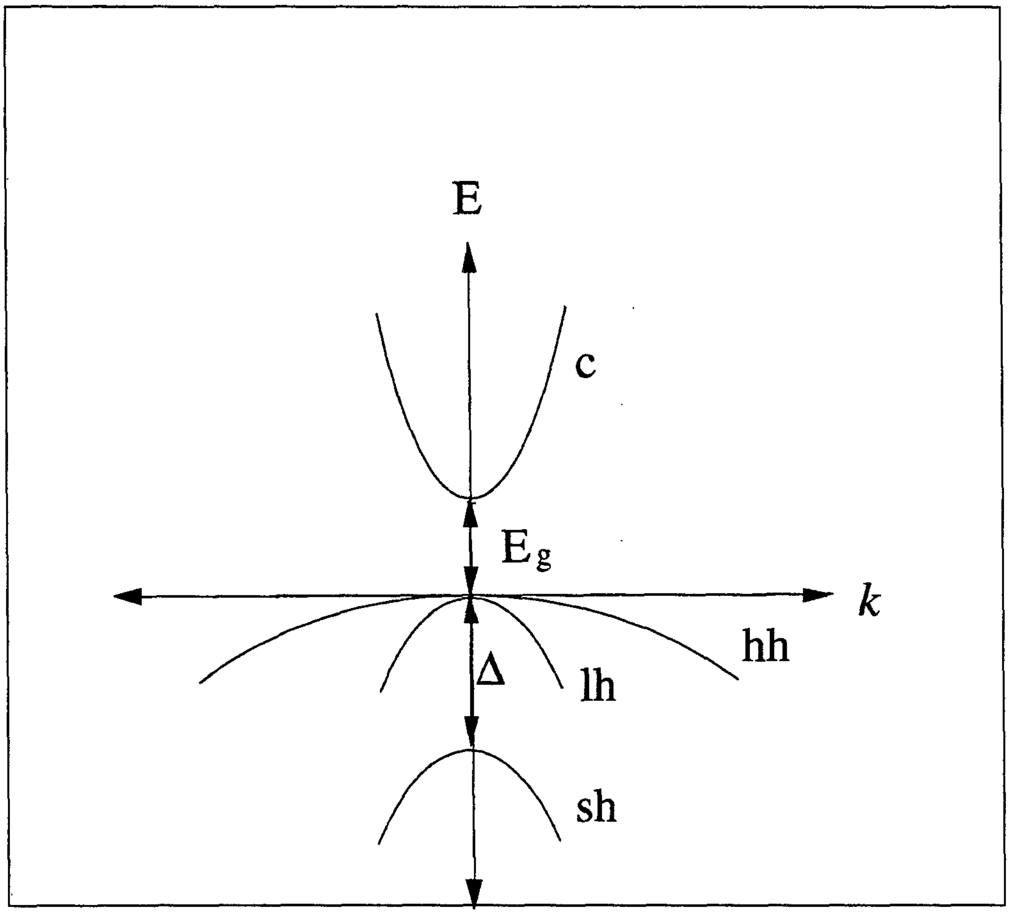

Figure 1. The band structure of GaAs. GaAs is a direct gap semiconductor with band-gap energy E_g. (c) denotes the conduction band, (hh) the heavy hole band with ($J = 3/2$, $m_j = \pm 3/2$), (lh) the light hole band ($J = 3/2$, $m_j = \pm 1/2$) and (sh) the split off band ($J = 1/2$, $m_j = \pm 1/2$), which lies at energy Δ below the conduction band edge. At 77 K, $E_g = 1.50$ eV (828 nm) and $\Delta = 0.30$ eV.

the magnetic quantum number. At energy Δ below the light hole valence band, there is a split-off band ($J = 1/2$ and $m_j = \pm 1/2$) resulting from the spin-orbit interaction.

The allowed transitions are governed by the same dipole selection rules governing atomic states $J = 3/2$ ($^2P_{3/2}$) and $J = 1/2$ ($^2S_{1/2}$). Figure 2 summarizes the selection rules for irradiation with left (σ^+ dashed line) and right (σ^- solid line) circularly polarized light along with the relative intensities [2]. Irradiation of the sample with σ^+ light will

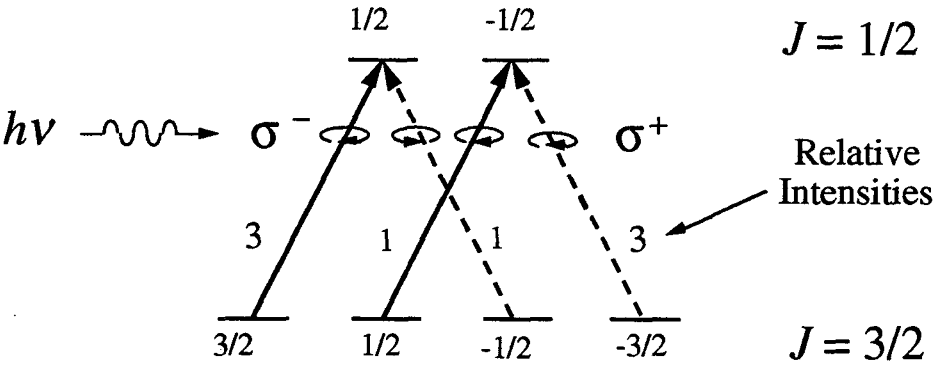

Figure 2. Selection rules for GaAs. The solid lines represent irradiation by σ^- light and the dashed lines by σ^+ light. The circular arrows indicate circularly polarized light and the vertical arrows represent linearly polarized light.

result in the excitation of the transition $m_j = -3/2 \rightarrow -1/2$, and $m_j = -1/2 \rightarrow 1/2$ with an intensity ratio of 3:1. The resulting polarization is $P_e = -1/2$ with P_e defined by

$$P_e = \frac{n_+ - n_-}{n_+ + n_-}. \tag{1}$$

where n_+ and n_- are the numbers of electrons in the conduction band with spin up and down, respectively. P_e is related to the electron spin expectation value along the optical axis by $S = 1/2\, P_e$, where the factor of 1/2 is the spin quantum number of the electron. In heterostructures, the degeneracy of the light and heavy holes is split. By choosing wavelength to selectively irradiate the heavy-hole band, it is possible to achieve polarizations of $P_e = -1$, and luminescence polarization ρ of up to 80% has been observed in a GaAs quantum well [3]. The measured quantity ρ is defined as (eq. 2)

$$\rho = \frac{I_+ - I_-}{I_+ + I_-} \tag{2}$$

where I_+ and I_- are the intensities, respectively, of the detected right and left circularly polarized luminescence. A simple relationship exists relating ρ and P_e since the same selection rules apply in emission. In bulk GaAs, electrons with spin m = 1/2 will result in 50% circular polarization in one direction and those with m = -1/2 will result in 50% circular polarization in the opposite direction. Thus [6]

$$\rho = -\frac{1}{2}P_e \tag{3}$$

This relationship is generalized by replacing the factor of 1/2 with the constant C where C = 1/2 for bulk samples and C = 1 for heterostructures [7].

$$\rho = -CP_e \tag{4}$$

Substituting $S = 1/2P_e$, we obtain

$$\rho = -2C\boldsymbol{S} \bullet \boldsymbol{n} \tag{5}$$

where $\boldsymbol{n}$ is the unit vector in the direction of observation.

The observed circular polarization ρ will be the steady state value resulting from the competition between spin relaxation and recombination lifetime. Defining T_{1e} as

$$\frac{1}{T_{1e}} = \frac{1}{\tau} + \frac{1}{\tau_s}, \tag{6}$$

where τ and τ_S are the recombination lifetime and the spin relaxation time [8], the average electron spin for detection parallel to the incident light is

$$\langle S_z \rangle = \frac{1}{2}\frac{C}{(1+\tau/\tau_s)} = C\frac{T_{1e}}{2\tau} \tag{7}$$

Combined with equation (5), the luminescence polarization is

$$\rho = -C^2\frac{T_1^e}{\tau} \tag{8}$$

If $\tau >> \tau_S$, then $\rho = 0$. The observation of the optical orientation of electrons is possible because the spin relaxation time is comparable to or longer than the recombination time.

3.2 Optical Nuclear Polarization

The spin-polarized photoelectrons are able to polarize the nuclei by the process of dynamic nuclear polarization (DNP) via the hyperfine interaction (eq. 9) [1,9,10].

$$H_{hf} = AI \bullet S|\Psi(0)|^2 \tag{9}$$

where $A = \frac{2}{3}\mu_0 g_0 \mu_B \gamma h$ with μ_0 is the magnetic permeability, g_0 is the free electron g-factor, μ_B is the Bohr magneton, γ is the nuclear gyromagnetic ratio, and $\Psi(0)$ is the electron wave function at the nucleus. When these interactions are averaged over the occupied electronic states q, for a nucleus i at position r_i, the resulting interaction is equivalent to an effective magnetic field B_e^i acting on the nucleus (eq. 10) [11,12]

$$B_e^i = (A_i/\gamma_i)\sum_q \langle S_q \rangle |\Psi_q(r_i)|^2 \tag{10}$$

The DNP is most efficient for nuclei near localized electrons where the electron wave function is largest. In bulk p-type samples, the conduction electrons are localized on defect sites of unknown identity, called optically relevant defects (ORDs). The steady-state nuclear spin polarization $\langle I \rangle$ is proportional to the electron spin polarization and occurs within the region of carrier localization and in adjoining regions within the range of spin diffusion through nuclear spin-spin couplings [9]. The proportionality is [9]

$$\langle I \rangle = f\frac{I(I+1)}{S(S+1)}\langle S \rangle \tag{11}$$

The leakage factor f ($0 < f < 1$) accounts for other mechanisms of relaxation which drive the I spins toward thermal equilibrium with characteristic relaxation time T_{1f} [12].

$$f = \frac{T_{1f}}{T_{1e} + T_{1f}} \tag{12}$$

It has been observed that results for nuclear polarization are more accurately described by providing a leakage factor for each nucleus, assuming that the primary relaxation mechanism is the quadrupole interaction [13]. The length scale of both localization and spin diffusion during the several seconds of the experiment can be estimated to be $\cong 10$ nm.

In turn, the electrons experience a nuclear field B_n which the hyperfine-weighted average of the nuclear polarizations [11]

$$B_n^q = \frac{2\mu_0}{3}\frac{g_0}{g^*}\hbar\sum_i \gamma_i I_i \left|\Psi_q(r_i)\right|^2 \tag{13}$$

where g^* is the effective g-factor of the electron. Nuclear fields of 170 kGauss have been predicted, and, experimentally, fields as large as 17 kGauss have been observed, corresponding to a leakage factor of $f = 0.1$ [12].

3.2.1 Nuclear Alignment in the Presence of an External Magnetic Field

The system of the electrons and nuclear spins form a tightly coupled system. When the sample is placed in an external longitudinal magnetic field B_0 parallel with the exciting light, the magnetic field increases the electron polarization (eq. 14)

$$\langle S_z \rangle = S_0 \frac{1}{1 + \tau / \tau_s(B_0)} \tag{14}$$

where the electron spin τ_s is a function of the external field B_0. This results in an increase of the nuclear polarization which will, in turn, feed back on the electrons. Dyakonov and Perel' [10] derived the magnetic field dependence of the electron spin relaxation time which depends on the fluctuating field associated with the electron hops between shallow donors. The field dependence of the electron spin-lattice relaxation time is

$$\frac{1}{\tau_s(B_0)} = \frac{1}{\tau_s(0)}\left[1 + \left(\frac{B_0 + \eta B_N}{B_\gamma}\right)^2\right]^{-1} \tag{15}$$

where B_N is assumed to be proportional to $\langle S \rangle$ (eq. 11), B_γ is the frequency of the hops expressed in field units of Gauss, $\tau_s(0)$ is the electron spin-lattice relaxation time in zero magnetic field, and η is a coefficient which depends on the mechanism of electron spin relaxation ($0.1 < \eta < 1$). This theory is found to be in reasonable agreement with experiment [14]. The calculated field dependence is shown (fig. 3) for the parallel and antiparallel geometry with parameters commonly encountered in experiments. The dashed line represents the magnetic field dependence of the electron spin polarization in the absence of nuclear effects.

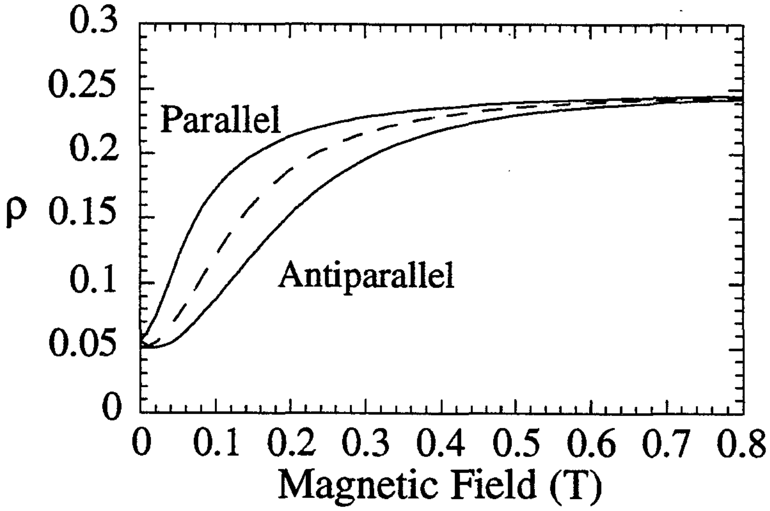

Figure 3. Banana curve simulation. The parameters used in this simulation are $B_\gamma = 600$, $\beta = 4000$, $S_0 = 0.25$, $\tau/\tau_s(0) = 4$.

At small values of magnetic field, the parallel orientation, in which nuclear polarization has the same orientation as the magnetic field, results in a greater degree of nuclear polarization. This is because the total field which is the sum of nuclear and external fields

$$B_T = B_n + B_0 \tag{18}$$

is greater than B_0, and thus the electron spin-lattice relaxation time is longer. The polarization of the light, rather than the applied field, determines the direction of the nuclear spin orientation. At large fields ($B_0 >> B_n$), the two curves approach asymptotically because τ_s is no longer sensitive to B_T.

3.3 Hanle Effect

The Hanle effect, originally discovered in the magnetic depolarization of fluorescence in gases [15], was first observed in semiconductors by Parsons [16] and is the effect by which NMR is optically detected in GaAs. The evolution of the average electron spin is governed by a Bloch-like equation, similar to the one used to describe classical NMR, but with time constant T_{1e}, defined in the previous section [12,17].

$$\frac{d\langle\vec{S}\rangle}{dt} = -\frac{\langle\vec{S}\rangle - \langle\vec{S}_0\rangle}{T_{1e}} - \frac{g^*\mu_B}{\hbar}\left(\langle\vec{S}\rangle \times B_T\right) \qquad (19)$$

In the presence of a magnetic field perpendicular to the detection axis, the steady-state solution of Eq. 19 for the z-component of the average spin, $\langle S_z\rangle$ is a Lorentzian given by

$$\langle S_z\rangle = \langle S\rangle_0 \frac{\Delta B^2 + B_z^2}{\Delta B^2 + B_T^2} \qquad (20)$$

where $\Delta B = \dfrac{\hbar}{g^*\mu_B T_{1e}}$ is the Hanle width expressed in field units.

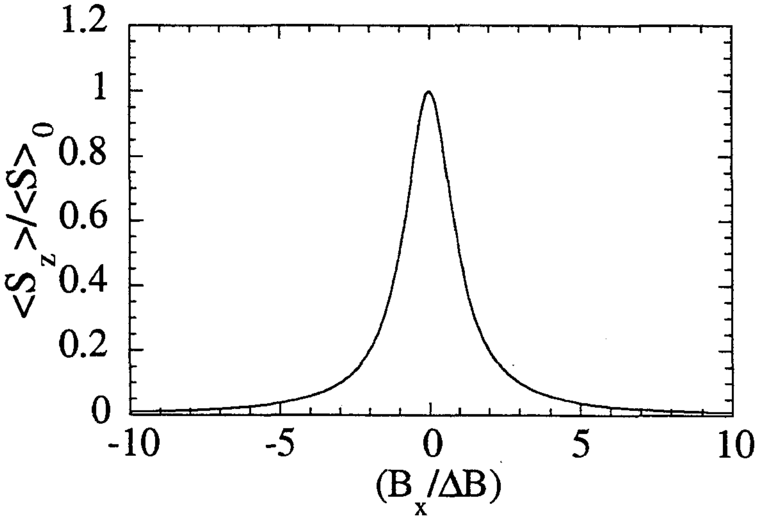

Figure 4. The Hanle depolarization curve is a Lorentzian with width ΔB. As the transverse field is increased, there is a progressive depolarization of the optically detected signal ρ. The axes are expressed in dimensionless units.

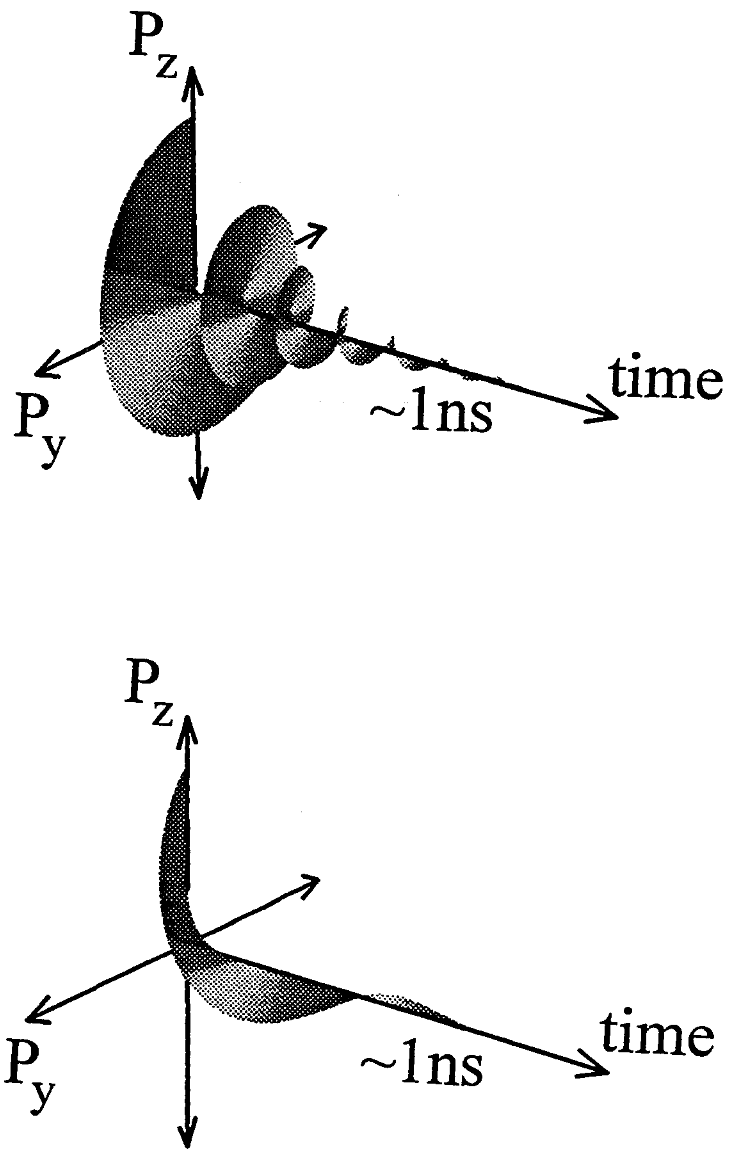

Figure 5. (a) A graphical illustration of the Hanle effect when the precession period is short compared to the electron spin relaxation time. The observed luminescence polarization is a measure of the time average of the electron polarization. The more precession periods before decay, the smaller the resulting polarization of luminescence. (b) A graphical illustration of the Hanle effect when the precession period is long compared to the lifetime of the oriented electron.

A time-domain view of the origin of the Hanle effect is illustrated in fig. 5. The screw axis represents time, and the other two axes span the S_y and S_z plane containing the electron magnetization $\langle \vec{S} \rangle$. For electrons with time constant T_{1e} long relative to the precession period, $\langle \vec{S} \rangle$ will precess several times about the transverse magnetic B_x field before decaying. The quantity $\langle S_z \rangle$, the spin component along the detection axis, will be small because its value is averaged over many precession periods (fig. 5a). When T_{1e} is short compared to the precession period, the electron spin will decay before completing one revolution. In this case, the average z-component of electron spin will be nonzero (fig. 5b).

3.3.1 Oblique Hanle Effect

In the presence of external fields, the total magnetic field $\vec{B}_T$ experienced by the electron is the sum of the nuclear and applied fields and can alternatively be expressed as $\vec{B}_T = \vec{B}(1+K)$ and K is the enhancement factor [12] defined by

$$K = f\, b_n \langle S \rangle_0 \frac{(\boldsymbol{B} + \Gamma_t b_e \langle S \rangle)}{B^2 + \xi B_L^2} \bullet \langle S \rangle \tag{21}$$

where Γ_t is the occupation time of the electron at the ORD, b_e is the proportionality constant relating electron spin to the electron field experienced by the nuclei, b_n is the corresponding factor for the nuclei, ξ is the relative relaxation rate of the dipolar and Zeeman energies, and B_L^2 is the value of the local fields experienced by the nuclei in the lattice. Substituting this into the expression for the Hanle effect, we get

$$\langle S_z \rangle = \langle S \rangle_0 \frac{\Delta B^2 + B_z^2 (1+K)^2}{\Delta B^2 + B^2 (1+K)^2} \tag{22}$$

Equations 21 and 22 represent a set of coupled equations which gives a cubic equation for the electron polarization $\langle S_z \rangle$. When multiple solutions exist under particular circumstances, oscillations have been observed [2]. The solution yields a curve which has a Lorentzian shape at large magnetic fields when $B \gg \Gamma_t b_e \langle S \rangle$, but exhibits complex feedback behavior when these values are comparable. In these small transverse magnetic fields, ONP results in the creation of large nuclear polarizations aligned along the direction of the total field ($(\boldsymbol{B}+\Gamma_t b_e\langle \boldsymbol{S}\rangle)$), oblique to the exciting light and external magnetic field. The large magnitude of the nuclear field depolarizes the electron spins more than the external field could by itself. As the transverse magnetic field increases, ONP efficiency decreases so the behavior approaches that of the Hanle depolarization curve in the absence of nuclear effects. Estimating the Hanle curve as a Lorentzian for large magnetic fields is a reasonable approximation, but only when the field and exciting light are exactly perpendicular. When the external magnetic field is oblique, a significant deviation from the Lorentzian shape can occur. The term "approximate" appears in the graph label because while these values were calibrated in the previous TSONMR apparatus, the value in the new apparatus , with similar geometry, has not.

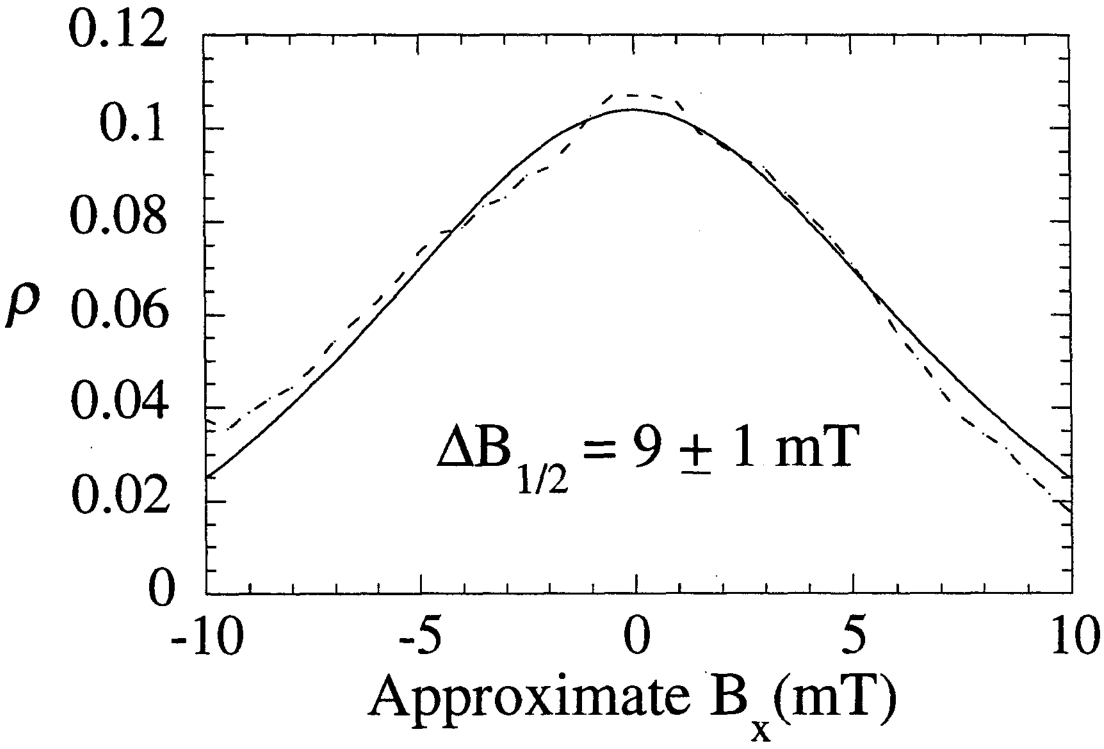

Figure 6. Hanle curve measurements with magnetic field perpendicular to the exciting light.

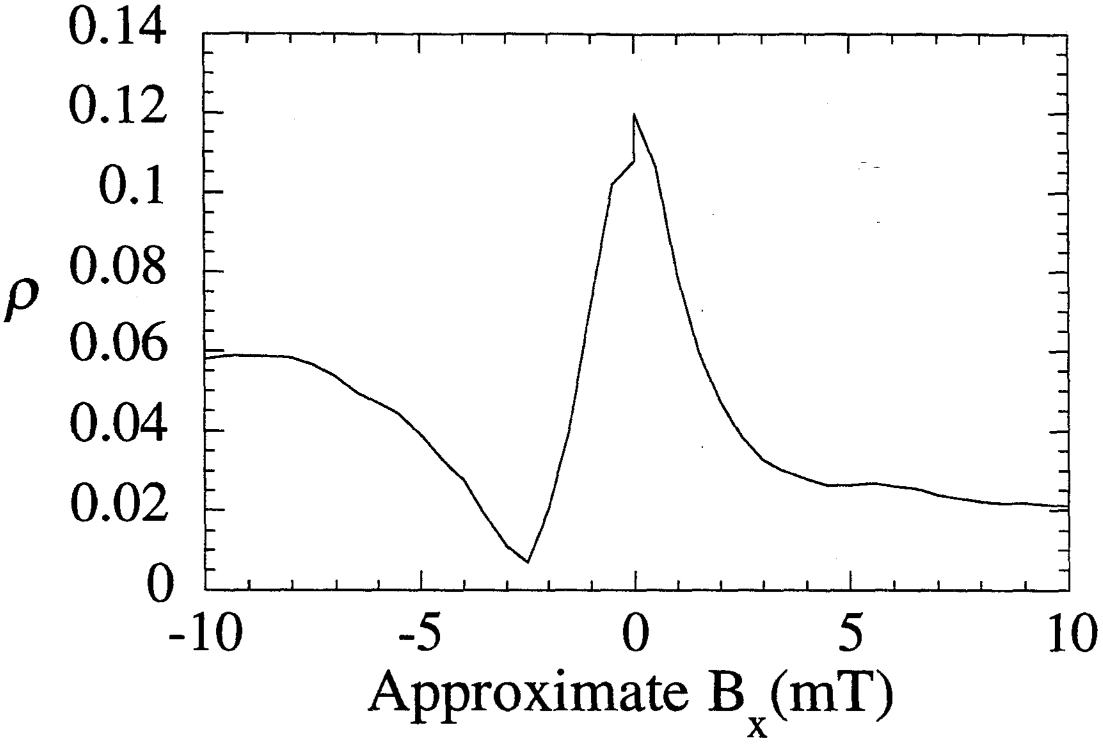

Figure 7. Oblique Hanle effect with magnetic field 10° off axis from exciting light.

Figures 6 and 7 show data from Hanle curve sweeps for the exciting light perpendicular (a) and oblique (b) for a GaAs heterojunction at 2 K to be discussed in chapter 5. In these measurements, it was only possible to sweep the transverse magnetic field from zero to 10 G in one direction. Negative values of the magnetic fields were obtained by changing the connections of the wires from the current source to reverse the polarity. Because the time constant of these nuclear effects are on the order of minutes, care was taken to minimize hysteresis effects when sweeping the transverse magnetic field. Each of the data sets were acquired by monitoring the luminescence polarization while sweeping the magnetic field from zero, up to the final value and back to zero. In the time scale of the experiment, the observed hysteresis effects were minimal. However, upon acquring data for the reverse polarity of the magnetic field, the observed value of the luminescence polarization in figure 7 was slightly different. Since only the difference in luminescence polarization was measured ($I_+ - I_-$) ,the data point at zero field was normalized with a denominator to yield the ρ ($B_x = 0$) equal to that observed at zero field.

3.4 Optical Detection of NMR

Because of the importance of the adiabatic rapid passage experiment for optically detecting NMR, this experiment will be discussed in detail. The motion of a magnetic moment $\vec{M}$ in a magnetic field $\vec{B}$ is described by the well known equation

$$\frac{d\vec{M}}{dt} = \gamma \vec{M} \times \vec{B} \tag{23}$$

A simplification in the description of the motion can be obtained by transforming into the rotating frame defined with angular velocity and direction $\vec{\omega}$. For an arbitrary time-dependent vector $\vec{A}(t)$, the derivative in the lab frame defined is related to that in the rotating frame by

$$\frac{d\vec{A}}{dt} = \frac{\partial \vec{A}}{\partial t} + \vec{\omega} \times \vec{A} \tag{24}$$

This expression allows us to transform the lab frame equation of motion into a rotating-frame equation of motion.

$$\frac{d\vec{M}}{dt} = \gamma \vec{M} \times \left(\vec{B} + \frac{\vec{\omega}}{\gamma} \right) \tag{25}$$

If $\vec{B}_{eff} = \vec{B} + \frac{\vec{\omega}}{\gamma}$, then equation 25 has the same form as equation 23, but with precession about $\vec{B}_{\text{eff}}$. By sweeping either the frequency of the applied rf field or the magnitude of the static field, the direction of $\vec{B}_{\text{eff}}$ can be changed continuously. If the changes are slow enough, the adiabatic theorem dictates that the magnetization will follow $\vec{B}_{\text{eff}}$. The conditions for adiabaticity are [9]

$$\frac{1}{T_1} << \frac{1}{B_1}\left|\frac{dB_0}{dt}\right| << |\gamma B_1| \cong T_2 \tag{26}$$

When far off resonance, $\vec{B}_{\text{eff}}$ is parallel to the magnetization and external magnetic field. During an adiabatic field or frequency sweep through resonance, the magnetization follows B_{eff}, and is spin-locked along this field. After passing through resonance, the magnetization is inverted relative to the external field. In ODNMR experiments, the transverse component of the magnetization is detected via the Hanle depolarization. The method of adiabatic rapid passage has the advantage of sensitivity and speed, but lacks resolution. The rf field must be significantly larger than the local fields to efficiently spin lock the magnetization, but the resulting linewidths are found to exceed the sum of the rf and local field strength. The other method of detection is the steady state cw method which observes NMR signals in the linear response regime by using small rf field strengths to tilt the magnetization by only a few degrees. Here, a steady state is reached between nutation by the rf field and spin-lattice relaxation. Because of the small tilt angles and small rf field strengths, this method yields better resolution, but is an order of magnitude less sensitive. The desire to improve both sensitivity and resolution was the impetus for the development of TSONMR [4].

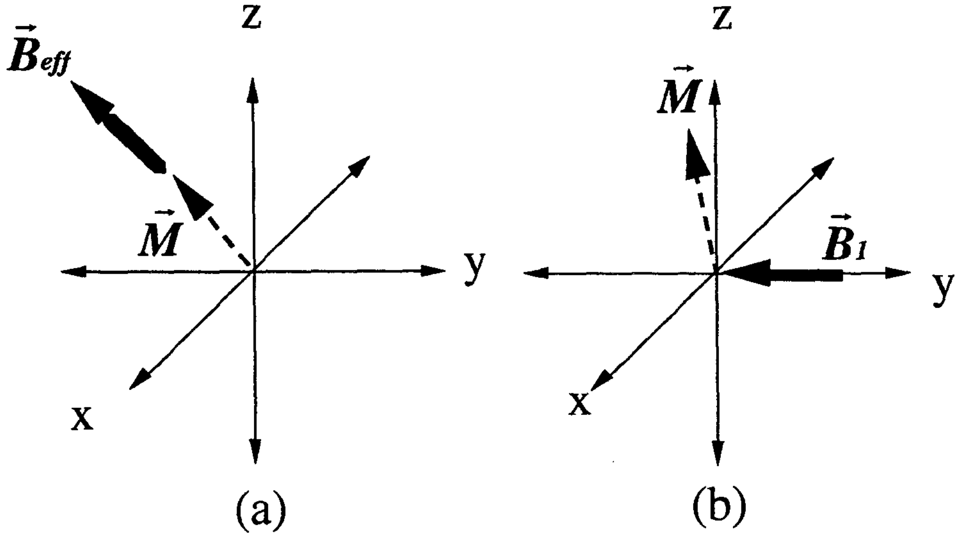

Figure 8. Illustration of the two (quasi)-steady state methods for detecting NMR. (a) Adiabatic rapid passage by spin locking along B_{eff}. (b) cw-steady state detection in linear response.

3.5 TSONMR

The introduction of TSONMR in which the optical nuclear polarization, NMR, and optical detection occur separately in successive periods has resulted in order-of-magnitude improvements in sensitivity and resolution over previous steady-state ODNMR methods where the three processes occur simultaneously. In addition to improvements in sensitivity and resolution, time-domain experiments are also possible with the TSONMR technique, allowing use of the well established techniques of multiple-pulse and multidimensional NMR at the disposal of optical NMR.

The general timing sequence of a TSONMR experiment is: (i) ONP until a steady-state nuclear spin polarization is achieved, (ii) a period of NMR to selectively modulate nuclear spin order, and (iii) OD to sensitively assess this modulation (fig. 9). During the ONP period of the TSONMR experiment, the sample is irradiated with circularly-polarized light near the band-gap energy in a magnetic field along the optical z axis.

Once a steady-state nuclear field is established, its value can be manipulated with NMR. The power of the TSONMR technique comes from the flexibility in the type of NMR experiment that can be performed. The NMR of the valence band can be measured by turning off the light. In this manner the resolution is maximized because NMR is performed in the absence of spin polarized photocarriers, which degrade spectral resolution. The rf field can be applied in a cw fashion or as a series of pulses and delays, the latter of which is more versatile, as evidenced by modern time-domain NMR spectroscopy.

After NMR takes place, the resulting signal is encoded as z-magnetization which is then optically detected through Hanle depolarization by the detection period transient (fig. 10). The nuclear field is first adiabatically rotated to a direction x perpendicular to the optical z axis by rotating the DC field. Restoring the band-gap light causes the newly-created photocarrier spins to precess in the field $B_T = B_n + B_0^d$ where B_0^d is the applied field during optical detection. The detection period transient in ρ is governed by a quasi-steady state Hanle depolarization by B_T

$$\rho(\omega, T_d) = 2C\langle S\rangle_0 \frac{\Delta B^2}{\Delta B^2 + B_T^2(\omega, T_d)} \tag{27}$$

and its variation is arranged to be linear in B_n. The NMR signal is the integral of the transient relative to a null experiment without rf irradiation.

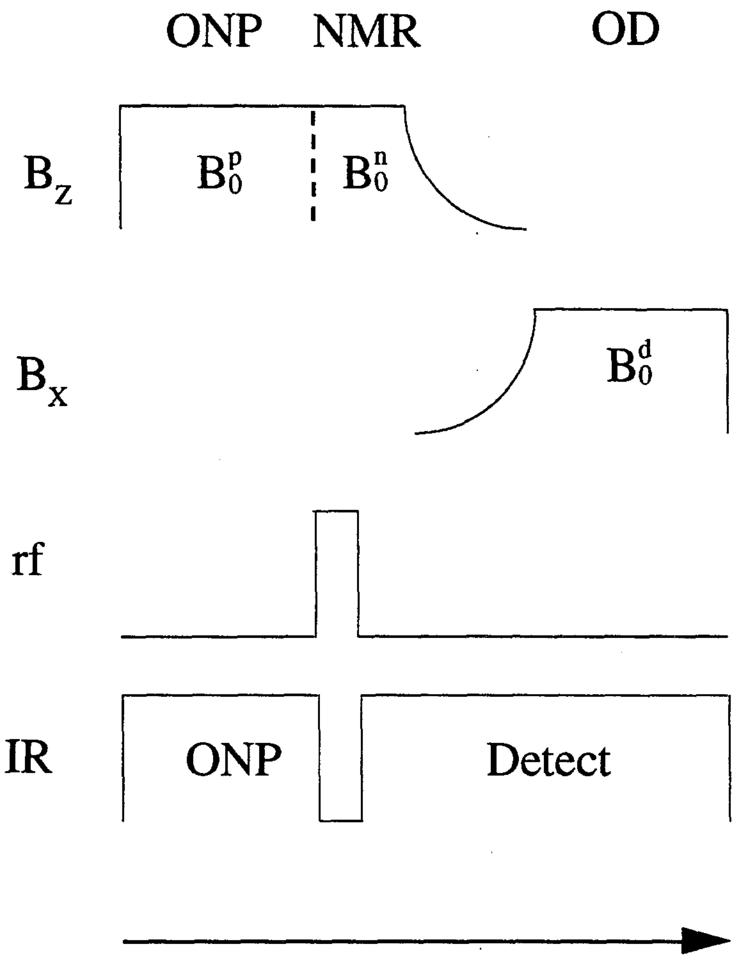

Figure 9. TSONMR timing sequence. The nuclei are optically polarized (ONP) during irradiation in the magnetic field B_0^p. The light is switched off during NMR in the same magnetic field B_0^n. Optical detection (OD) occurs after adiabatically rotating the field from the Z axis to the X axis where the nuclear field is detected by Hanle depolarization in the new transverse field B_0^d.

The signal $S(\omega)$ is optimized by selecting conditions under which $d\rho/dB_n$ is a maximum. Operationally,

$$S(\omega) = \mathcal{N}\int\int_0^{\infty}\left[\rho(\omega,t_d) - \rho_{null}(t_d)\right]\mathcal{W}(t_d)dt_d \qquad (28)$$

where $\mathcal{W}(t_d)$ is a weighting function to optimize signal-to-noise. The absolute optimum experiment necessitates that the reference field must necessarily be time-dependent where $B_0^d = B_0^d\,(t_d = 0)\,exp\,(\,-t_d/T_{1on})$. In practice, an optimized constant value of B_x is selected. This simpler approach sacrifices little sensitivity for samples where B_N is comparable to ΔB.

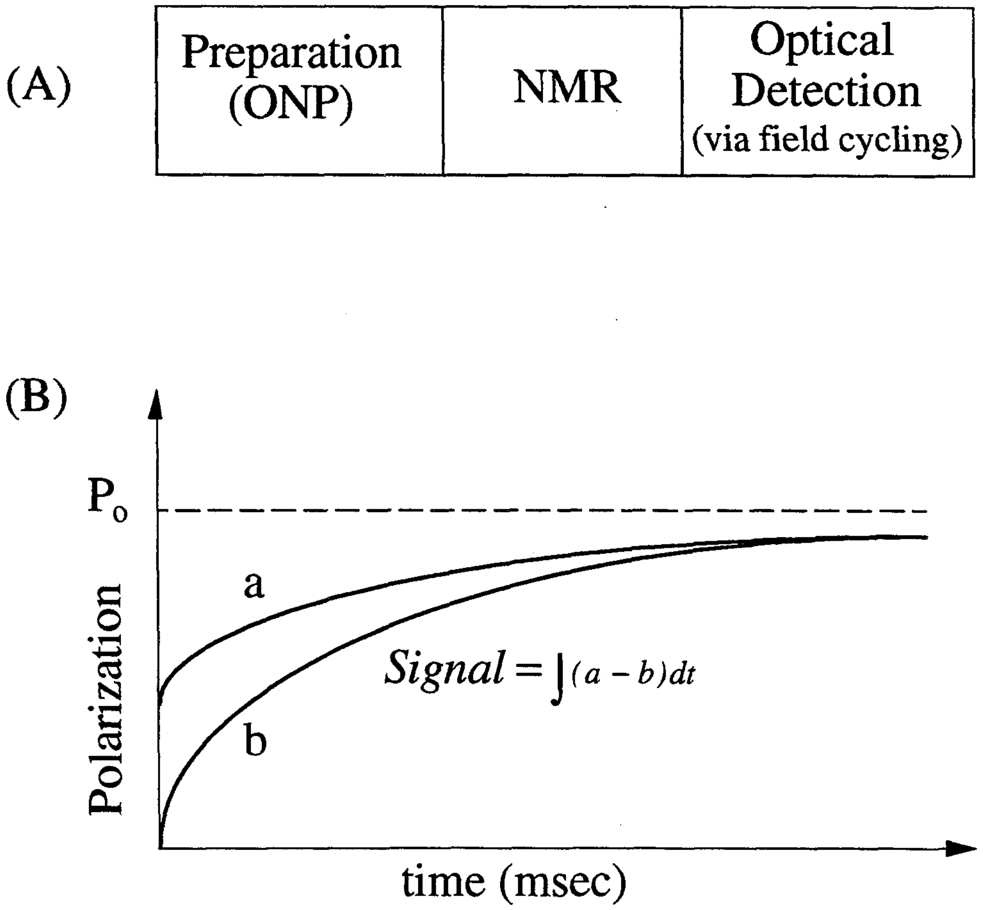

Figure 10. (A) TSONMR timing sequence. (B) NMR detection by field cycling.

3.6 Experiment

The NMR experiments of this section are performed at liquid nitrogen temperatures (77K) in a 115 Gauss longitudinal magnetic field. The details of the spectrometer are contained in the thesis of S.K. Buratto [7]. The experimental apparatus is shown in Figures 11a and b. The laser (Spindler and Hoyer, Inc. model DL25C single mode GaAs/GaAlAs laser diode) put out 30 mW (nominal) of linearly polarized continuous power at 780 nm. A $\lambda/4$ plate converted the linearly polarized laser beam into circularly polarized light.

A lock-in detection method is used to avoid low frequency noise. The total luminescence ($I_+ + I_-$) was modulated at 3 kHz with a chopper (Stanford Research model SR540). The combination of a photoelastic modulator (Hinds, model PEM-80) oscillating between $\pm\,\lambda/4$ retardation at 50 kHz and amplitude modulated right and left circularly polarized fluxes 180 degrees out of phase with each other results in a 50 kHz signal at the detector. Two lock-ins (Stanford Research, model SR530 and model SR510) were used to demodulate the sum and difference of I_+ and I_-. The quantity ρ, proportional to ($I_+ - I_-$), can be determined from the lock-in outputs by accounting for all the optical components (i.e., polarizers, etc.) [7,18].

$$\rho = \frac{Signal_{diff}\left(\frac{1}{2}\right)^{-1}\left(J_1(A_0)\right)^{-1}}{Signal_{sum}\left(\frac{2}{\pi}\right)^{-1}\left(\frac{1}{2}\right)^{-1}} \tag{29}$$

Evaluating the expression,

$$\rho = \frac{Signal_{diff}}{Signal_{sum}}(1.12) \tag{30}$$

where $Signal_{diff}$ and $Signal_{sum}$ are the output voltages of the lock-in amplifiers proportional to the sum and difference photocurrents. Measurements on the lock-in were acquired with 30 msec integration time. The optical detection bandwidth was selected with 10 nm bandwidth interference filters from Corion and Melles Griot for the 870 nm and 830 nm detection, respectively.

All single phase rf experiments used an HP 3335A synthesizer, followed by an rf switch from Merrimac (SE 11D-125). Quadrature rf was generated with the home built spectrometer documented in the thesis of M.H. Werner [19] with minor modifications to allow operation at 150 kHz. The frequencies were generated at 30 MHz+ω_0, where ω_0 is the Larmor frequency near 150 kHz. This frequency was subsequently mixed down in the transmitter controller with the 30 MHz signal from the rf quadrature source before sending the signal to the rf-amplifier. The impedance of the rf coil was matched to 50 ohms by adding 50 ohms in series to minimize the reflected power. The logic levels to control the rf switches were generated with an IT RS-670 word generator. The z-coils are home-built air-cooled magnets capable of generating 115 Gauss magnetic field.

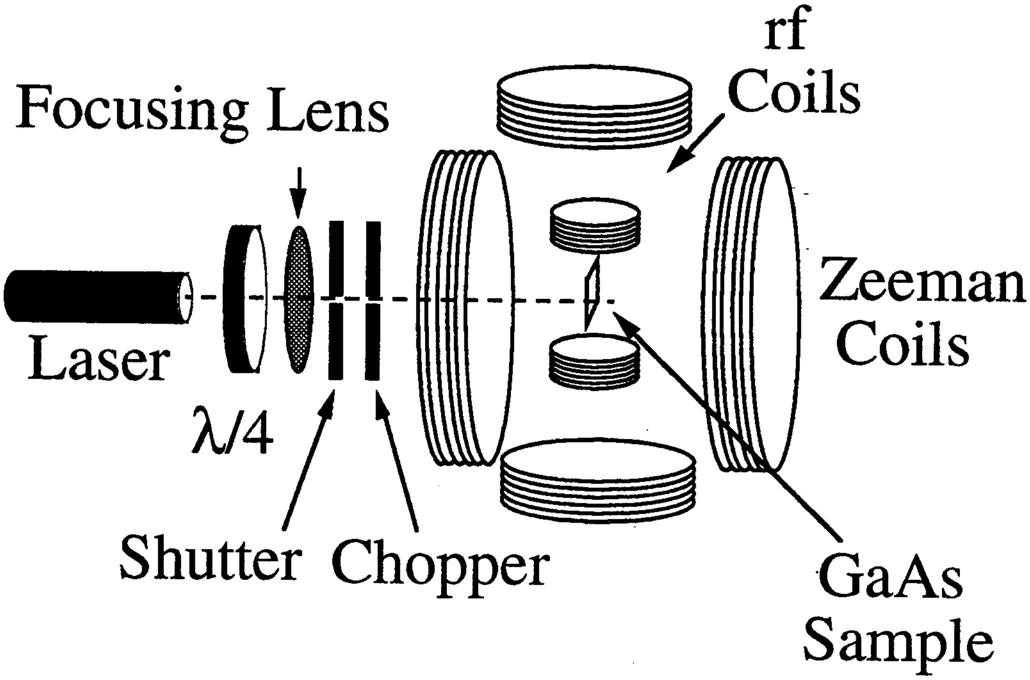

Figure 11. Schematic of excitation optics.

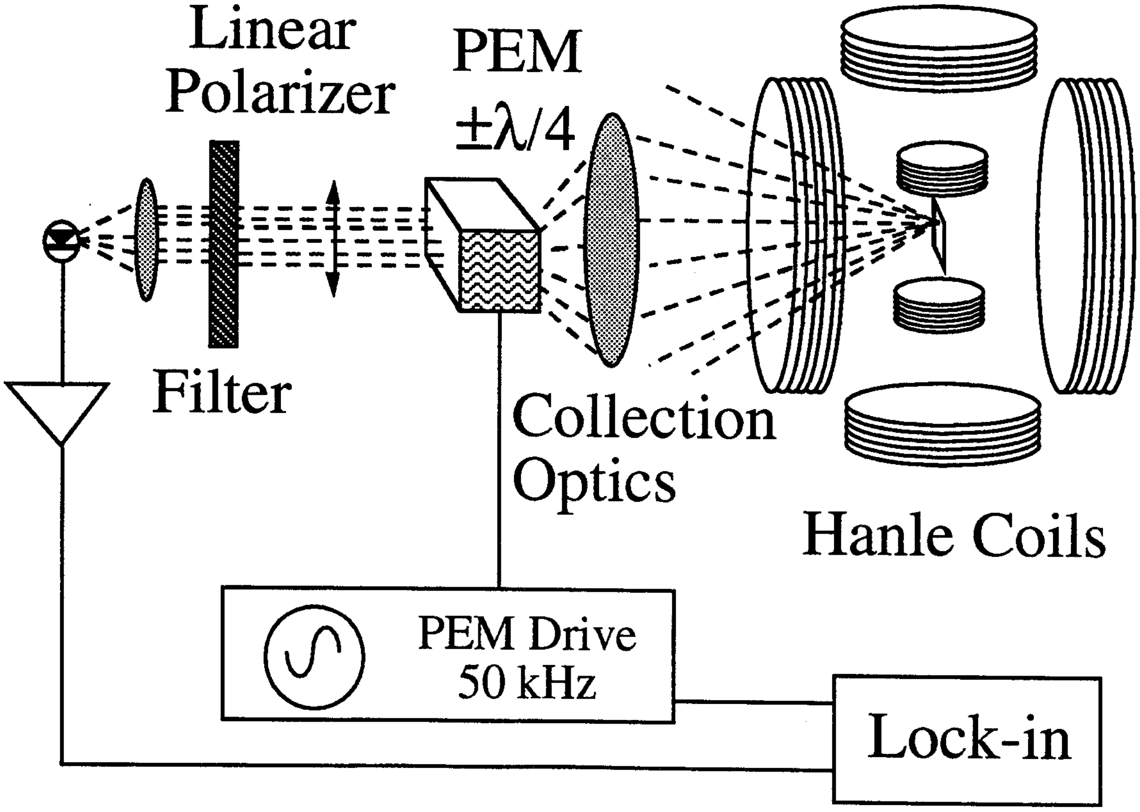

Figure 12. Schematic of detection optics.

3.6.1 GaAs Samples

The remaining experiments of this chapter were performed mostly with an MBE grown bulk GaAs sample doped with Zn ($10^{17}/cm^3$) [7], hereafter referred to as sample 5. The NMR experiments were detected at 870 nm luminescence using a 10 nm bandpass interference filter. Although more luminescence was present at 830 nm, the circular polarization at that wavelength was not measurably modulated by NMR. Another p-compensated sample has a 1μm $Al_xGa_{1-x}As$ cap with $x = 0.36$, followed by 3 μm of p-compensated GaAs on an undoped substrate (sample M303). The doping concentration is $N_d/N_a = 0.3$ with d = Si, and a = Be with $N_a = 2 \times 10^{18}/cm^3$ (N_a and N_d correspond to the number of acceptors and donors) [20]. Unlike Sample 5, NMR of the p-compensated sample was optically detected at 830, 860, and 870 nm. The NMR data to be presented were detected at 830 nm where the maximum luminescence was obtained.

The photoluminescence (PL) spectrum is associated with the light emitted from the semiconductor when electrons relax from the conduction band back to the valence band after excitation by a laser. These spectra can have resolved lines which are assignable to specific electronic states. Figure 13 is a PL spectrum of sample M303, a heavily doped p-compensated bulk GaAs sample. The spectrum is centered about 840 nm which is the band-gap energy of GaAs. The lack of well-resolved lines is attributed to the large number of donors and acceptors present in the sample which result in many states in the band-gap region. The sample was excited with a Spectra Physics 2020 Ar+ laser at 5145 Å at T = 4.7-5 K. The power density is approximately 1.4 W/mm^2. Detection was performed with a 1-meter SPEX 1704 monochrometer with 2 Å resolution.

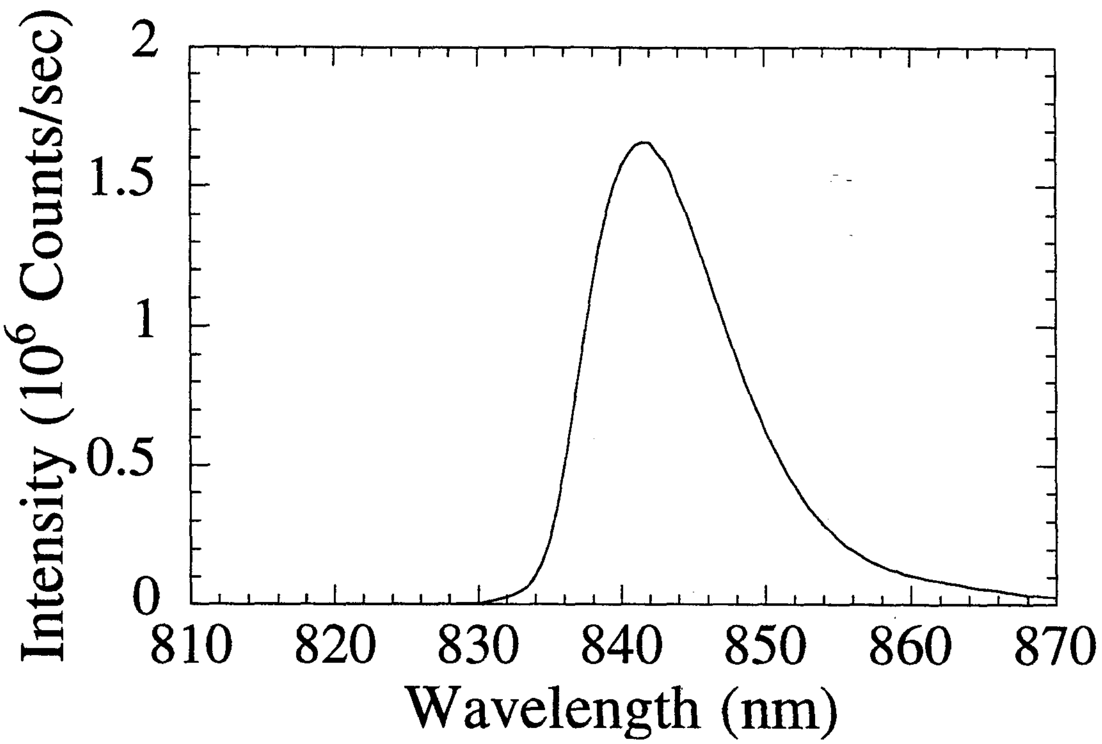

Figure 13. PL spectrum of sample M303, a p-compensated GaAs sample [21].

3.6.2 Background

From earlier work [7], a picture of the interplay between the optically relevant defects and the bulk sites began to emerge which explained the linewidth difference between the cw and FT-TSONMR spectra (figure 14). The source of the NMR signal and nuclear polarization is the optically relevant defect (ORD) around which the nuclei are coupled to the electrons by the hyperfine interaction. The size of this region is estimated to be approximately 100 Å [7]. At sites closest to the ORD, in a radius of 10Å, the nuclei experience both a strong hyperfine interaction and strong quadrupole coupling due to the perturbed lattice sites. As a result, only the central transition of the NMR spectrum is

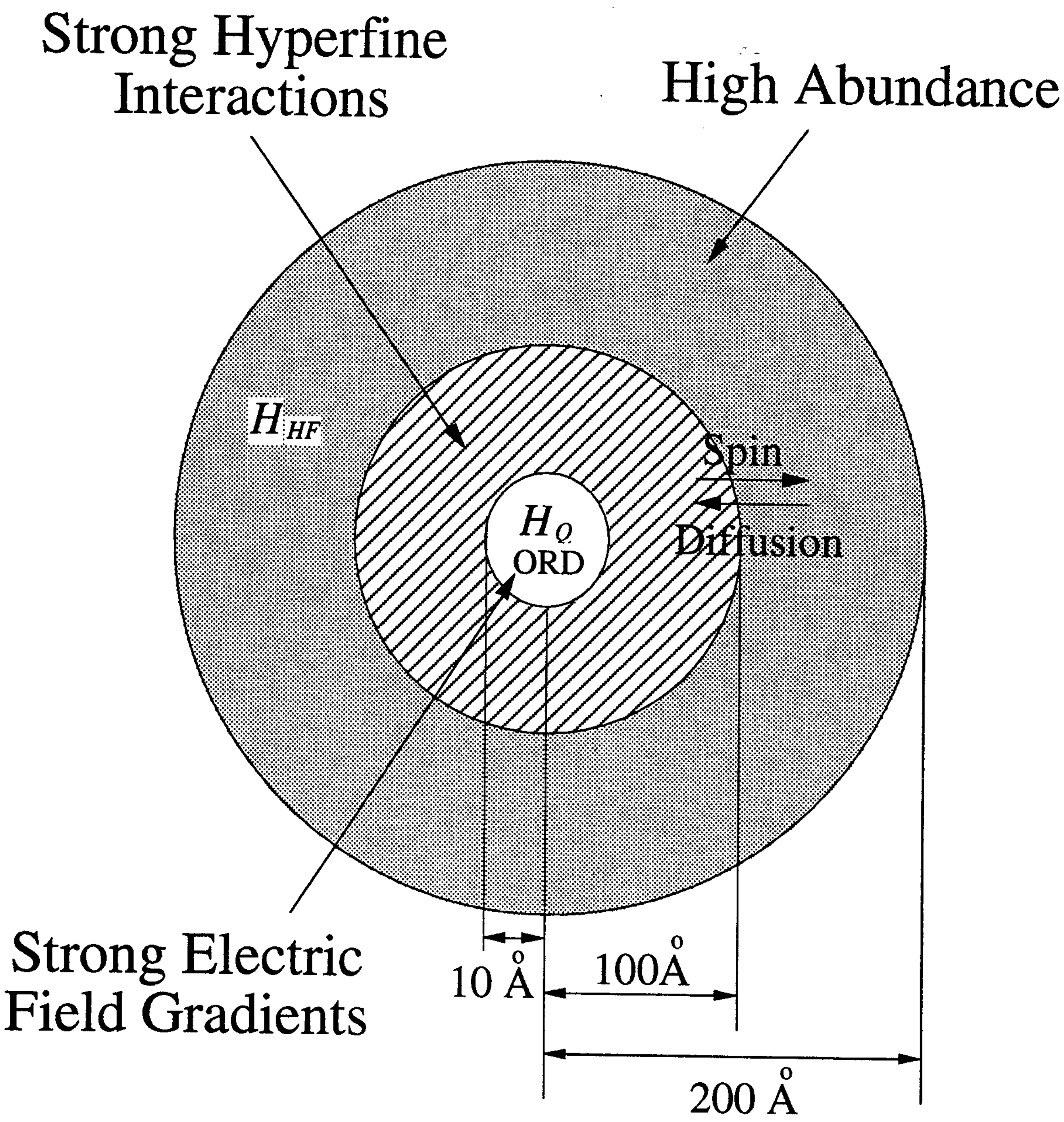

Figure 14. Model of significant interactions for sites around an ORD.

detected. These are rare sites, but the large nuclear polarization allows for their observation. Sites up to 100 Å further away still experience comparable hyperfine interaction, but smaller quadrupole effects so that the satellite transitions are observable, and their distribution is responsible for broadening of the NMR line. Sites distant from the ORD are the most abundant, but are not optically detected and do not possess significant quadrupole interactions. These nuclei remain coupled through spin-diffusion. If sufficient time is allowed for this to occur, the NMR of these sites will be observable by the change in magnetization of sites at the ORD. Based on estimates of the spin-diffusion rate and relaxation times, this region is estimated to encompass sites out to 200 Å away from the ORD at 77 K [7]. The difference between the cw and FT-TSONMR experiment can be explained by taking into account the different timescales and relative spin temperatures of the two experiments. The short duration of the FT experiment (100 μsec) is too rapid for spin diffusion to take place so the NMR spectrum is dominated by sites strongly coupled to the ORD. The duration of the cw experiment (100 msec) allows for spin diffusion to occur so that sites outside the ORD are observable, and because of their large numbers, the NMR spectra should be representative of these sites. Furthermore, the presence of lines shifted away from the bulk resonance is suppressed since the rf frequency which raises their spin temperature leaves the abundant bulk sites cold and thus more capable of recooling them prior to detection. The following discussion will present the background work [7] and will place the more recent experiments into the proper context.

Figure 15 shows a FT-TSONMR spectrum of Sample 5. The extra features around the main resonance result from second order shifts of the central transition of perturbed sites. The central peak has a linewidth of approximately 8 kHz which is twice the intrinsic NMR linewidth. The cw spectrum exhibits unperturbed linewidths, and is slightly shifted from the FT spectrum (fig. 16).

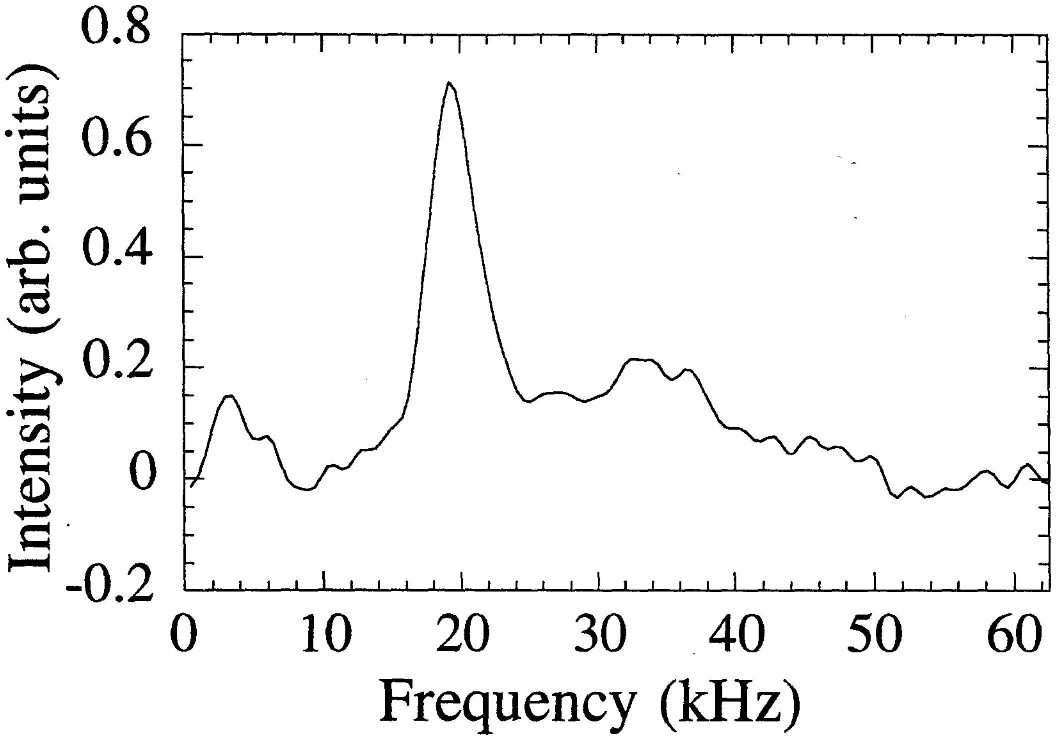

Figure 15. Off resonance FT-TSONMR spectrum of ^{71}Ga in Sample 5 (no quadrature).

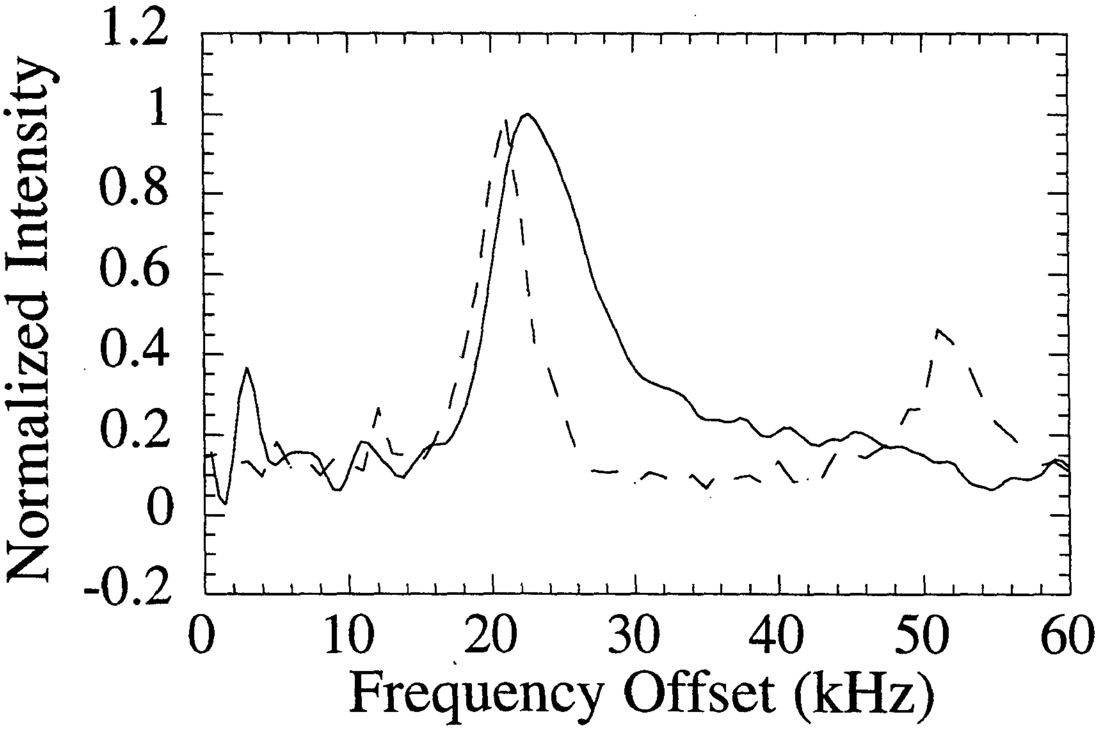

Figure 16. FT and cw spectra from Sample 5 [7]. The cw spectrum exhibits significantly narrower linewidth, and is frequency shifted from the FT-spectrum.

The origin of the broadening in the FT spectrum was investigated with a TSONMR nutation experiment. The results show the presence of an additional peak at $2\omega_1$ (36 kHz), confirming the existence of sites strongly perturbed by the quadrupole interaction with satellites outside the rf bandwidth.

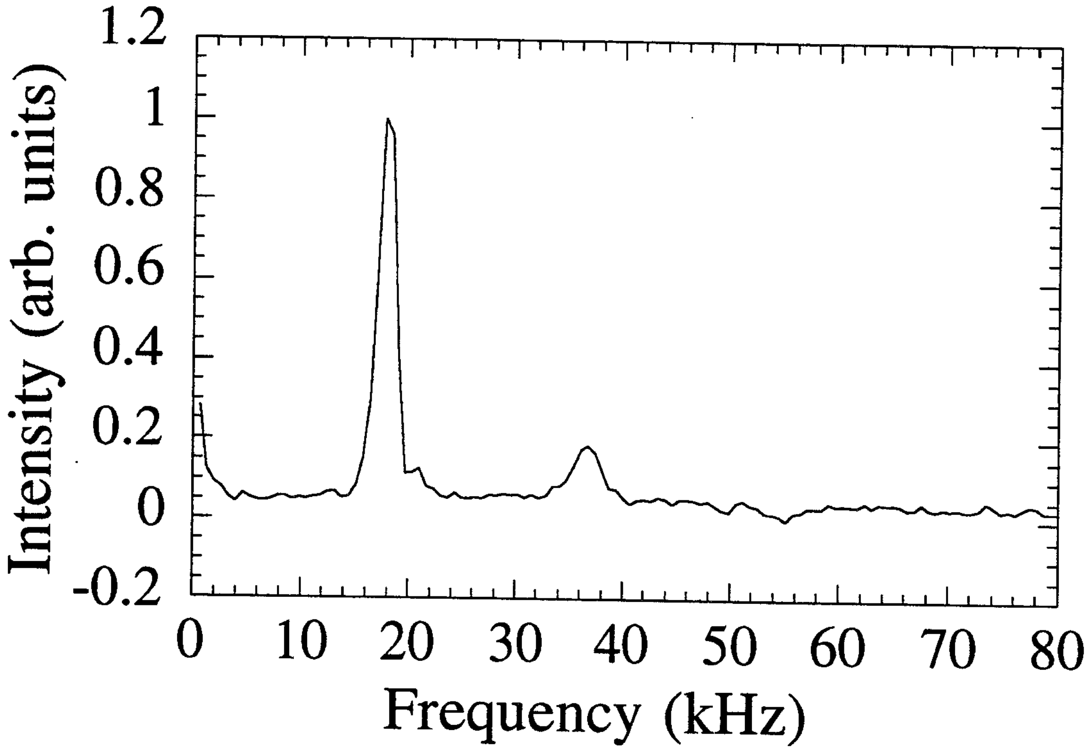

Figure 17. Nutation experiment on Sample 5. The primary nutation frequency is at approximately 18 kHz with an additional peak at 36 kHz corresponding to the sites with quadrupole splittings much greater than the rf bandwidth.

A Hahn spin-echo experiment was performed with the pulse sequence shown in fig. 18. This sequence eliminates the second-order quadrupolar interaction from the NMR spectrum.

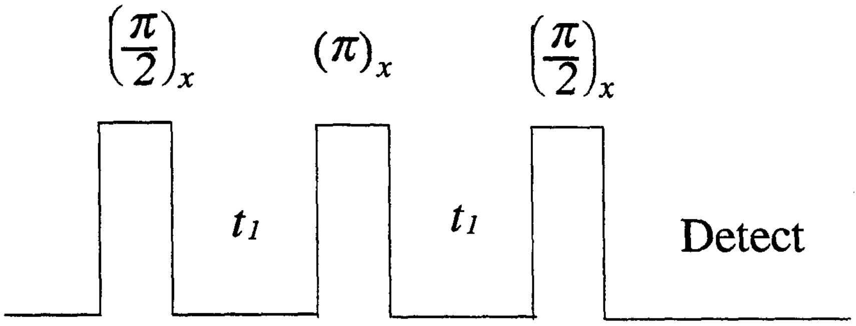

Figure 18. Pulse sequence for the Hahn spin-echo experiment.

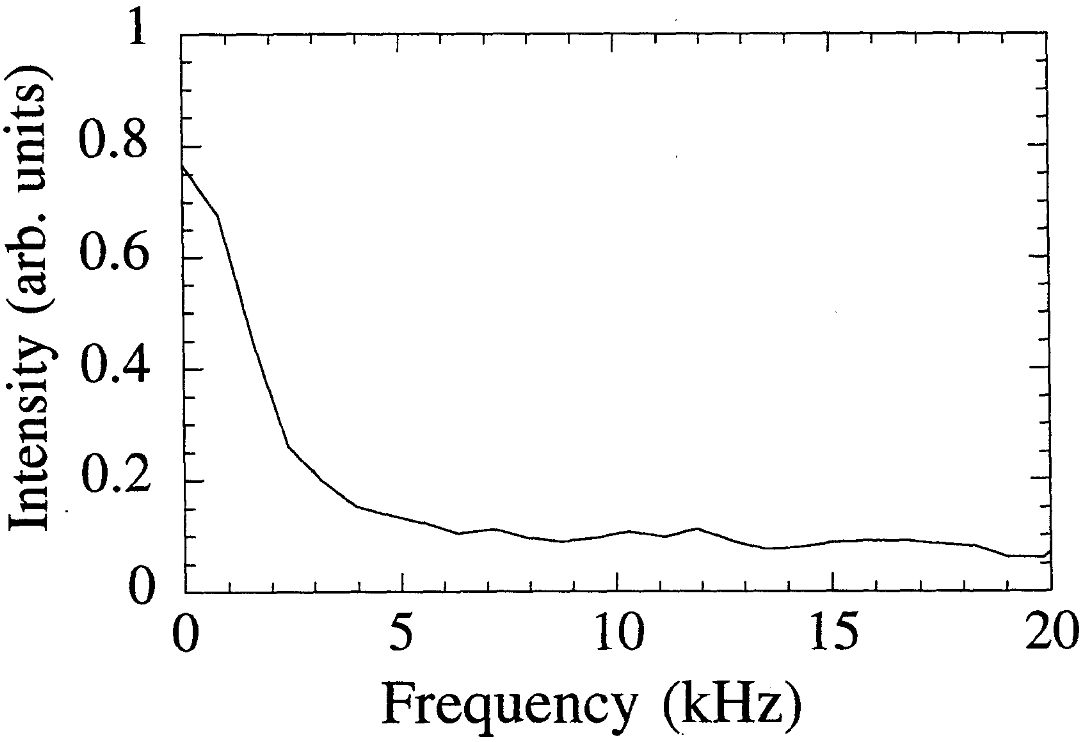

Figure 19. Hahn spin-echo spectrum. The linewidth = 3.6 kHz which is close to the intrinsic linewidth of bulk GaAs.

The spectrum resulting from the Fourier transformation with respect to t_1 is shown in Fig. 19. The broad features have vanished, and the observed linewidth is 3.6 kHz which is close to the unperturbed linewidth.

To explore the role of spin diffusion in the cw experiment, FT experiments were designed to incorporate a period of spin diffusion following NMR. A delay period of 1 second allows for the distant spins to couple to the ORD with spin diffusion. The results show a disappearance of the peak at $2\omega_1$ which supports the picture of the perturbed sites being associated with the ORD and distant sites being unperturbed. The shift in the primary nutation peak, however, is unexplained.

3.7 Recent Investigations

The hypothesis of spin diffusion was adequate for explaining the additional features of the spectrum, but the frequency shift is still a mystery. Additional sets of experiments were performed to explore different hypotheses. The first hypothesis was that the highly polarized nuclei at the ORD create a dipole field which shifts the resonance frequency of spins outside the ORD, which are the spins observed in a cw spectrum. Because of the higher resolution of a cw experiment, an attempt was made to observe the effect of this field by applying a π pulse to the ^{71}Ga before the cw experiment, and a π pulse after the experiment to return the system to the original state for detection. If the dipole field of the highly polarized nuclei is the cause of the shift, inverting these spins should produce a frequency shift in the opposite direction of magnitude comparable to the linewidth. Figure 21 shows the results of the

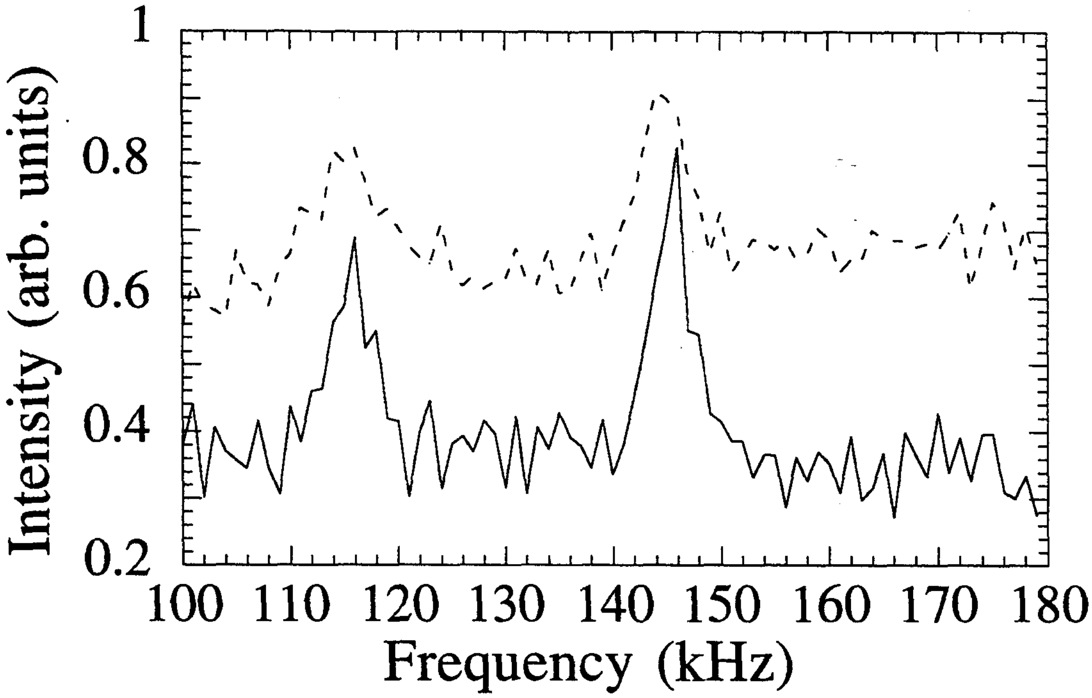

Figure 21. Two cw spectra comparing the effects of π pulses before and after the rf irradiation period to explore the anomalous frequency shift between the cw and FT experiment. The top spectrum is from the experiment with π pulses.

experiments. The data indicates that if a shift is present, it is significantly smaller than the linewidth. If the origin of the shift seen in the FT and cw TSONMR experiments on Sample 5 is due to the dipole field of a highly polarized core, inverting the spins is expected to double the relative shift of the peaks seen in this experiment compared to that of the cw versus FT-TSONMR experiment (fig. 16). While the signal to noise ratio in this experiment is enough to exclude the dipole field model, it does not exclude the possibility of smaller shifts due to other, as yet, unknown mechanisms.

To fully implement multiple-pulse NMR, quadrature phases for the generation of rf pulses is essential. Previous experiments were performed off resonance to avoid confusing signals with positive and negative offset frequencies. The application of spin locking was possible by performing experiments off resonance and tipping magnetization away from the z-axis by an angle equal to the angle of the effective applied field in the rotating frame. By waiting a calculated period of time, the resulting magnetization will eventually become colinear with the effective field. However, there is an associated loss because not all of the magnetization can be spin-locked.

Quadrature was implemented by performing two sets of experiments in which the x and y transverse magnetization are sampled in successive experiments (fig. 22). Figures 23 and 24 are the FT-quadrature spectra for Sample 5 [7] and the p-compensated sample M303 from JPL. Both spectra exhibit comparable linewidths of

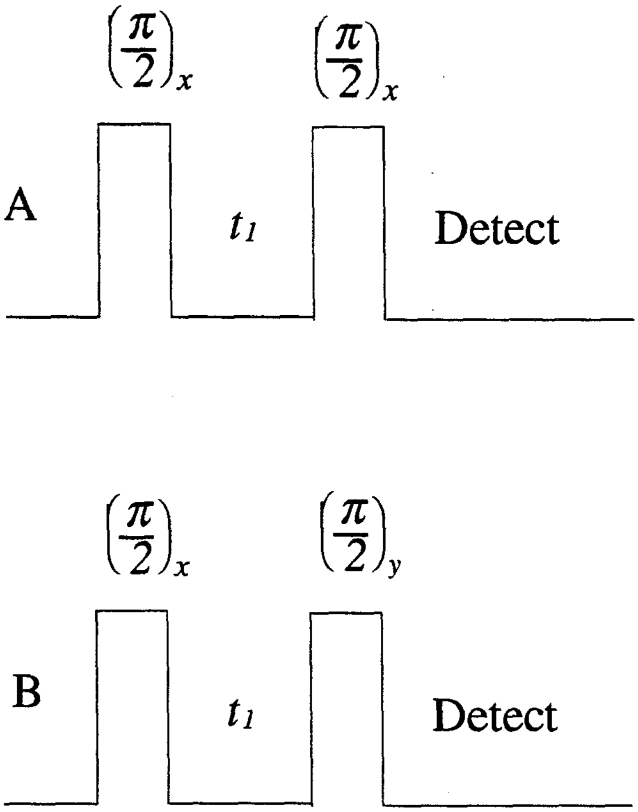

Figure 22. FT-TSONMR sequence for sampling both real and imaginary components.

approximately 8 kHz, but the most interesting feature is the lack of the second order quadrupole shifted lines in figure 23. Previous FT-TSONMR spectra performed off resonance have exhibited additional lines attributed to second order shifts of the central ^{71}Ga resonance (fig. 15). In that experiment, it was not possible to apply an exact $\pi/2$

pulse to the nuclei because of the lack of quadrature rf. With the new hardware, on resonance experiments were performed with π/2 rf pulses applied to the unperturbed ^{71}Ga nuclei (fig. 23, 24). However, the strongly perturbed quadrupolar sites are now nutated by an angle π which would eliminate their contribution to the NMR spectrum (chapter 2).

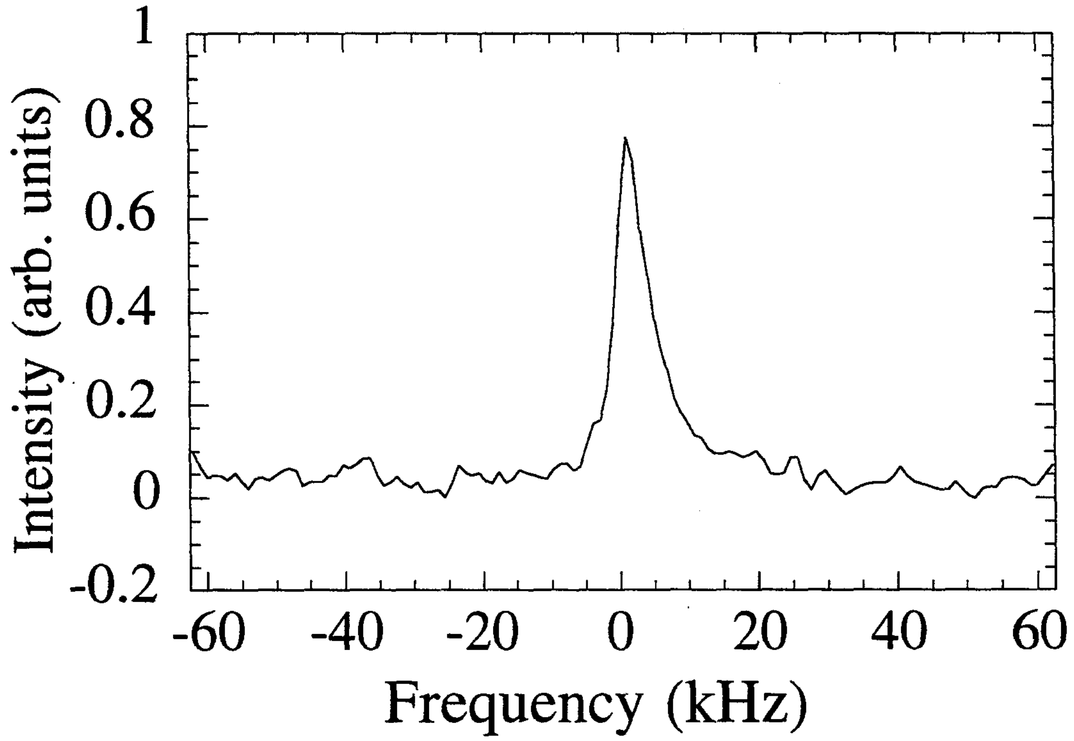

Figure 23. TSONMR experiment on sample 5 with quadrature. Carrier frequency at 151 kHz, π/2 pulse, 8.0 μsec/point, lb = 1300 Hz, 64 data points zero-filled to 128 points. The line width is approximately 7 kHz.

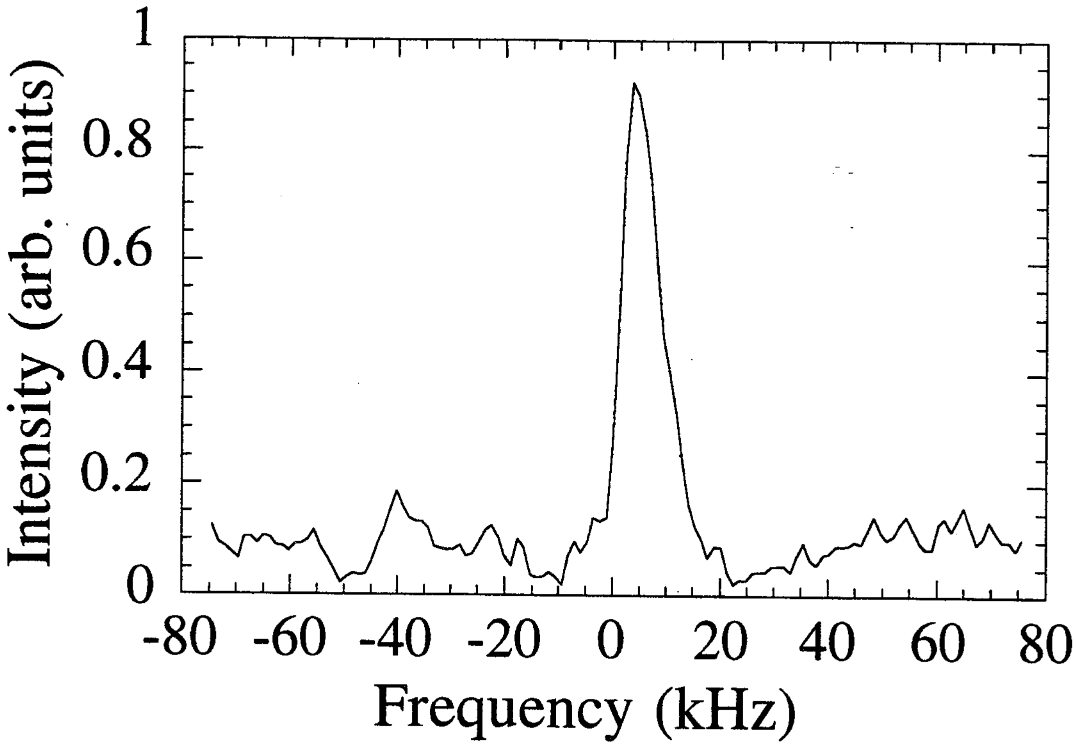

Figure 24. p-compensated GaAs (sample M303). A fit of the lineshape to a Gaussian yields a linewidth of 8.3 kHz.

3.8 Double Resonance Experiments

TSONMR also presents the possibility of studying dilute sites in GaAs with unprecedented sensitivity. To reach the highest possible sensitivity for dilute species, it will be necessary to amplify the destruction of spin order that takes place at resonance. Consider an initial condition of uniform ONP (low uniform Zeeman spin temperature). This can be converted into dipolar order (low uniform dipolar spin temperature) by adiabatically turning off the magnetic field [22] or performing adiabatic demagnetization in the rotating frame (ADRF) [23] on one or more of the principal isotopes. This step stores the spin order in a form common to all the spins in the volume. This is particularly suitable for the detection of the dilute spins associated with defects, since a brief period of resonant irradiation of the defect spins destroys a calculable fraction of the spin order [23]. This destruction may be repeated many times, thereby amplifying the observability of the dilute site resonance. If this repetition is done at intervals of several milliseconds, to allow time for the spin temperature to become homogeneous again before the next pulse, then the magnitude of the destruction remains fully calculable [23]. The fraction destroyed depends, however, on the dipolar spin temperature at the defect site, so there is a diminishing effect of subsequent pulses due to the spin heating by earlier pulses. This is an example of the thermodynamic principle that inverse temperature is the proportionality constant that determines the entropy production associated with a given quantity of heat exchanged. In the present case, the abundant spin reservoir will consist of the ^{75}As, ^{71}Ga, and ^{69}Ga nuclei, which are optically polarizable and detectable as already described. The contact with the dilute species can be made in one of several ways: spin-locking with matched nutation frequencies [24], a common reservoir of dipolar order in zero [22] or high field [23,25], or level-crossing induced by field cycling [26].

The key to the success of these methods is isolation of the spins from the lattice for a period many times longer than that needed for dipolar couplings to transfer spin order between species. The implementation of quadrature phases for TSONMR has facilitated the measurement of the relevant relaxation times $T_{1\rho}$, T_1 during level crossing, T_{1D} (figs. 25 and 26), respectively, and the results are favorable for double resonance measurements.

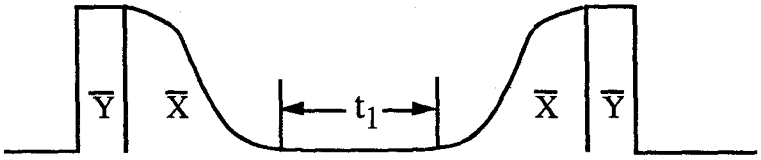

Figure 25. ADRF sequence for measuring T_{1D}.

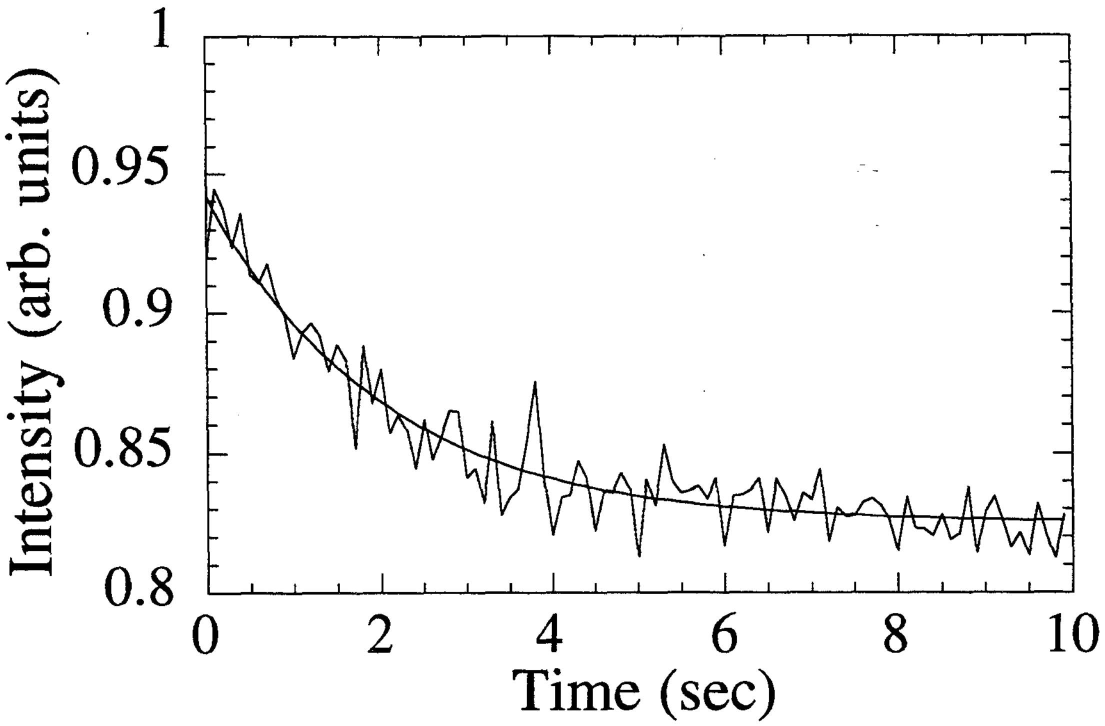

Figure 26. Optical measurement of T_{1D} in GaAs at 77 K. The nuclei are polarized with 6 seconds ONP followed by ADRF. After t_1, the rf is adiabatically turned on and the resulting magnetization is stored along z and measured with field cycling. The measured value for ^{71}Ga is $T_{1D} = 2.0$ sec.

3.9 Discussion

After the implementation of multiple-pulse quadrature NMR, all of the basic NMR experiments were possible, resulting in unprecedented resolution for the ODNMR experiment. All that was left was the demonstration of NMR multiple-pulse line-narrowing in GaAs. This was the key step that would make it possible to probe the probability density of localized electrons in semiconductor nanostructures with TSONMR. With the then current hardware, the 100 Watt amplifier was capable of producing $\pi/2$ times of approximately 15 μsec, but line narrowing sequences require $\pi/2$ times of approximately 2 μsec. Using a 1600 watt rf amplifier to generate the necessary high rf powers led to the discovery of the breakdown of the rotating-wave approximation which made experiments impossible with a linearly polarized rf coil. This approximation becomes invalid when the rf field strength becomes much larger than the Larmor frequency. In this limit, the wavelength of the rf becomes much longer than the pulse length used in the NMR experiment. Each time the rf is triggered, the resulting pulse is a DC pulse with amplitude which depends on the phase of the carrier at that instant so that successive pulses appear to have random amplitudes.

Circularly polarized rf could overcome this problem, but the gains to be obtained by moving to liquid helium far outweighed the added complexity and cost of the experiment. Many signals corresponding to localized sites become broadened and unobservable at higher temperatures. For example, the H-band luminescence in an $Al_xGa_{1-x}As$/GaAs heterojunction to be discussed in chapter 5 becomes unobservable above 10 K [27,28]. In addition, the 150 kHz Larmor frequency available provided poor chemical discrimination. The ^{69}Ga and the ^{27}Al peaks overlapped. These considerations provided the impetus for constructing a new ODNMR spectrometer to be described in the next chapter.

3.10 References

[1] Lampel, G., *Nuclear Dynamic Polarization by Optical Electronic Saturation and Optical Pumping in Semiconductors,* Phys. Rev. Lett., **20**, 491 (1968).

[2] *Optical Orientation*, edited by Meier, F., and Zakharchenya, B.P. (North-Holland, Amsterdam, 1984), Vol. 8.

[3] Flinn, G.P., Harley, R.T., Snelling, M.J., Tropper, A.C., and Kerr, T.M., *Optically detected nuclear magnetic resonance of nuclei within a quantum well,* Semicond. Sci. Technol., **5**, 533 (1990).

[4] Buratto, S.K., Shykind, D.N., and Weitekamp, D.P., *Time-sequenced optical nuclear magnetic resonance of gallium arsenide,* Phys. Rev. B, **44**, 9035 (1991).

[5] Buratto, S.K., Hwang, J.Y., Kurur, N.D., Shykind, D.N., and Weitekamp, D.P., *Fourier-Transform Time-Sequenced Optical Nuclear Magnetic Resonance of Gallium Arsenide,* Bulletin of Magnetic Resonance, **15**, 190 (1993).

[6] D'yakonov, M.I., and Perel', V.I., *Spin Orientation of Electrons Associated with the Interband Absorption of Light in Semiconductors,* Soviet Physics JETP, **33**, 1053 (1971).

[7] Buratto, S.K., *Time-Sequenced Optical Nuclear Magnetic Resonance of Gallium Arsenide*, Thesis, 1993.

[8] D'yakonov, M.I., and Perel', V.I., *Theory of Optical Spin Orientation of Electrons and Nuclei in Semiconductors*, edited by Meier, F., and Zakharchenya, B.P (Elsevier Science, North-Holland, 1984), Vol. 8.

[9] Abragam, A., *Principles of Nuclear Magnetism* (Clarendon Press, Oxford, 1961).

[10] D'yakonov, M.I., and Perel', V.I., *Optical orientation in a system of electrons and lattice nuclei in semiconductors. Theory,* Soviet Physics-JETP, **38**, 177 (1974).

[11] Cohen-Tannoudji, C., Diu, B., and Laloë, F., *Quantum Mechanics* (John Wiley & Sons, New York, 1977).

[12] Paget, D., Lampel, G., Sapoval, B., and Safarov, V.I., *Low Field Electron-Nuclear Spin Coupling in Gallium Arsenide Under Optical Pumping Conditions,* Phys. Rev. B, **15**, 5780 (1977).

[13] Buratto, S.K., Hwang, J.Y., Kurur, N.D., Shykind, D.N., and Weitekamp, D.P., *Time-sequenced optical nuclear magnetic resonance of GaAs,* J. Chem. Phys., to be submitted, (1994).

[14] Berkovits, V.L., Ekimov, A.I., and Safarov, V.I., *Optical orientatation in a system of electrons and lattice nuclei in semiconductors. Experiment,* Sov. Phys.-JETP, **38**, 169 (1974).

[15] Hanle, W., *Über magnetische Beeingflussung der Polarisation der Resonanzfluoreszenz,* Z. Phys., **30**, 93 (1924).

[16] Parsons, R.R., *Band-to-band optical pumping in solids and polarized photoluminescence,* Phys. Rev. Lett., **23**, 1152 (1969).

[17] D'Yakonov, M.I., and Perel', V.I., *Hyperfine Interaction in Optical Orientation of Electrons in Semiconductors,* Soviet Physics JETP, **36**, 995 (1973).

[18] Carson, P., personal communication, 1993.

[19] Werner, M.H., *NMR Imaging of Solids with Multiple Pulse Line Narrowing and Radiofrequency Gradients*, Thesis, 1993.

[20] This sample was provided by J. Liu of the JPL microdevices laboratory in collaboration with F.J. Grunthaner.

[21] PL spectrum obtained by A. Ksendzov of the JPL microdevices laboratory in collaboration with F.J. Grunthaner.

[22] Slusher, R.E., and Hahn, E.L., *Sensitive Detection of Nuclear Quadrupole Interactions in Solids,* Phys. Rev., **166**, 332 (1968).

[23] Lurie, F.M., and Slichter, C.P., *Spin-Temperature in Nuclear Double Resonance,* Phys. Rev., **133**, 1108 (1964).

[24] Hartmann, S.R., and Hahn, E.L., *Nuclear Double Resonance in the Rotating Frame,* Phys. Rev., **128**, 2042 (1962).

[25] Spencer, P.R., Schmid, H.D., and Slichter, C.P., *Sensitivity of Nuclear Magnetic Double Resonance,* Phys. Rev. B, **1**, 2989 (1970).

[26] Edmonds, D.T., Int. Rev. in Phys. Chem., **2**, 103 (1968).

[27] Yuan, Y.R., Pudensi, M.A.A., Vawater, G.A., and Merz, J.L., *New Photoluminescence Effects of Carrier Confinement at an AlGaAs/GaAs Heterojunction Interface,* J. Appl. Phys., **58**, 397 (1985).

[28] Ossau, W., Bangert, E., and Weimann, G., *Radiative Recombination of a 3D-Electron with a 2D-Hole in P-Type GaAs/(GaAl)As Heterojunctions,* Solid State Communications, **64**, 711 (1987).

Chapter 4: The 2 K ODNMR Spectrometer

To implement the multiple-pulse experiments proposed by Buratto *et al.* [1], large rf fields are necessary, comparable to the available DC magnetic field of 115 Gauss in the nonsuperconducting TSONMR apparatus documented in the thesis of S.K. Buratto. At these rf powers, the approximation that linearly polarized rf acts only through one circular component (the "resonant" one) begins to break down. Although this problem can be solved with circularly polarized rf fields, there are other disadvantages of operating at 77 K in addition to low DC magnetic fields that cannot be so easily solved. Many photoluminescence (PL) lines broaden, and become unobservable at 77 K. Performing the ODNMR experiments at 2 K allow a wider variety of samples to be studied. For example, the 830 nm line in a GaAs heterojunction sample, called the H-band, broadens with temperature and becomes unobservable above 10 K [2,3]. The ONP process is also strongly temperature dependent. The significantly longer nuclear relaxation times at 2 K allows the creation of large nuclear polarizations (10%) [4]. The drawback is the increased complexity and cost of the cryostat design. The low heat of vaporization and the high cost of liquid helium make the optimization of the cryostat design essential. This chapter describes the design of the cryogenic NMR probe and liquid helium optical cryostat along with the detection apparatus.

4.1 The Liquid Helium Optical Cryostat

The original goal of the cryostat design was to be able to perform TSONMR experiments at liquid helium temperature with magnetic field cycling. The construction material of choice was glass, in order to eliminate eddy currents created by the necessarily large changing magnetic fields. To perform optical experiments in liquid helium, it is necessary to cool it below the λ-point (2.17 K). This is the temperature at which ^{4}He becomes a superfluid. Above this temperature, the boiling liquid helium scatters the laser light, making optical experiments impossible. Since the temperature of the helium is determined by the pressure above the liquid, it can be lowered by pumping off the evaporating gas. Large orifices are used to minimize the size of the mechanical pump needed, the most costly piece of equipment. The glass optical cryostat, made by Pope Scientific, has 4 walls made of borosilicate glass, each with a thickness of 0.23 cm, and has a volume of approximately 10 liters (figure 1). The inner two glass walls define the helium dewar space followed by the liquid nitrogen jacket and enclosed by the outer two glass walls. Without this lN_2 shield, the blackbody radiation from room temperature would reduce the helium hold time from 8 hours to 15 minutes for 5 liters of helium. The top of the cryostat, shown in figure 1, is constructed of copper with a large orifice at the side for connecting the pumping apparatus.

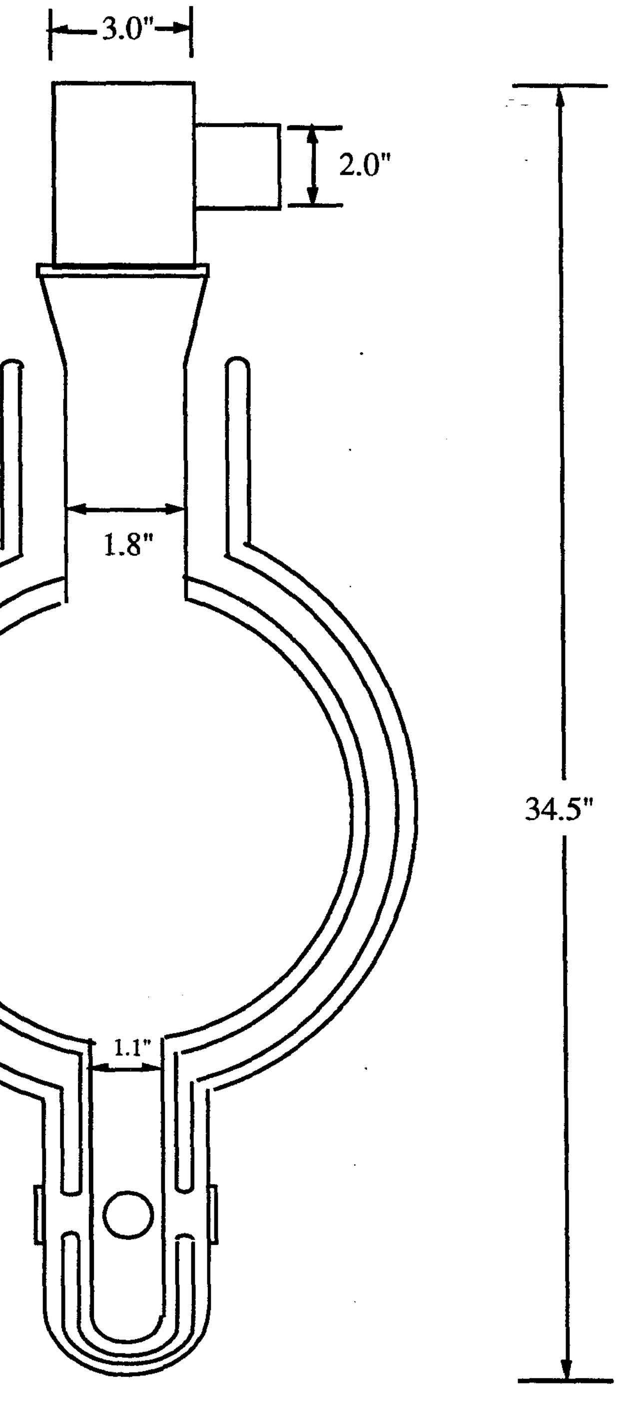

Figure 1. The Pope helium dewar is a four-walled glass dewar. The inner chamber is for helium, and the outer layer contains a nitrogen jacket.

4.2 The Helium Pumping System

To cool the helium down to the λ-point, the pressure must be reduced by pumping off the evaporating gas. At a helium pressure of 38 mm Hg, the temperature is uniquely determined to be 2.17 K. There will be a significant loss of helium in the cooling process because the large enthalpy of the liquid helium needs to be carried off by the pumped gas [6], which has a low heat of vaporization. Table 1 lists the fraction of helium remaining after reaching a given final temperature, assuming the process is carried out slowly.

Final Temp (K)	Fraction Remaining
3.5	0.83
3.0	0.74
2.5	0.68
2.0	0.63
1.6	0.58

Table 1. Liquid helium remaining after pumping to various final temperatures [5].

To maintain a constant temperature, the helium must be pumped at a rate equivalent to its boil off rate. The original transport calculations used a boil off rate of 1 liter/hour to calculate the flow rate to be carried by the pipes connecting the cryostat to the pump. Experimentally, it is 0.6 liters/hour. The pump is located 30 feet from the dewar in another room because of the excessive noise and the oil vapor given off from pumping helium gas at 38 mm Hg. Over these distances, the pressure drop is minimized to avoid the need for an excessively large vacuum pump. These calculations will be reviewed using the actual boil off rate.

The estimate of the pumping rate needed assumes negligible pressure change in going from the interior of the dewar to the dewar pump orifice. Isothermal flow at room temperature is assumed through the 30 foot section. If the dewar has been designed properly, these assumptions should be valid. If there is ice on the pumping line, this means liquid helium is being wasted because the pump rate is too high. Assuming a pressure of 38 mm Hg at 293 K and a boil off rate of 0.6 liters/hour, the resulting volumetric flow rate is 180 liters/minute. The pipe diameter is equal to the dewar orifice size of 1.5" to minimize the pressure drop. Useful quantities are given in tables 2 and 3.

ΔH_{vap}	3.5 J/cm^3
Density (2.17 K)	0.145 g/cm^3
Pressure	38 mm Hg
Temperature	2.17 K

Table 2. Physical properties of liquid helium at the λ-point [5].

Total Volume He	5 liters
Total Weight He	0.725 kg
ΔH_{vap} He (5 liters)	17500 J
Heat Transfer Rate	0.6 Watts

Table 3. Storage characteristics of the liquid helium dewar.

The type of flow through the pipe is characterized by the Reynolds number (Re) which determines the relative contributions of the viscous and kinetic forces which governs fluid flow

$$Re = \frac{DV\rho}{\mu} \qquad (1)$$

where D is the characteristic pipe diameter, V the characteristic velocity, ρ the gas density, and μ the gas viscosity. The viscosity of helium gas at 38 mm Hg pressure at room temperature is estimated with the Chapman-Enskog equation [6] which is based on the Lennard-Jones (6-12) potential. This equation provides accurate values for the viscosity of dilute gases at room temperature. The interatomic potential

$$\phi(r) = 4\varepsilon\left[\left(\frac{\sigma}{r}\right)^{12} - \left(\frac{\sigma}{r}\right)^{6}\right] \tag{2}$$

leads to viscosity μ, where

$$\mu = 2.669 \times 10^{-5}\frac{\sqrt{MT}}{\sigma^2 \Omega_\mu} \tag{3}$$

$$\Omega_\mu = 0.7,$$

$$\sigma = 2.576\ \text{Å},$$

$$T = 293\ \text{K},$$

$$M = 4\ \text{g/mole}$$

In these equations, σ is the characteristic diameter of the helium atom used in the Lennard-Jones potential and M is the molecular weight. Ω_μ is a slowly varying function of the dimensionless temperature kT/ε [6] where ε is the energy of interaction between the atoms. From this relation, $\mu = 2 \times 10^{-4}$ g/cm-sec.

Reynolds Number Parameters	Values
V	256 cm/sec
ρ (density)	8.3×10^{-6} g/cm^3
D	3.8 cm
μ	2.0×10^{-4} g/cm-sec

Table 4. Reynolds number parameters.

Using the values in table 4, $Re = 40$. For flow in smooth pipes, $Re < 2100$ results in laminar flow. In this regime, the pressure drop can be calculated with the Hagen-Poiseuille equation for laminar flow in tubes

$$\Delta P = \frac{8\mu LQ}{\pi R^4} \tag{4}$$

The calculated pressure drop of 0.04 mm Hg is insignificant compared to 38 mm Hg, so the assumptions of constant density for the flow through the pipe and negligible pressure drop for flow through the dewar are valid. If the flow were compressible, the equations would have had to be integrated over differential sections. With an estimated flow rate of 180 liters/min, a Welch 1397 with 17.7 CFM, or 500 liters/minute, capacity was used. Experimentally, only a fraction of the pump capacity is needed.

4.3 Heat Transfer

When constructing the NMR probe, care must be taken to minimize the heat flux into the helium dewar. Milliwatts are significant when constructing a helium dewar. For example, a 30 mW heat leak would result in a boil off of approximately 1 liter/day. This quantity is comparable to the energy flux from the laser beam. The most significant heat leak is the blackbody radiation into the dewar from the optical windows, followed by conduction through the glass dewar and wires connecting the cryogenic probe to the external environment.

4.3.1 Black Body Radiation

The energy flux from blackbody radiation is described by the Stefan-Boltzman law

$$q = \sigma T^4 \tag{5}$$

where $\sigma = 1.355 \times 10^{-12}$ cal/sec-cm^2-K^4 and T is expressed in units of K. Since the optical windows are transparent to the near infrared and visible radiation, the primary components of the thermal radiation at 293 K, the inner window is is assumed to transmit all of the incident radiation.

The inner window is 0.75" in diameter, and the outer window is 1.25" separated by a 1.5" gap. There are three sets of these inner/outer window pairs. To simplify calculations, the energy flux from the room through the inner window is modeled as if the outer window were an infinite plane. This is because the outer window is four times larger than the inner window. Using equation 5, the total heat flux for all three windows is 340 mW which corresponds to half of the heat flux into the dewar. When a radiation shield at 77 K is present, the heat transfer by radiation is drastically reduced. The heat leak from blackbody radiation between the liquid nitrogen jacket at 77 K and the inner helium dewar, over an area of approximately 2000 cm^2, is only 30 mW. The next largest contribution to the heat leak is due to the conduction of heat through solid construction materials.

4.3.2 Heat Conduction Through Solids

The analytic calculation of thermal conduction from 2.17 K to 293 K is difficult because the thermal conductivity is a complex function of temperature. Cryogenic designers have long used the concept of thermal boundary potential [7]. The heat conduction through a material is described by the product of the thermal conductivity κ and the temperature gradient

$$\dot{Q} = -A(x)\kappa(T)\frac{dT}{dx} \tag{6}$$

where A is the area of heat flow and $\dot{Q}$ is the heat flux. Integrating this equation, we get

$$\int_{x_1}^{x_2} \frac{\dot{Q}}{A(x)}dx = -\int_{T_1}^{T_2} \kappa(T)dT \tag{7}$$

At steady state, $\dot{Q}$ is constant along x so the integral of κ can be split up to obtain

$$\dot{Q} = \frac{-\int_0^{T_2} \kappa(T)dT + \int_0^{T_1} \kappa(T)dT}{\int_{x_1}^{x_2} \frac{1}{A(x)}dx} \tag{8}$$

The quantity $\theta_i = \int_0^{T_i} \kappa(T)dT$ is the thermal boundary potential, and is tabulated for common materials [5]. The quantity in the denominator is called the geometric factor.

For the conduction along wires, the area $A(x)$ is constant along x so it may be taken out of the integral. Table 7 is a list of the calculated heat leak from wires connecting the helium chamber to the outside.

Wire	Heat Leak
two 28-gauge copper rf wires	20 mW
two 16-gauge brass wires	120 mW
24-gauge stainless steel coax	6 mW

Table 5. Approximate contribution of wires to helium boil off rate.

The selection of the material used for the magnet leads is difficult because of the strong temperature dependence of the heat and electrical conductivity. For the magnet leads, an optimized design was obtained with some trial and error. Originally, 16-gauge brass wires were selected over copper because copper has an extremely large thermal conductivity at 4 K. The heat conduction from 16-gauge copper wires would result in a boil off rate of 1.2 liter/hour which is twice as large as what is observed. However, the higher resistivity of brass results in a larger amount of Joule heating. 2-16-gauge brass magnet leads carrying 15 Amps of current generated enough resistive heating to boil off approximately 0.14 l/hour more helium compared to the current magnet lead design. In this design, 6 inches of 13-gauge copper wire, which has a much higher electrical conductivity, was used in the neck region of the dewar. To eliminate Joule heating inside while also minimizing heat leaks due to conduction, a superconducting wire was strung along a brass wire with multiple solder joints connecting the two along their entire length. When the wire pair is submerged in liquid helium, all of the current is shunted through the superconducting wire. Above the helium level, when the wire is not superconducting, all of the current flows through the brass wire.

For design purposes, all of the conduction calculations are performed with a liquid helium level at the middle of the spherical dewar of radius 10". At the middle of the helium dewar, the temperature is 2.17 K and at the top of the helium space, the temperature is 77 K. $A(x)$ is the conducting area in the glass dewar as a function of x, the height relative to the middle of the dewar. The orifice at the top of the helium space has a diameter of 1.9". This neck is in contact with liquid nitrogen at 77 K. A comparision of the heat loss from the dewar used in the experiments and one which has a vacuum insulated neck with a 77K blackbody radiation shield will be made. The geometric factor

$$\int_{x_1}^{x_2} \frac{1}{A(x)} dx \tag{9}$$

can be evaluated analytically to give the following result

$$\int_{x_1}^{x_2} \frac{1}{A(x)} dx = \frac{1}{2\pi t} \sin^{-1}\left(\frac{x}{R_a}\right) + \frac{l}{2\pi R_b t}$$

(10)

where t is the thickness of the glass, x is the height above the helium level ($x = 0"$) to the neck region ($x = 4.9"$), R_a is the radius of the liquid helium chamber, R_b is the radius of the neck, and l is the length of the neck region which is surrounded by both a vacuum space and a liquid nitrogen jacket. The first term is associated with the spherical region surrounding the helium chamber and the second term is associated with the neck region. It is clear that a dewar with an insulated neck is much better. In these calculations, a 12" insulated neck will be used as an example.

Conduction through the glass	$\dot{Q}$ (mW)
$l = 0"$	133
$l = 12"$	13

Table 6. A comparision between a dewar with a vacuum insulated neck and a single walled neck, cooled to 77 K by a liquid nitrogen jacket.

When all of the heat leaks are added up, the total calculated heat flux of 649 mW is close to the observed value.

Source	$\dot{Q}$ (mW)
Blackbody radiation (windows)	340
Blackbody radiation (dewar)	30
Conduction (dewar)	133
Conduction (wires)	146
Total	649

Table 7. Tabulation of heat leaks in the helium cryostat.

If a similar dewar with an insulated neck has only one window, the heat leak would be approximately 300 mW. This translates into a hold time for the helium of nearly 18 hours instead of 8 hours.

4.4 The Probe Construction

The design of cryogenic equipment places stringent demands on the mechanical properties of materials. The large temperature range over which the parts are to be used results in large thermal stresses which can result in mechanical failure, compounded by the fact that many materials are brittle at 4.2 K. The construction material must also minimize heat losses by conduction. Since magnetic fields are present, the material must be nonmagnetic. G-10, a brand of fiberglass, is favored by cryogenic equipment manufacturers. The parts are assembled with "Shygoo" (Table 5), named after its creator David Shykind, because the thermal stresses in normal epoxy at liquid helium temperature will lead to mechanical failure. Finely ground quartz chop is added to the epoxy in "Shygoo" to reduce the average thermal expansion coefficient of the mixture.

"Shygoo" recipe
1 part CIBA 6010 resin
1 part CIBA 825 hardener
1 part fine quartz chop

Table 8. "Shygoo" recipe. To use, mix the ingredients, apply, and wait 8 hours for the mixture to harden.

Material	Thermal Expansion Coeff
Plexiglass	11
G-10 tube (axial)	2.3
G-10 tube (radial)	2.8
quartz	-0.08
Teflon	21
aluminum	4.1
Pyrex	3 to 4
copper	3.3

Table 9. Thermal expansion coefficients for common materials [8].

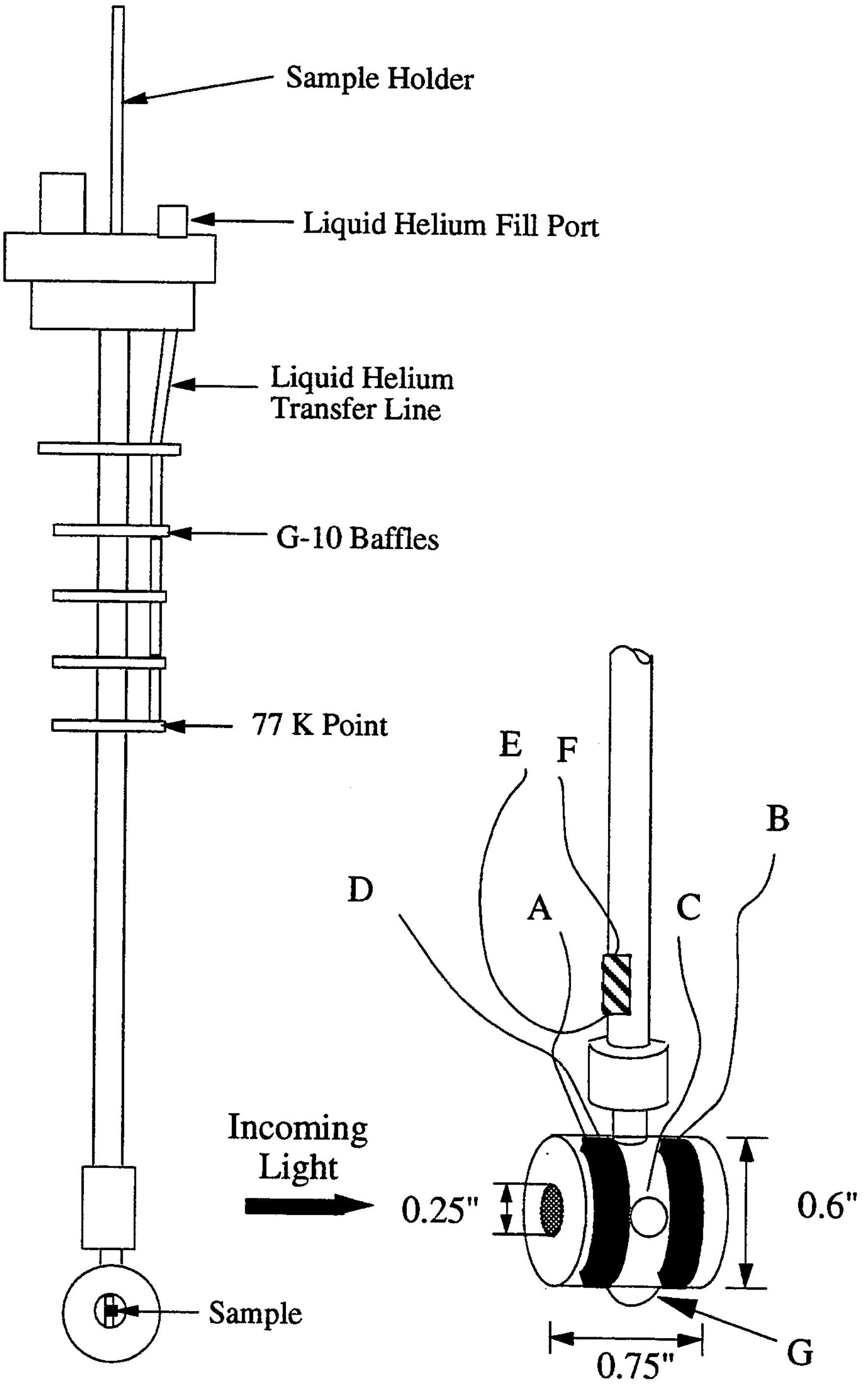

Figure 2. Close-up of superconducting magnet mounted onto the NMR probe. The leads are for superconducting magnets (A,B), rf coil (C,D), carbon resistor leads (E,F), and connection between superconducting magnets (G).

Without this, the thermal stresses from the daily 300 K thermal cycle will lead to mechanical failure. Table 6 is a list of thermal expansion coefficients for several common materials. The schematic of the NMR probe is shown in figure 2. Heat transfer by convection from the helium chamber to the neck region at 77 K is minimized by placing G-10 disks or "baffles," from the point where the dewar temperature is 77 K, up the neck of the dewar [5]. However, these baffles must be bypassed with a tube to allow the transfer the liquid helium into the main chamber of the dewar. It is not possible to fill the dewar by forcing liquid helium down the sides of the neck of the dewar because the neck temperature is too high. The sample is attached to a 3/16" G-10 rod, leading from the magnet to the top of the dewar, with GE 7031 varnish. The rod leads from the magnet to the top of the dewar. The rf coils are oriented so that the rf field is horizontal and transverse to the Zeeman field.

4.4.1 Dewar Cap Design

The NMR probe with superconducting magnet requires several wires to be inserted into the evacuated dewar. The connections are made with vacuum feed-throughs consisting of threaded G-10 plugs with a hole drilled through the center for the wire. The wires are coated with "Shygoo" before inserting them into the plug. The threaded plug is then coated with GE 7031 varnish and screwed into the dewar cap. Figure 3 shows the layout for the various feedthroughs.

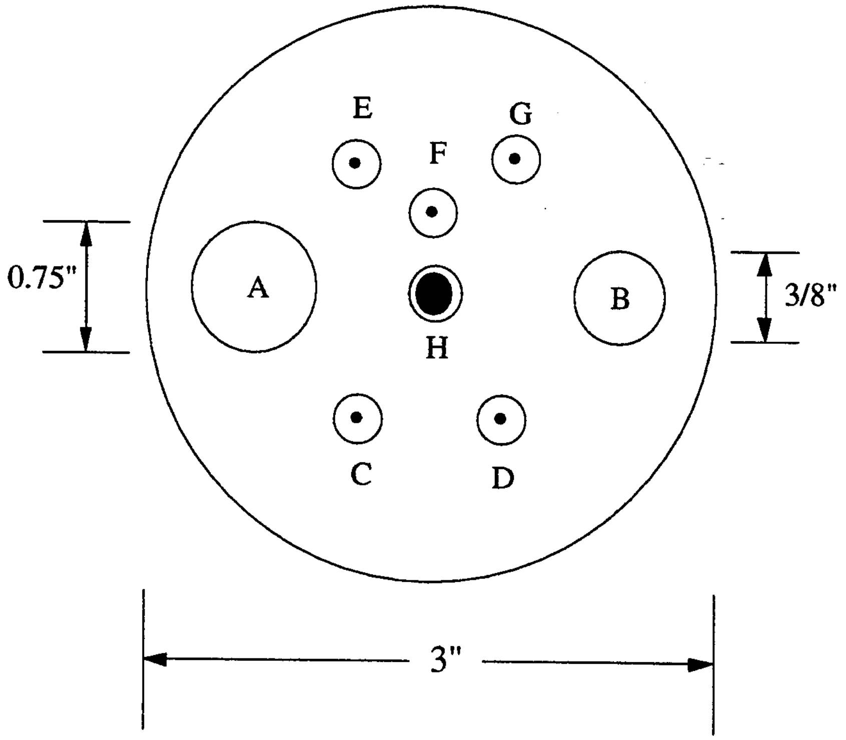

Figure 3. Schematic of dewar cap layout. (A) Exit port for helium exhaust, (B) helium fill port, feed throughs for: (C,D) superconducting magnet leads, (E,F) leads to the carbon resistor, (G) rf coaxial cable, (H) 3/16" sample holder.

4.4.2 Temperature Measurement

The temperature in the dewar was monitored with a carbon resistor located a few inches above the superconducting magnet. Table 8 shows the measurement of the resistance versus temperature. The temperature at 500 ohms marks the onset of superconductivity in the magnet wire.

R (ohm)	T (K)	Est. Error in T	Calculated T (K)
260	293	5	271
330	77	3	92
500	10	2	33
4300	4.2	0.01	4.3
28500	2.17	0.01	2.03
33000	-	-	1.94

Table 10. Experimental values of the resistance as a function of temperature.

The functional dependence of the carbon resistor may be approximated by

$$T = \frac{\ln(R)}{\left(a + b\ln(R)\right)^2} \tag{11}$$

A least squares fit has been performed with the results $a = -2.35$ and $b = 0.448$. The data and the fit are plotted in figure 4.

Although there is some error in fitting the resistance versus the temperature, it is qualitatively correct. The main purpose of this fit was to estimate the temperature during an experiment, when the resistance is typically at 33 kΩ. The estimated errors at 4.2 and 2.17 K are artificially reduced so that the scale is fixed at this temperature for extrapolation purposes. However, based on the phase transition, the λ-point transition is the most accurate temperature point in the list. Using the fit, the estimated temperature corresponding to R = 33 kΩ is 1.94 K so that the helium temperature is still very close to the λ-point.

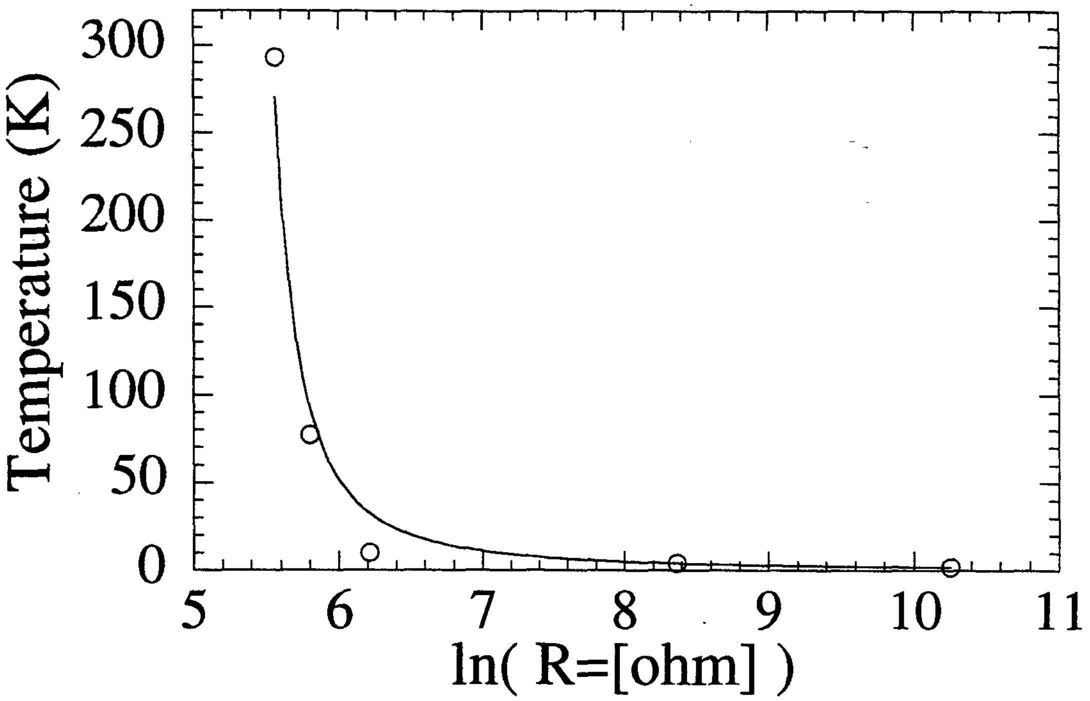

Figure 4. Experimental temperature and resistance of a 260 ohm carbon resistor and the fit to equation (11).

4.4.3 The Superconducting Z-Field Magnet

To obtain the desired magnetic fields, superconducting technology was used [9]. The design consideration of the Zeeman superconducting magnet was to maximize magnetic field within the space constraints shown in figure 5 which was achieved by maximizing the number of wire turns in the magnet. Figure 6 is a simulation of the magnetic field inside the Zeeman coil used. The bore of the magnet was 0.25" wide and 0.8" long. This provides a total angle of 30° for the collection of photoluminescence.

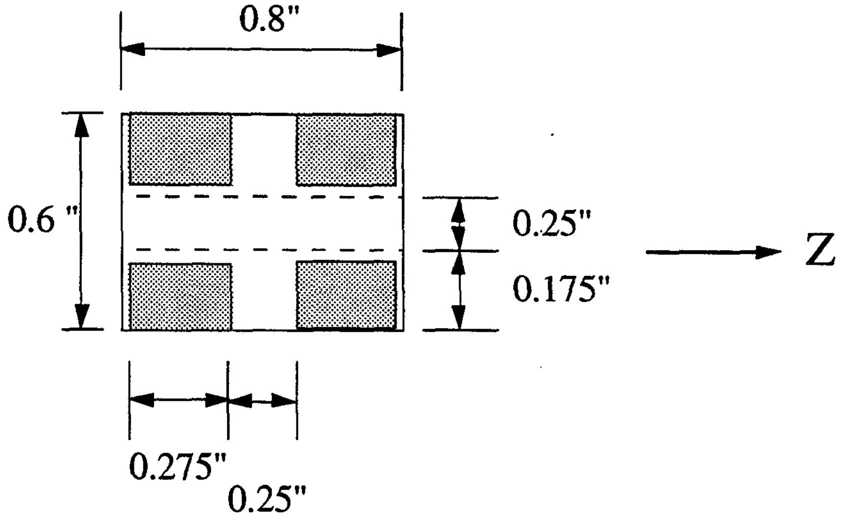

Figure 5. Dimensions of the Zeeman magnet.

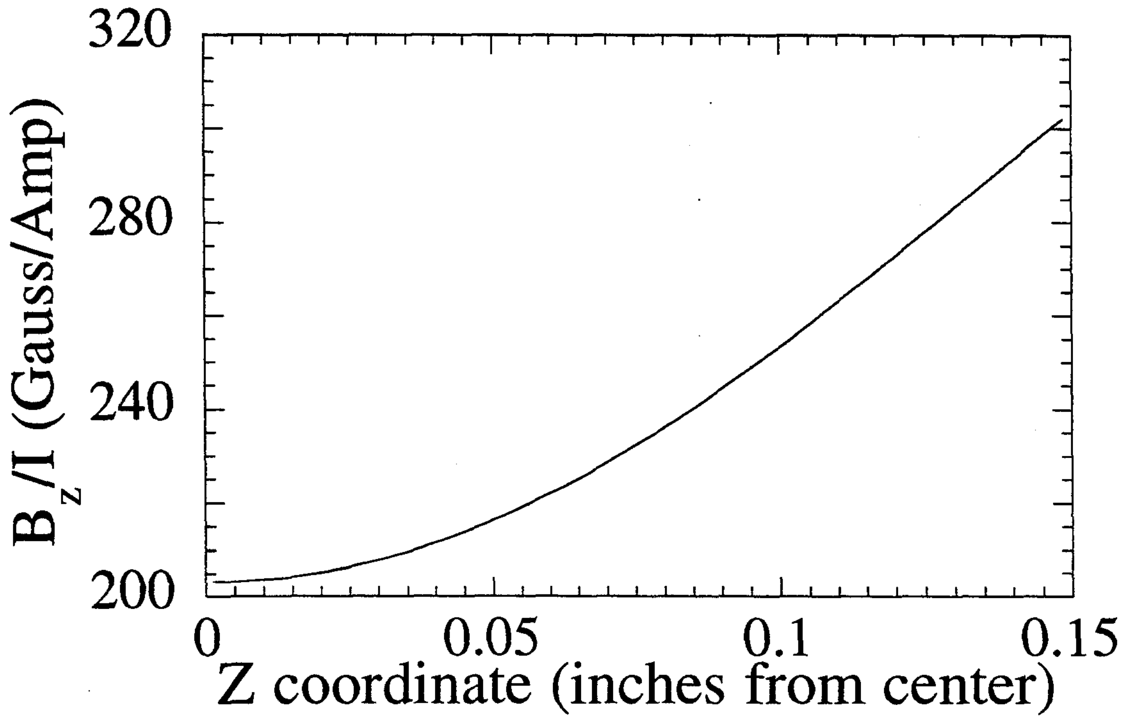

Figure 6. Simulated longitudinal magnetic field along the coil axis. The value of 206 Gauss/amp at the center is experimentally obtained.

4.4.4 The Radiofrequency Field

The design goal for the rf coils was to maximize the rf field for the given power available. Since experiments are performed in fields of ~ 200 mT, the Larmor frequencies for the principal isotopes of GaAs are in the 2 to 3 MHz range. Normally, 100 watt rf amplifiers are sufficient to achieve the required pulse times of 2 to 3 μsec necessary for multiple-pulse experiments. This is because the probes in high field NMR are resonant circuits with quality factors of $Q = 100$. The quality factor is associated with a ringdown time of approximately πQ oscillations. At 200 MHz, this corresponds to a ringdown time of approximately 0.5 μsec, but at 3 MHz the ringdown time is 30 μsec which makes multiple pulse experiments with a tuned circuit impossible. Optimizing the rf magnetic field without a tuned circuit places greater demands on the rf coil design in addition to requiring a larger rf amplifier. An ENI rf amplifier, model A-500, is used with a maximum of 500 watts of rf output power into 50 ohms, resulting in currents which produce a 140 gauss magnetic field. The final design of the rf coil used in the experiment consists of a pair of 3 by 3 arrays of nine turns each of 36 guage wire wound about a hollow G-10 rod 0.25" in diameter. The coil pair separation was 3.6 mm. The resulting magnetic field was simulated with the program MANYCOIL.C written by John Marohn which calculates the field by summing the field contributions of discrete elements using the Biot-Savart law. Experimentally, the frequency response of the coil is flat over the range of interest, resulting in a $\pi/2$ time of 3 μsec for ^{71}Ga, and 5 μsec for ^{75}As. The different pulse times result from the different gyromagnetic ratios of the two nuclei.

Normally, NMR probes are impedance matched at 50 ohms to maximize the amount of power transferred. By not tuning the probe, the rf coil cannot be matched, but experiments have shown that running the ENI amplifier in this way generates larger rf magnetic fields than when a 50 ohm resistor is placed in series.

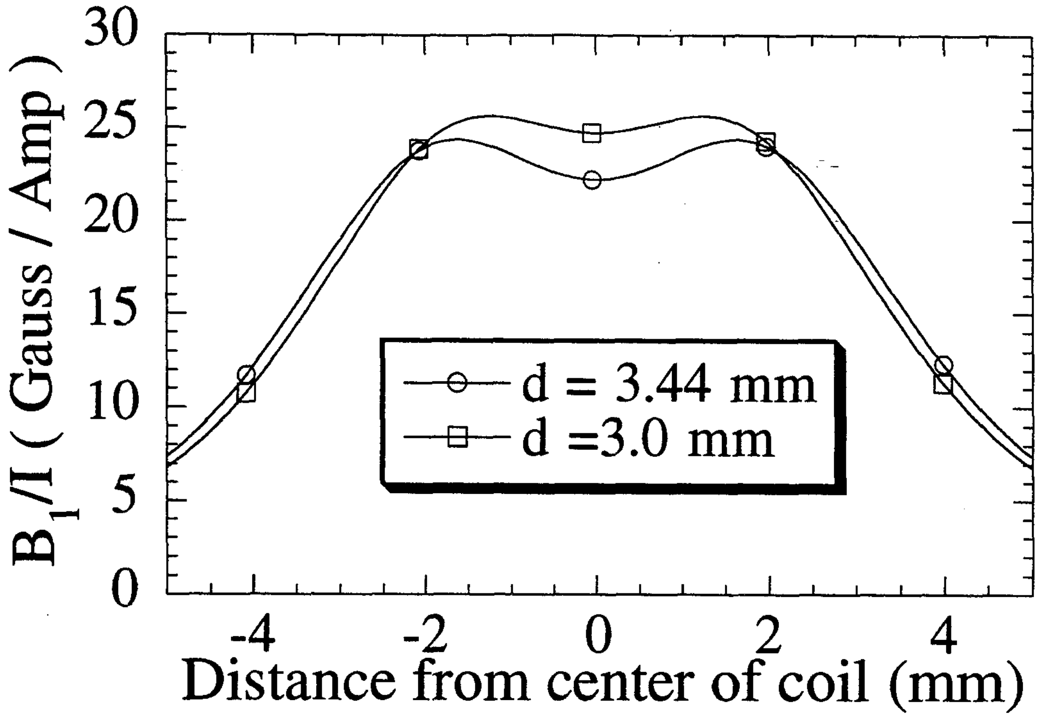

Figure 7. Simulation of rf field strength. The coil pair separations simulated are d = 3.0 mm and 3.44 mm. The actual coil separation used was 3.6 mm. The radius of the coil is 0.25". There are 9 turns of 36 guage wire on each side.

4.4.5 The Photodiode

The photodiode used in the experiment is a low noise silicon avalanche photodiode (EG&G, model C30998-30) with a built-in preamplifier optimized for detection of 400 to 1000 nm radiation with a 30 MHz bandwidth. Table 9 lists the important specifications for this diode. Noise measurements with lock-in detection were

Bias Voltage	-234 V
Dark N.E.P.	0.018 $pW/\sqrt{Hz}$
Responsivity	11.5 MV/W
Bandwidth	27.3 MHz

Table 11. Detector specifications.

made with the laser light on yielding noise of 0.13 $\mathrm{pW}/\sqrt{\mathrm{Hz}}$. Compared to the quantum-limted noise of 0.027 $\mathrm{pW}/\sqrt{\mathrm{Hz}}$, this is a factor of 5 above shot noise. The detector noise equivalent power (NEP) indicates that the detector should be capable of shot-noise limited detection. The discrepancy is attributed to noise in the laser output.

4.5. Excitation and Detection of Real-Time Optically Detected NMR

The optical pumping is accomplished with the same setup as described in chapter 3. The demodulation of the optically detected NMR beat frequencies (chapter 5) was achieved with a home-built heterodyne spectrometer. Figure 8 is a schematic of the ODNMR apparatus, and figure 9 is a schematic of the heterodyne spectrometer. In this experiment, only the difference $I_+ - I_-$, and not the sum, is detected because the NMR information is encoded in this quantity. The PEM in conjunction with a linear polarizer acts as a mixer to modulate an input signal, having frequency ω_{diff}, to give an output frequency of

$$\omega = \omega_{\mathrm{diff}} \pm 50 \text{ kHz} \tag{12}$$

where ω_{diff}, the difference in precession frequencies of two isotopes. Note that the action of the PEM and the polarizer is to modulate I_+ and I_- 180° out of phase from each other at 50 kHz. This signal is converted into current by the photodiode and used as the input to the heterodyne spectrometer. A reference signal is generated by mixing a 30 MHz reference signal from the spectrometer and a sinusoid at $\omega_{\mathrm{diff}} - \Delta$, where Δ represents an audio offset, from the D/A waveform generator used to generate the rf pulses (Signatec, AWG502). The resulting signal is sent through a 30 MHz low pass filter to yield the frequency

$$\omega_{\mathrm{a}} = 30 \text{ MHz} - \omega_{\mathrm{diff}} + \Delta \tag{13}$$

This signal is combined with the 50 kHz reference output of the PEM (whose square wave is first filtered to give a sine wave) to yield

$$\omega_{\mathrm{ref}} = 30 \text{ MHz} - \omega_{\mathrm{diff}} \pm 50 \text{ kHz} + \Delta \tag{14}$$

This is the reference which will demodulate the optical signal modulated at the Larmor beat frequency of two nuclei (and the PEM) to ultimately yield the NMR signal at audio frequencies. The two signals are mixed after the first amplification stage of the receiver yielding (with extraneous sidebands not shown)

$$\omega = 30\text{ MHz} + \Delta \qquad (15)$$

which is then passed through the IF stage of the receiver and filtered to yield the audio NMR frequency Δ. This is the basis for the detection of real-time optically detected NMR. It has been observed that the noise contribution of the NMR spectrometer is insignificant compared to the noise contribution of the laser [10].

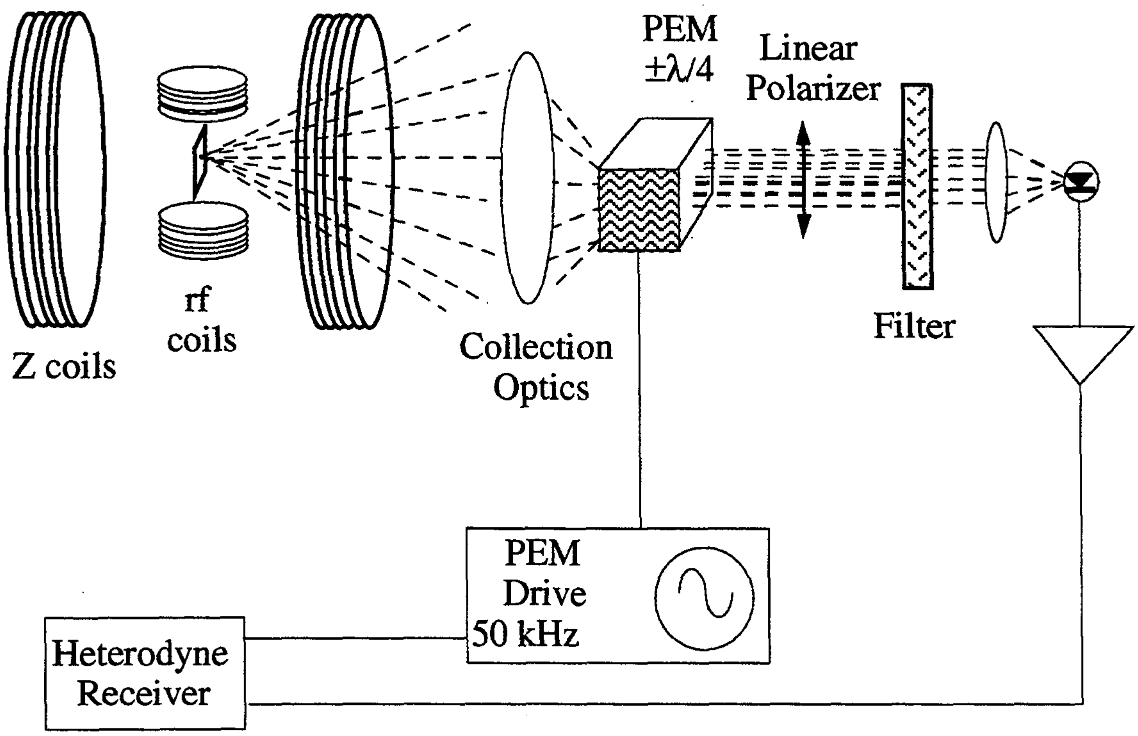

Figure 8. Schematics of the detection of optical signals modulated at rf frequencies.

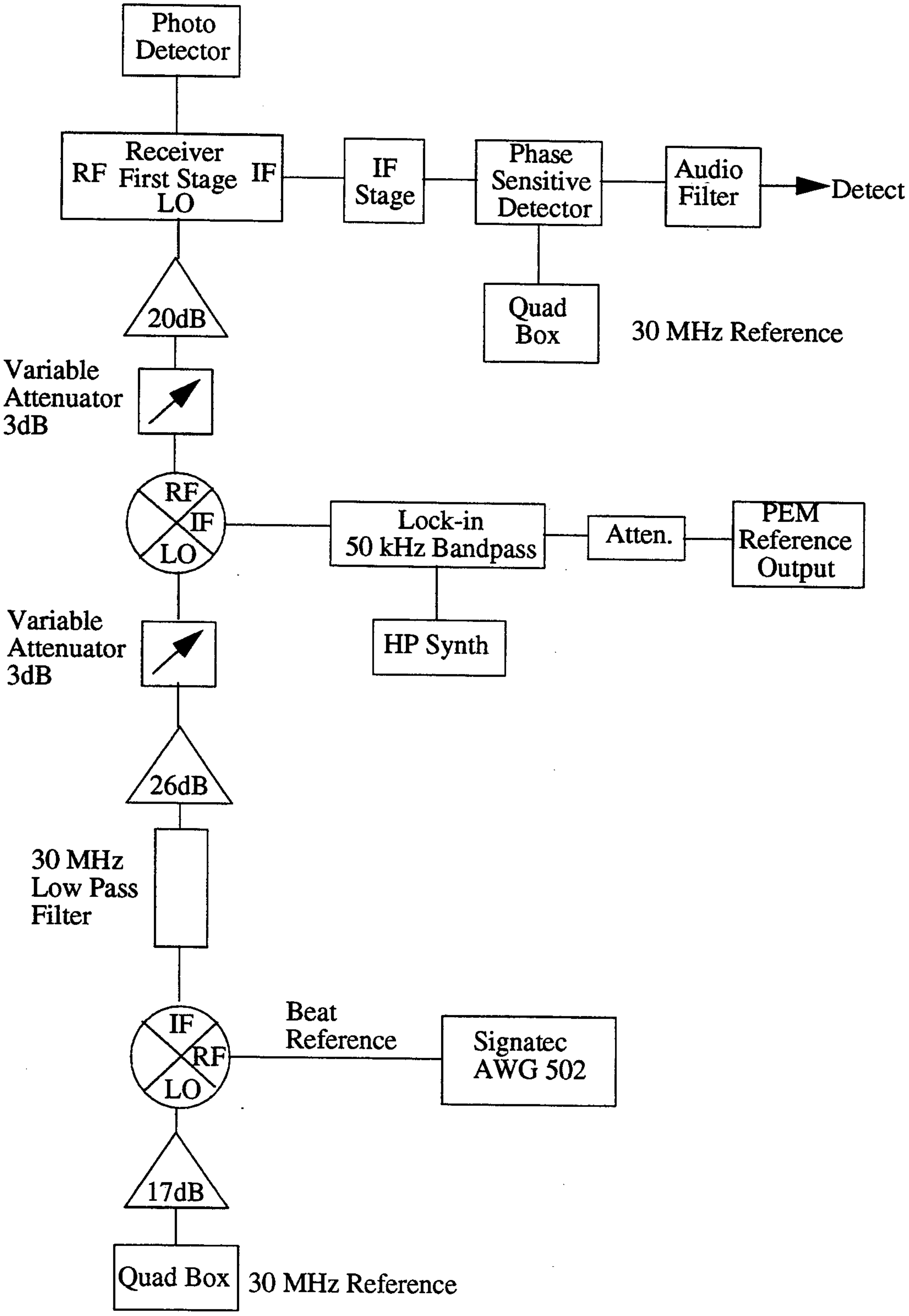

Figure 9. Schematic of the detection circuit for rf detection of ODNMR.

4.6 References

[1] Buratto, S.K., Shykind, D.N., and Weitekamp, D.P., *Can Nuclear Magnetic Resonance Resolve Epitaxial Layers?,* Journal of Vacuum Science and Technology B, **10**, 1740 (1992).

[2] Yuan, Y.R., Pudensi, M.A.A., Vawater, G.A., and Merz, J.L., *New Photoluminescence Effects of Carrier Confinement at an AlGaAs/GaAs Heterojunction Interface,* J. Appl. Phys., **58**, 397 (1985).

[3] Ossau, W., Bangert, E., and Weimann, G., *Radiative Recombination of a 3D-Electron with a 2D-Hole in P-Type GaAs/(GaAl)As Heterojunctions,* Solid State Communications, **64**, 711 (1987).

[4] Paget, D., Lampel, G., Sapoval, B., and Safarov, V.I., *Low Field Electron-Nuclear Spin Coupling in Gallium Arsenide Under Optical Pumping Conditions,* Phys. Rev. B, **15**, 5780 (1977).

[5] Rose-Innes, A.C., *Low Temperature Techniques* (D. Van Nostrand Company, Inc., Princeton, 1964).

[6] Bird, R.B., Stewart, W.E., and Lightfoot, E.N., *Transport Phenomenon* (John Wiley and Sons, New York, 1960).

[7] Garwin, R.L., Rev. Sci. Instrum., **27**, 826 (1956).

[8] Shykind, D.N., *personal communication,* 1993.

[9] The magnet was designed and constructed by D.N. Shykind of Quantum Magnetics.

[10] Carson, P.J., *personal communication,* 1993.

Chapter 5: Real Time Optically Detected NMR

The rotating-wave approximation for linearly polarized rf was found to break down at the high rf powers necessary to implement multiple-pulse line-narrowing sequences in the 77 K TSONMR spectrometer. This was a direct consequence of the low external magnetic field (115 G) used in the TSONMR spectrometer. The construction of the liquid helium cryostat described in chapter 4 with superconducting magnets capable of achieving fields of 0.4 T has solved this problem. Performing experiments at 2 K allows the observation of ODNMR of the well-resolved luminescence band (the H-band) in a GaAs/$Al_xGa_{1-x}As$ (x = 0.36) heterojunction. Low resolution ONMR of this system has been reported by Krapf and co-workers using the usual steady-state methods [1]. Our attempts to implement TSONMR were hampered by the long ONP (~ 10 min) times at these low temperatures. For comparision, T_1 of a bulk sample in the absence of light at 1.7 K and 6 kG is in excess of an hour [2]. For liquid helium hold-times of 8 hours, the long relaxation time makes the implementation of TSONMR described in chapter 3 impractical, at least for the more slowly relaxing sites. This restriction has now been lifted with the introduction of real-time optically detected NMR. By adding a circularly polarized reference field, the vector sum field (reference plus signal) is modulated at the difference frequencies of its Fourier components. This allows the real-time radio frequency modulation of the luminescence polarization by the nuclear field in an extension of the Hanle effect. This chapter describes the development of this new technique.

5.1 Experiment

Recent advances in MBE have allowed the fabrication of novel semiconductor nanostructures. The high sensitivity of ODNMR has allowed other workers to obtain NMR spectra of GaAs/AlGaAs heterojunctions [1] and GaAs/AlGaAs quantum wells [3,4]. However, the steady-state NMR experiment used gave excessive linewidths as it has in other samples for 25 years [1,5]. The motivation for constructing the new optical cryostat (chapter 4) was to apply TSONMR experiments at 2 K with larger magnetic fields to provide improved resolution and to allow the application of NMR multiple-pulse line-narrowing sequences. To facilitate the extension of TSONMR to new NMR experiments, a high quality sample with a small Hanle width and large nuclear fields was needed. A GaAs semiconductor heterojunction was selected based on a sample used by Krapf and co-workers [1].

5.1.1 Sample Characterization

The GaAs/AlGaAs heterojunction was provided by the JPL microdevices fabrication laboratory. Figure 1 is an illustration of the composition of the p-channel heterojunction. The substrate is semi-insulating GaAs with a 2500 nm layer of undoped GaAs, followed by a 6.5 nm undoped $Al_xGa_{1-x}As$ spacer (x = 0.36). The 30 nm p-type $Al_xGa_{1-x}As$ (x = 0.36) layer is doped with $6 \times 10^{17}/cm^3$ of Be, followed by 21 nm of undoped GaAs.

A photoluminescence (PL) spectrum of heterojunction sample M303 heterojunction is shown in figure 2, taken with the apparatus described in chapter 3. The luminescence peaks at 825 and 830 nm are attributed to the H-band, respectively denoted the *e* and *d* line, found only in p-channel heterojunctions [6,7]. The *e*-line and d-line have been assigned to the recombination of an interfacial 2D heavy hole sub-band with a 3D free electron and with a donor bound electron, respectively.

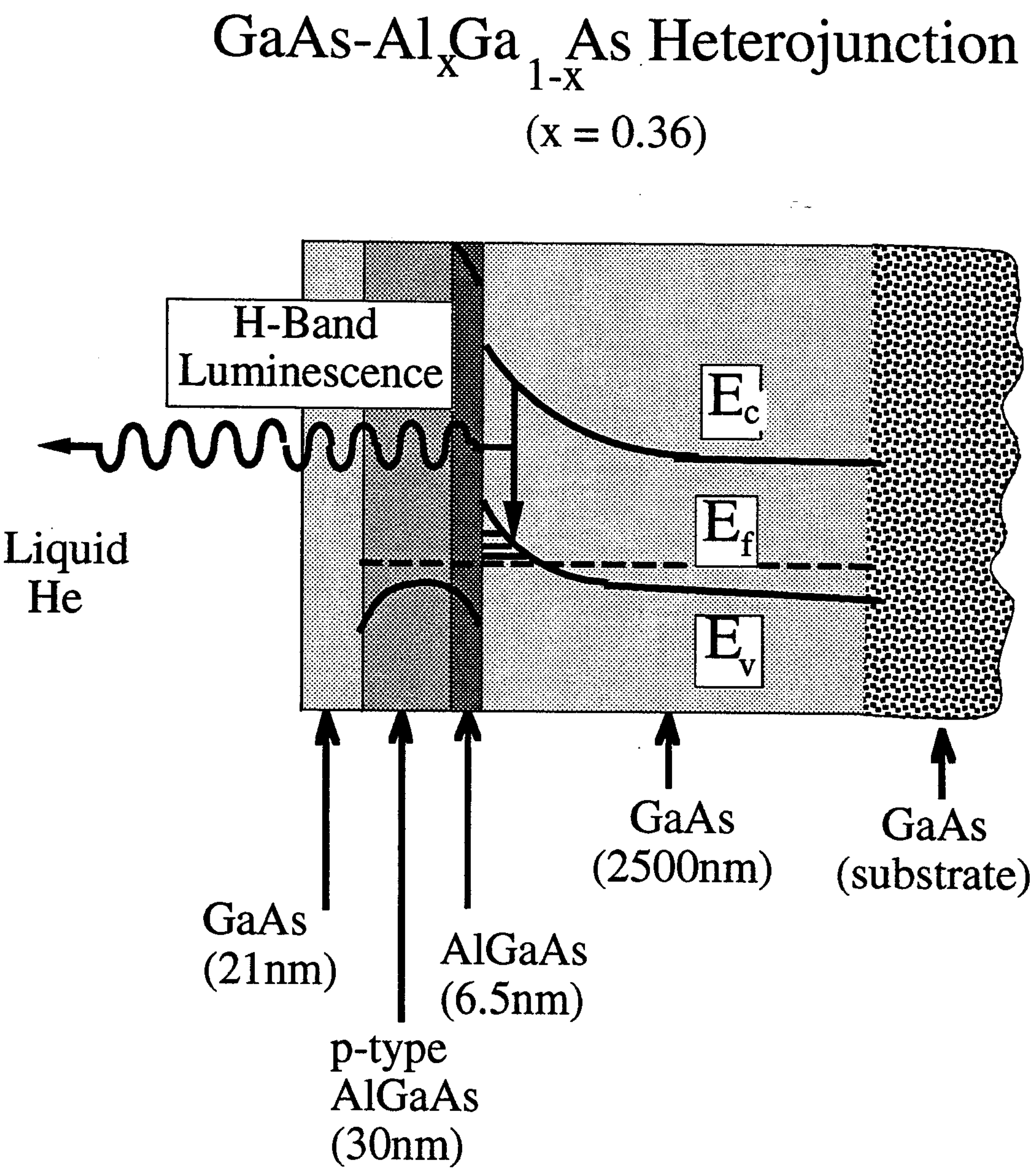

Figure 1. A schematic of the heterojunction structure [8].

The 830 nm line is more pronounced in our sample, compared to published spectra by Ossau and co-workers [6], and has been hypothesized to be the result of carbon impurities [9]. The sharp peak at 818 nm is attributed to excitonic luminescence lines [10].

Hanle-curve measurements were performed in the presence of nuclear fields with the exciting light transverse to the magnetic field. For magnetic fields much larger than

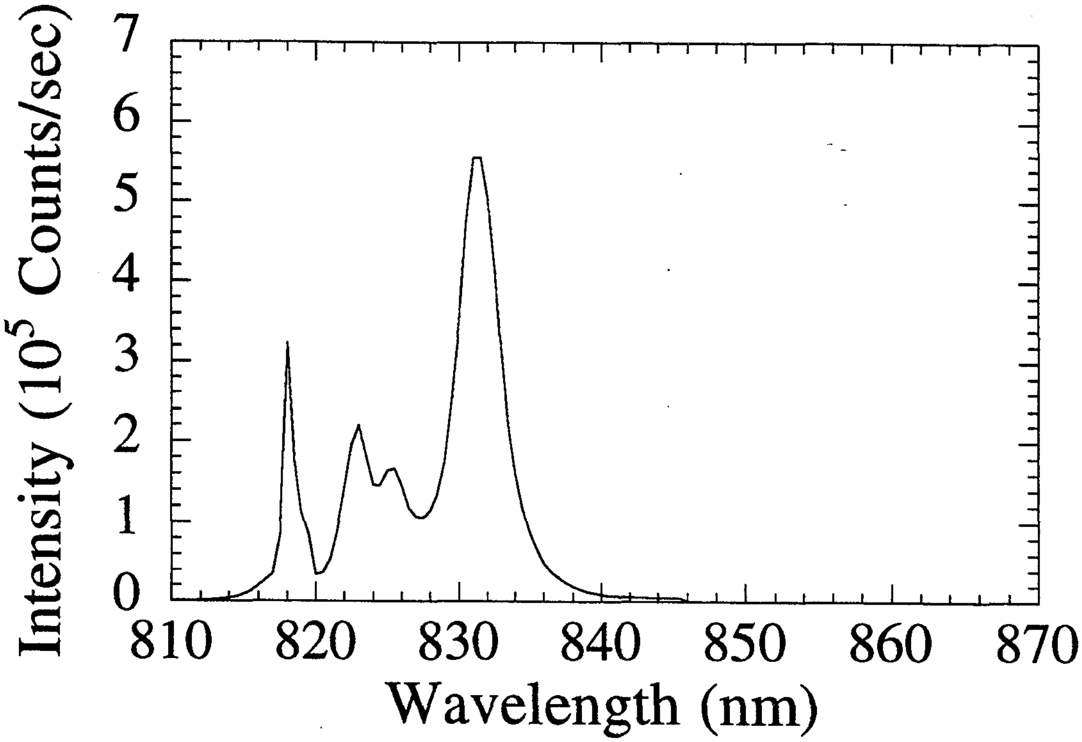

Figure 2. The PL spectrum of sample M304, a GaAs/AlGaAs heterojunction [11].

the electron fields b_e ($b_e \approx 5$ G [12]), this measurement should yield an approximate value of the Hanle width when the external magnetic field is exactly transverse to the excitation axis (chapter 3). These measurements yield a value of approximately 9 ± 1 mT. The value is approximate because the transverse magnetic fields were not calibrated since being moved from the original TSONMR apparatus. Krapf and co-workers measured the Hanle width of the H-band of a similar heterojunction with a time-dependent polarization of the exciting light to minimize nuclear effects [10]. Their data was best fit to a sum of two Lorentzians which indicates the presence of the two separate luminescence lines in this band. The measured half-widths of the two Lorentzians are 16.6 and 4.3 mT, and if the data is fit by one Lorentzian, the best fit yields 11 mT, approximately equal to our measured value.

The longitudinal magnetic field dependence of the circular polarization ρ is shown in figure 4. The decrease of ρ at large magnetic fields is attributed to the exciting light being off axis by 10 degrees from the longitudinal magnetic fields. From these measurements, it was observed that the total luminescence increased with magnetic field. This has been previously observed and hypothesized to be due to the mixing of heavy-hole and light-hole states for excited sub-bands in a magnetic field which relaxes selection rules relative to the nondegenerate bandstructures [6]. The total luminescence was found to increase approximately 20 percent as the field was increased from 0 to 0.4 T.

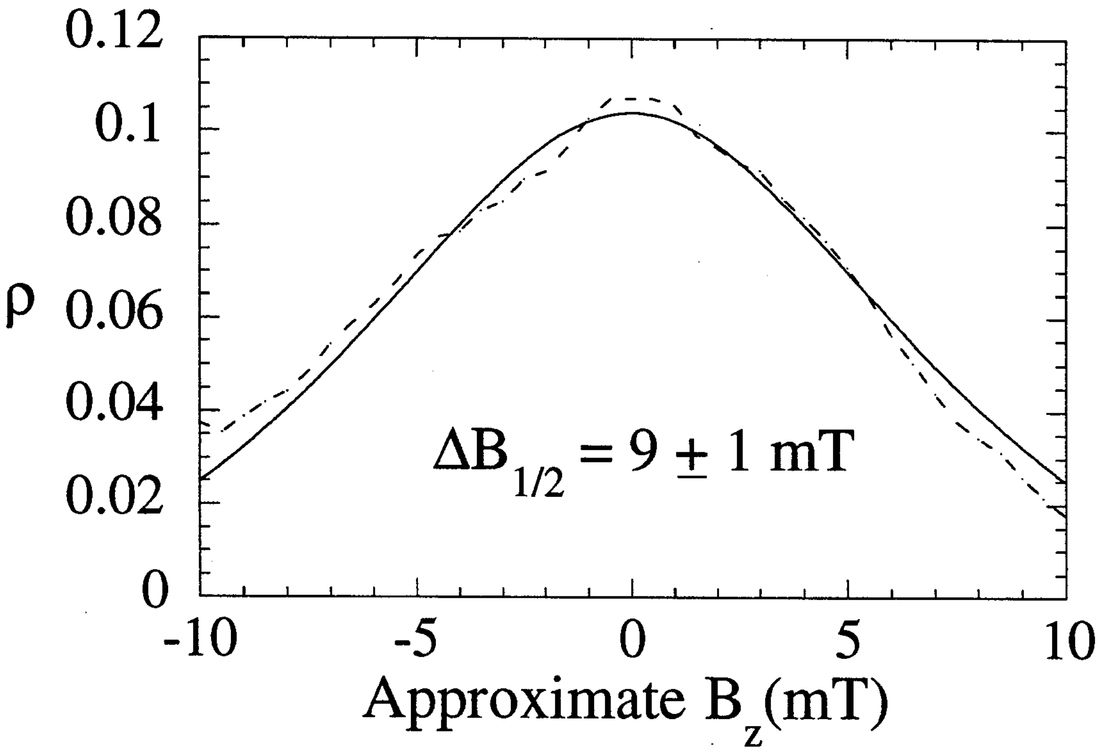

Figure 3. Hanle curve measurement of H-band luminescence with the exciting light perpendicular to the external magnetic field.

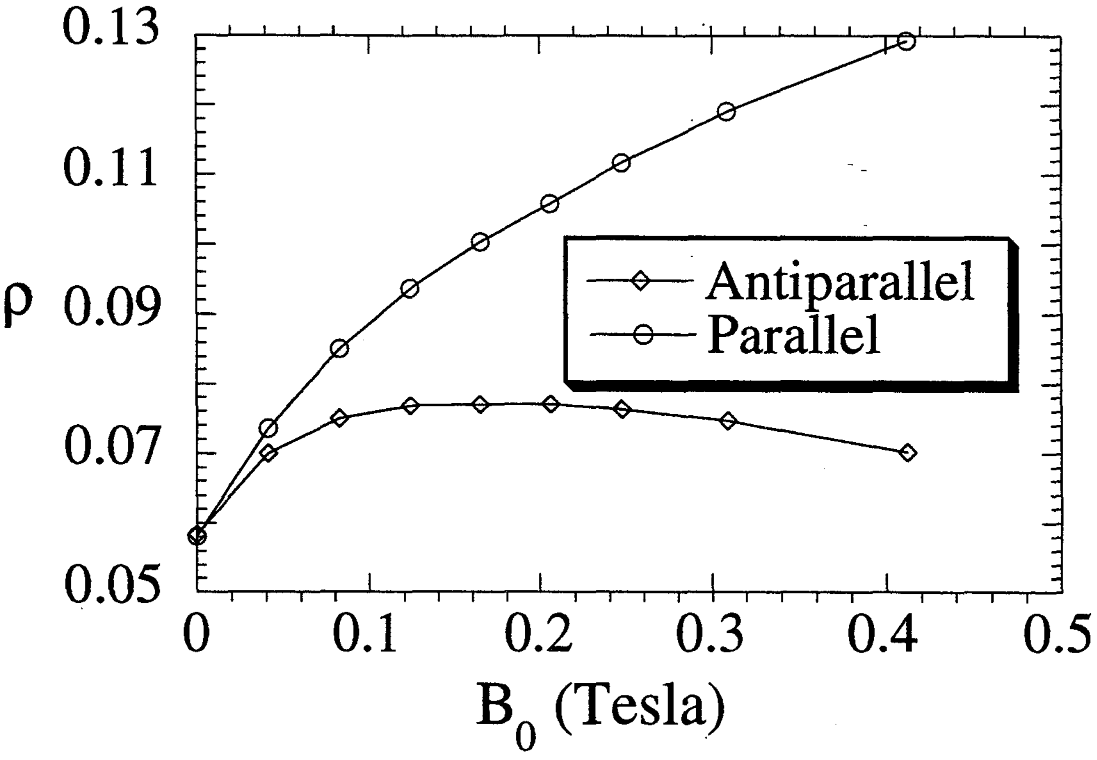

Figure 4. Longitudinal magnetic field dependence of the luminescence polarization.

5.1.2 Preliminary Studies

The experimental apparatus was described in the previous chapter. The initial observation of optically detected NMR was obtained with adiabatic rapid passage and lock-in detection of ρ. For these experiments, the value of B_1 was unknown. Nutation experiments (chapter 2) were unsuccessful at this time, since B_1 was estimated to be < 0.5 mT at the power used (< 200 Watts).

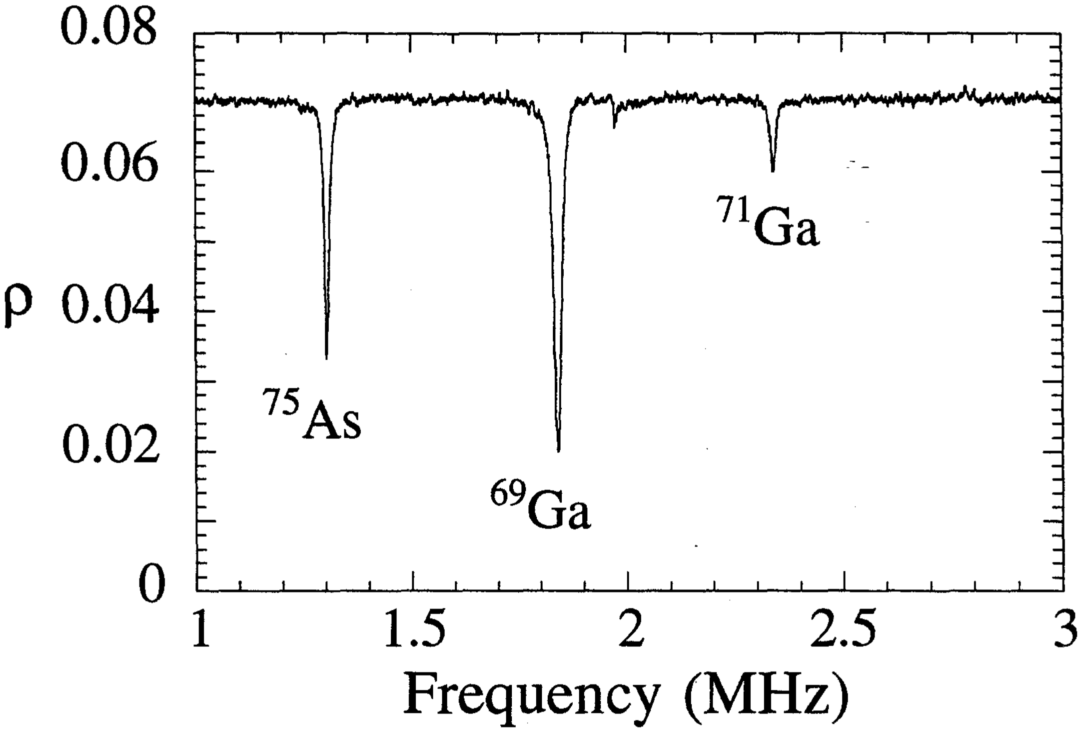

Figure 5. Adiabatic rapid passage with frequency sweep acquired with 1 scan lasting 10 seconds.

Figure 5 is the quasi-steady-state ONMR spectrum obtained for the GaAs heterojunction at 2 K. The spectrum of the three principle isotopes was obtained in a single frequency sweep lasting 10 seconds with lock-in detection (30 msec time constant). The polarization of the luminescence was simultaneously digitized with a Nicolet digital oscilloscope (model 4094A). Figure 6 shows a cw-TSONMR experiment attempted with a repetition rate of 2 min per point. The ^{71}Ga NMR signal is present at 155 kHz, but there is a large drift of the baseline comparable to the time of the experiment (30 min). The dependence of signal intensity on optical nuclear polarization time is plotted in figure 7. A fit of the data suggests an ONP time constant of approximately 10 minutes. These results highlight the limitations of the point-wise acquisition of an NMR transient in TSONMR. Each NMR transient would require a 20 minute delay period between points

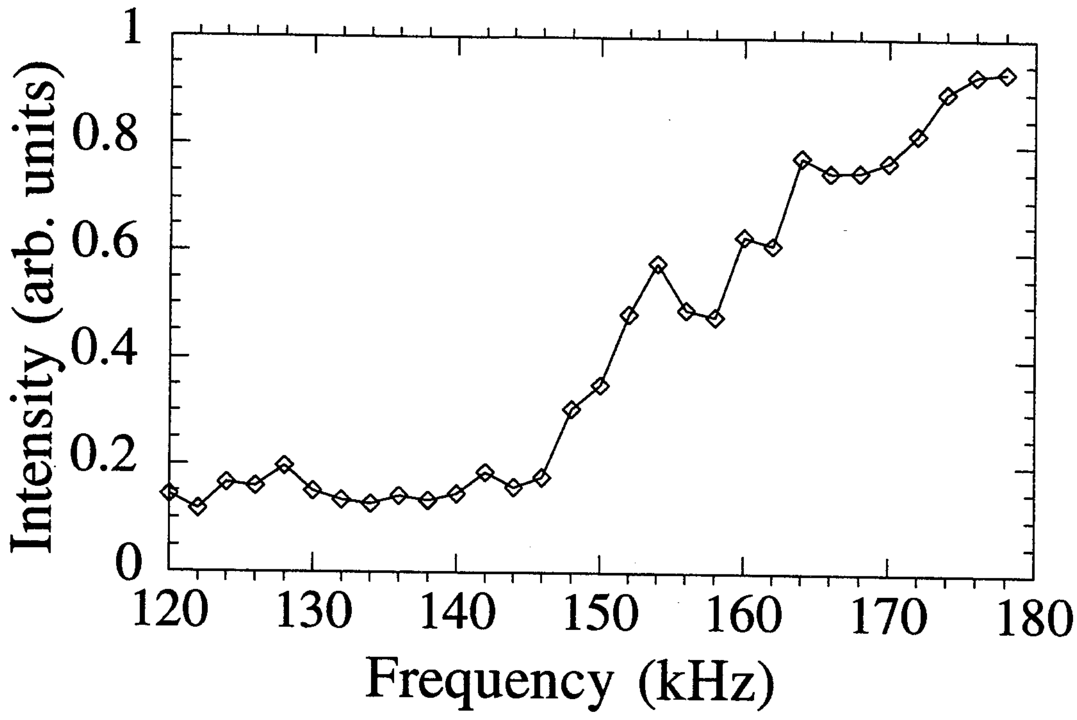

Figure 6. CW-TSONMR experiment.

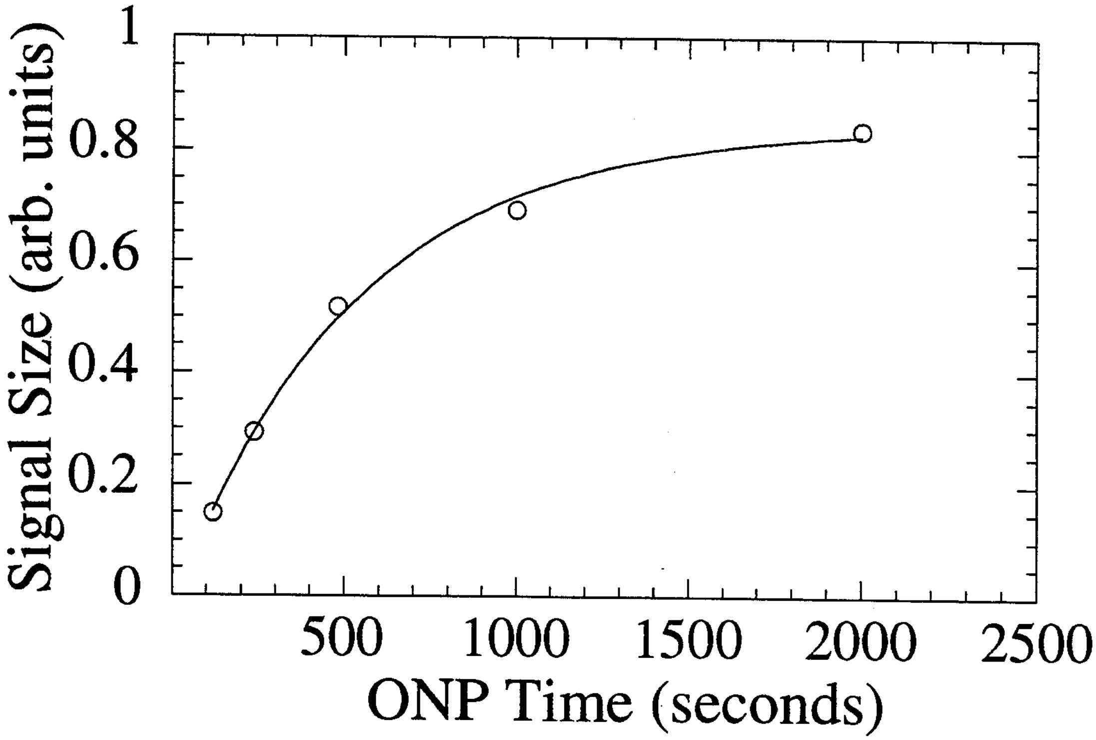

Figure 7. Integrated rapid passage signal strength versus ONP time. The data can be fitted with an exponential time constant of 525 seconds.

so that a complete transient would require an excessive amount of time. This inspired the quest for real-time optically detected NMR.

5.2 Real-time Optically Detected NMR

In ODNMR, for parallel detection axis and static field axis, the free precession of nuclear magnetization is not detectable by the Hanle effect because ρ is independent of the orientation of magnetization in the transverse plane. The basis of the real-time optically detected NMR described here is the modulation of the total transverse magnetization by interference of a signal field with an rf reference field, enhanced by spin-locking a different "reference" isotope. It is easiest to visualize the experiment in the rotating frame of the reference field $\vec{B}_N^{ref}$. The exciting light is parallel to the external magnetic field $\vec{B}_0$, and the transverse magnetization of nucleus "sig" is precessing with the difference frequency $\omega_{ref} - \omega_{sig}$ about the z-axis. The modulation of ρ depends only on the magnitude of the total

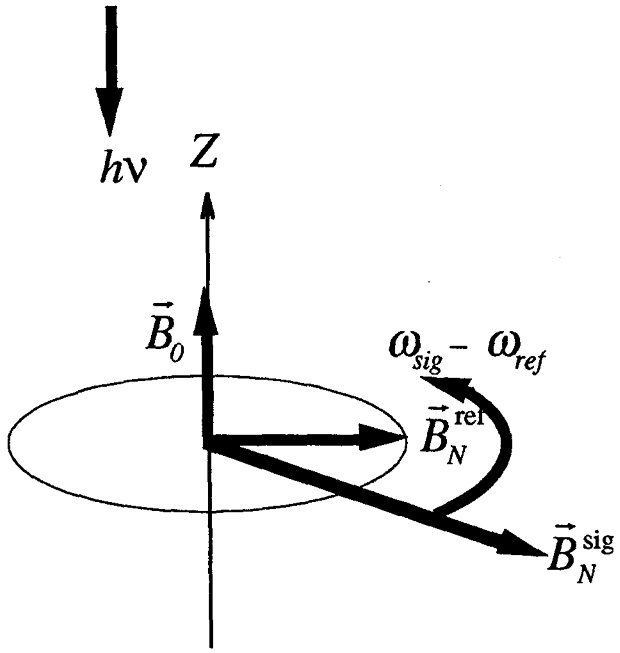

Figure 8. Illustration of rf beat detection of transverse magnetization.

transverse magnetization (sum of $\vec{B}_N^{ref} + \vec{B}_N^{sig}$) which will be modulated at the difference frequency. The steady-state cw response of nucleus "ref" is used as the reference $\vec{B}_N^{ref}$. The transverse nuclear fields to be detected, $\vec{B}_N^{sig}$ is created with the application of a π/2 pulse. The resulting NMR transient is optically detected and demodulated by nearly the Larmor beat frequency to audio frequencies with a heterodyne receiver (chapter 4). The Fourier transform of the resulting transient will yield the FT-NMR spectrum.

5.2.1 Theory

The precession of the electrons is described as a Bloch precession about the total field, which is the sum of both external and nuclear fields. Since the precession frequencies and relaxation rate for the electrons are three orders of magnitude larger than for nuclear spins, the evolution of the electron spins in the total magnetic field will reach steady state before the nuclear spins reorient appreciably. This adiabatic approximation is the basis for the steady-state approximation used in the solution of the Bloch equations for the electron motion about the total field $\vec{B}$. To lend coherence to the discussion of the various experiments, the basis of this effect will first be discussed.

The phenomenological equations of Bloch assume that the change in the magnetic moment of a spin S is subject to the sum of decay processes back to equilibrium with time constant T_{1e}, and the torque exerted on the magnetic moment $g^*\mu_B\vec{S}$ by the total magnetic field $\vec{B}_T$ (eq. 1).

$$\frac{d}{dt}\vec{S} = -\frac{1}{T_{1e}}(\vec{S}-\vec{S}_0) - \frac{g^*\mu_B}{\hbar}(\vec{S}\times\vec{B}_T) \tag{1}$$

where g^* is the electron g factor, μ_B is the Bohr magneton, and $\vec{B}_T = \vec{B}_N + \vec{B}_0$ is the total contribution of both nuclear and external fields. The steady-state solution is

$$B_H(\vec{S}-\vec{S}_0) = (\vec{B}_T \times \vec{S}) \tag{2}$$

where $B_H = \dfrac{\hbar}{g^*\mu_B T_{1e}}$ is the Hanle width.

Solving for S using common vector identities [13], we obtain

$$\vec{S} = \frac{B_H^2\vec{S}_0 + (\vec{S}_0 \bullet \vec{B}_T)\vec{B}_T + B_H(\vec{B}_T \times \vec{S}_0)}{B_H^2 + B_T^2} \tag{3}$$

This relationship was originally derived by Merkulov and Fleischer [14]. The resulting polarization is detected along the $\vec{n}$ axis by monitoring the polarization of the luminescence

$$\rho = -2C(\vec{n} \bullet \vec{S}) \tag{4}$$

where C (= 1/2 or 1) depends on the optical selection rules. If these equations are solved for a magnetic field perpendicular to the detection axis, the resulting equation is the complete Hanle effect

$$\rho = \rho_0 \frac{1}{1+\left(\frac{B_\perp}{B_H}\right)^2} \tag{5}$$

where $B_\perp$ is the magnitude of the magnetic field transverse to the optical axis. Here $\rho_0 = -2CS_0$, the steady-state luminescence polarization in the absence of transverse nuclear fields. When the magnetic field is oblique, the incomplete Hanle effect results. The resulting equations are similar to those describing the complete Hanle effect, but the Hanle width B_H is substituted with an "incomplete Hanle width" $A_H = \sqrt{B_H^2+B_n^2}$. This situation is the one encountered in ODNMR experiments.

$$\rho = S_0 \frac{1}{1+\left(\frac{B_\perp}{A_H}\right)^2} \tag{6}$$

The innovation of real-time optically detected NMR described here involves introducing a time-dependence to $B_\perp$ by the addition of a reference field so that the vector sum field (reference field plus nuclear field of interest) is modulated at the difference frequencies of its Fourier components.

5.2.2 Zeeman Beat Experiment

In the Zeeman beat experiment, the time dependence of $B_N(t)$ is imparted to ρ by the application of an additional rf field which is enhanced by spin locking a heteronucleus. This section reviews a quantitative theory [15] relating the observable Fourier components of ρ to the nuclear fields of two isotopes, which are manipulated by NMR. Taking into account miscellaneous nuclear fields B_N^{misc} along the z-axis which add to $\vec{B}_0$ for optical pumping parallel to $\vec{B}_0$ gives

$$\rho = \rho_0 \left\{ \frac{1}{1+\left(\frac{\left(B_N^{tot}(t)\right)^2}{B_H^2 + \left(B_0 + B_N^{misc}\right)^2} \right)} \right\} \tag{7}$$

where

$$\left(B_N^{tot}(t)\right)^2 = \left(B_N^{sig}(t)\right)^2 + \left(B_N^{ref}(t)\right)^2 + 2B_N^{sig}(t)B_N^{ref}(t)cos(2\pi f_{12}t) \tag{8}$$

is the square of the magnitude of the vector sum of the two nuclear fields B_{N1} and B_{N2} computed from the law of cosines,

$$\rho_0 = \rho\left(B_N^{tot} = 0\right) \tag{9}$$

and f_{12} is the Larmor beat frequency. Substituting equation 8 into equation 7, we get

$$\rho = \rho_0 \left\{ \frac{B_H^2 + \left(B_0 + B_N^{misc}\right)^2}{B_H^2 + \left(B_0 + B_N^{misc}\right)^2 + \left(B_N^{tot}\right)^2} \right\} \tag{10}$$

If dimensionless nuclear fields

$$b_N^{ref} = \frac{B_N^{ref}}{\sqrt{B_H^2 + \left(B_0 + B_N^{misc}\right)^2}}$$
$$b_N^{sig} = \frac{B_N^{sig}}{\sqrt{B_H^2 + \left(B_0 + B_N^{misc}\right)^2}} \tag{11}$$

are introduced, then Eq. 10 can be rewritten as

$$\rho = \rho_0 \frac{1}{1+\left(b_N^{ref}\right)^2 + \left(b_N^{sig}\right)^2 - 2b_N^{ref} b_N^{sig} \cos\left(2\pi f_{12} t\right)} \tag{12}$$

This can be simplified by separating out the rapid time dependence by using the following substitutions

$$\alpha = \frac{2b_N^{ref} b_N^{sig}}{1+\left(b_N^{ref}\right)^2 + \left(b_N^{sig}\right)^2}$$
$$\beta = b_N^{ref} - b_N^{sig} \tag{13}$$

resulting in the final expression

$$\rho = \rho_0 \frac{1}{1+\beta^2}\left(\frac{1-\alpha}{1-\alpha \cos\left(2\pi f_{12} t\right)}\right) \tag{14}$$

The value of α is restricted to the values $-1 < \alpha < 1$. The Hanle effect from the magnitude difference is the major effect and the rapid time dependence is contained in the second term. The rapid time-dependence near the beat frequency between two nuclei can be represented by the function $f(t)$ where

$$f(t) = \left\{\frac{1-\alpha}{1-\alpha \cos(2\pi f_{12} t)}\right\} \tag{15}$$

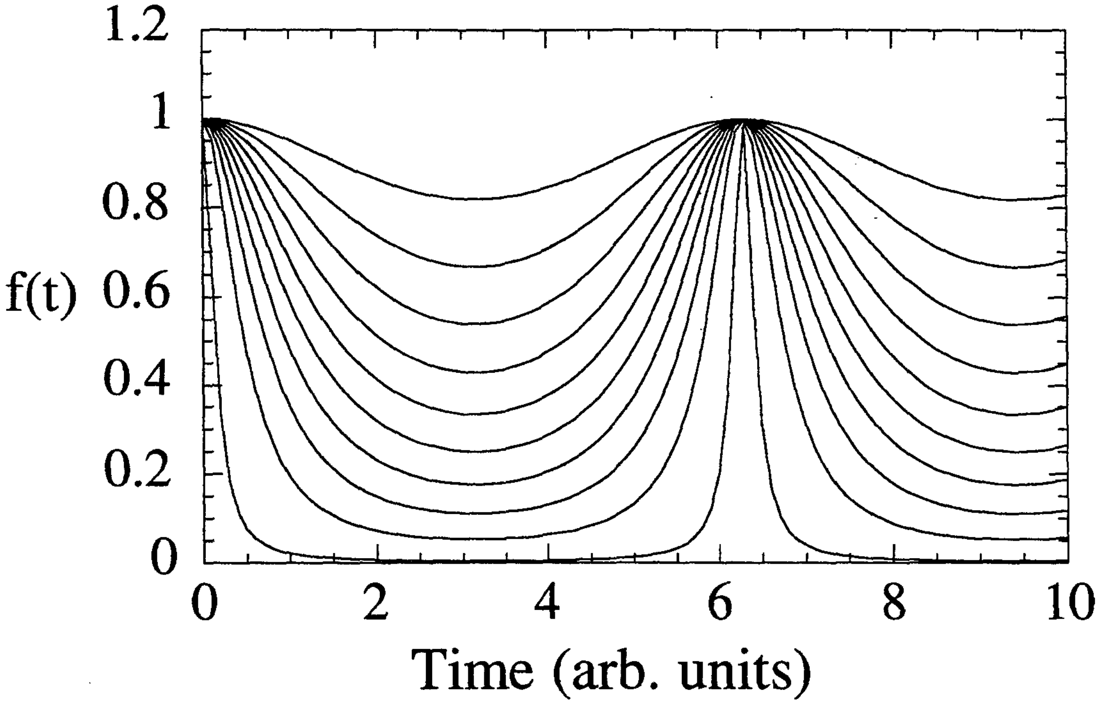

Figure 9. Time dependence of $f(t)$ as a function of the modulation factor α. From top to bottom, the values of α are 0.1,0.2,0.3, 0.4, 0.5, 0.6, 0.7, 0.8, 0.9, 0.99.

The time-dependence of $f(t)$ is shown in figure 9. For small modulation factors, the response of the system is linear [15]. As the modulation factor α gets larger, there is a saturation of the Hanle effect so that small changes in the transverse magnetic field do not have a significant effect. In the limit of $\alpha \to 1$, the resulting time-dependence is described by equally spaced delta functions. Typically, only the first Fourier component of the time-domain signal will be detected. The Fourier components at frequencies in a narrow audio band about harmonics of f_{12} is computed to be

$$\hat{\rho}(f + mf_{12}) = \rho_0 \int_0^\infty dt\; e^{2i\pi ft} A^{(m)}(t) \tag{16a}$$

where

$$A^{(m)}(t) = \frac{1}{1+\beta(t)^2}\sqrt{\frac{1-\alpha(t)}{1+\alpha(t)}}\left(\frac{1-\sqrt{1-\alpha(t)^2}}{\alpha(t)}\right)^m \tag{16b}$$

using the assumption that b_N^{ref} and b_N^{sig} change slowly compared to the Larmor beat period $1/f_{12}$, with $f << f_{12}$ as written. Setting $b_N^{ref} = b_N^{ref}(0)$ and assuming $b_N^{sig} << 1$, the Fourier components near the Zeeman beat frequency (m = 1) are seen to be linear in $b_N^{sig}(t)$

$$\hat{\rho}(f + f_{12}) = \rho_0 \int_0^\infty dt\, e^{2i\pi ft} \frac{b_N^{ref}(0)}{\left(b_N^{ref}(0)^2 + 1\right)^2} b_N^{sig}(t) + O\left(\left(b_N^{sig}\right)^3\right) \qquad (17)$$

This term is optimized for $b_N^{ref} = 1/\sqrt{3}$.

5.3 Results

Initial attempts to spin-lock the magnetization using pulsed NMR experiments were unsuccessful so it was necessary to resort to adiabatic half-passage experiments. Here spin-locking was achieved by stopping the frequency sweep on resonance, at which point B_{eff} is perpendicular to the external field and parallel to the magnetization. Figure 11 shows the depolarization of the luminescence resulting from this experiment on ^{71}Ga. The field is swept up 17 mT in 2 seconds, stopping at the Larmor frequency of 2.054 MHz. By performing this experiment on both ^{75}As and ^{71}Ga simultaneously, the first real-time optically detected NMR transient was observed (fig. 12). The amplitude modulation at the beginning of the transient is due to the overshoot past resonance of the field sweep, and the following return to resonance. These data indicate that there is a substantial steady-state response which persists for tens of seconds which is longer than the initial transient $T_{1\rho}$ observed in the DC-detected experiment (shown in fig. 11). The steady-state signal is not present when the rf frequency is far from resonance (not shown).

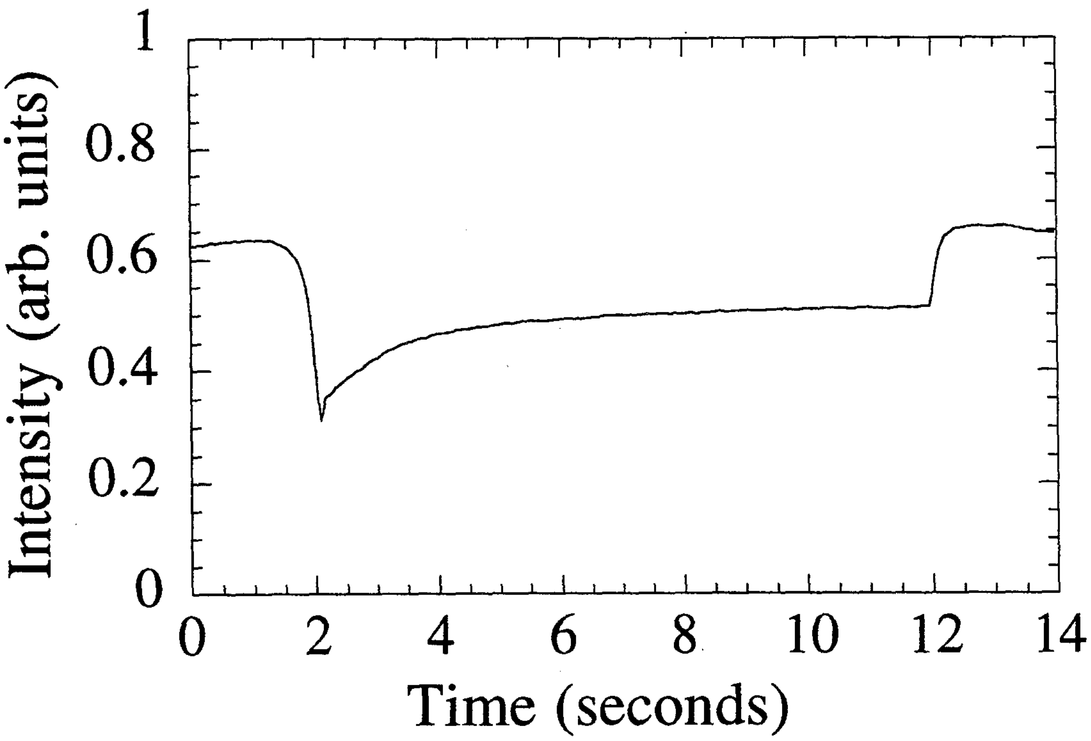

Figure 11. Field sweep spin lock of ^{71}Ga.

Further investigation indicated that turning the rf field on for both nuclei with no field sweep resulted in steady-state response (fig. 13). For all of the following rf transients, only one out of every 20 points digitized are plotted to aid in the visualization of the signal. Similar data could be obtained by changing the carrier of the demodulation frequency. The bandwidth for all of the following real-time optically detected NMR transients is 500 Hz.

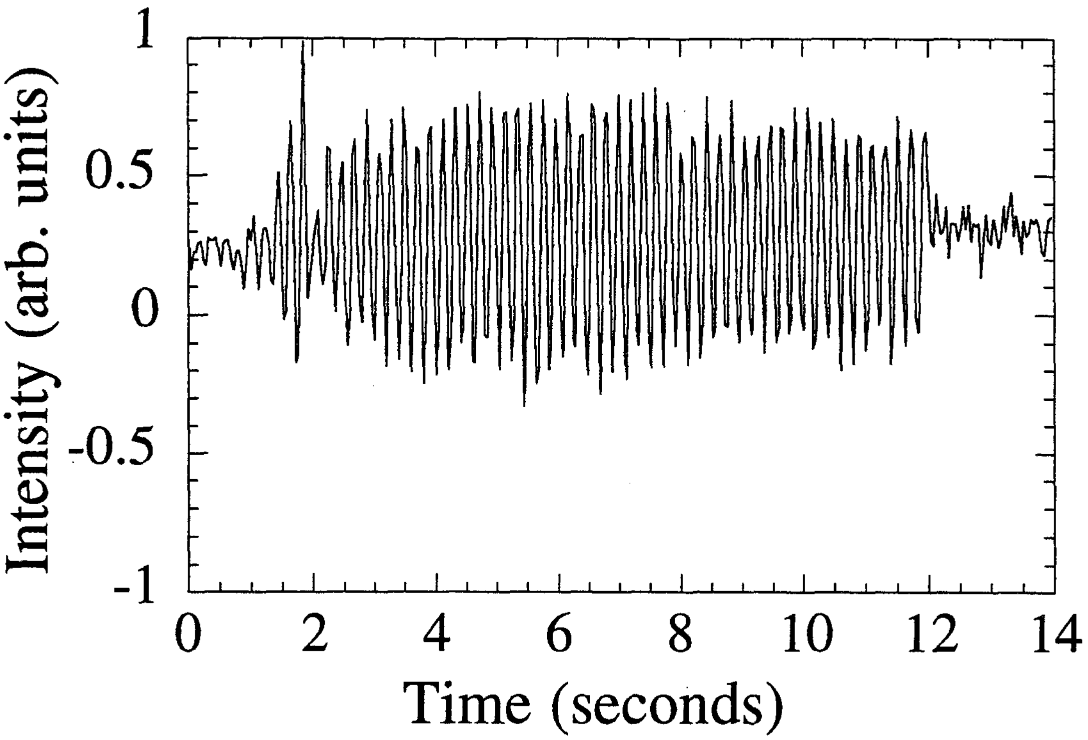

Figure 12 . RF-detected simultaneous adiabatic half-passage of ^{71}Ga and ^{75}As.

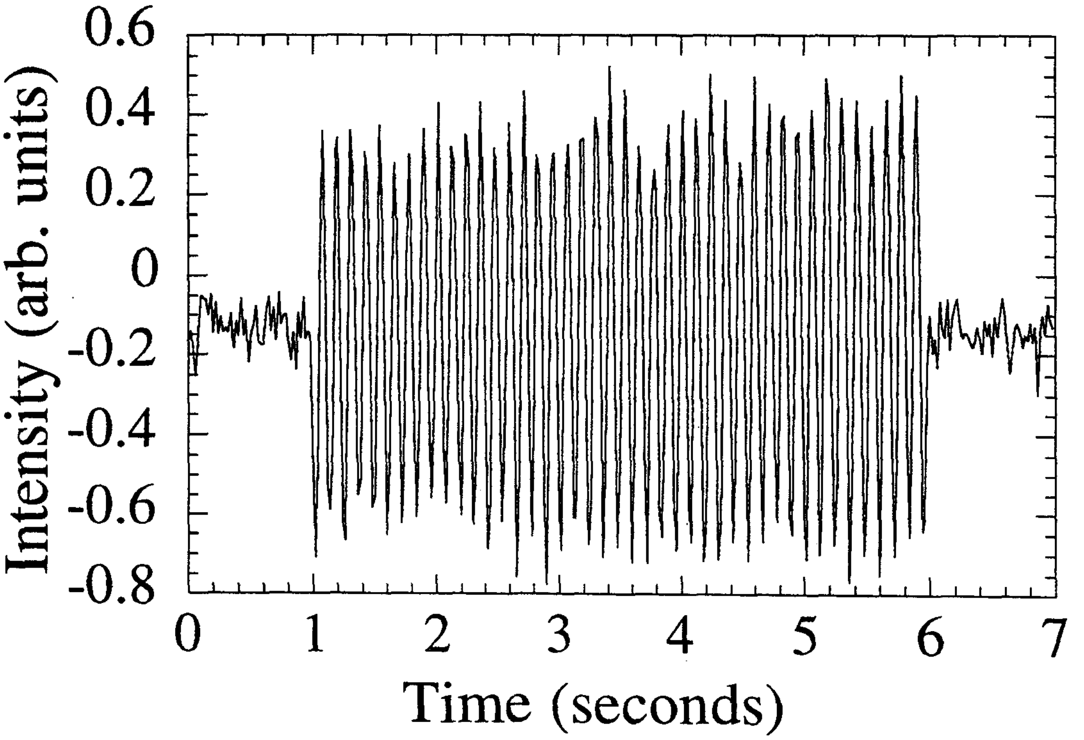

Figure 13. RF-detection of steady-state ^{71}Ga and ^{75}As response to rf.

With the incorporation of a larger rf amplifier (ENI 500A) and the redesign of the rf coils, pulsed NMR effects were observed, and the resulting B_1's were found to yield a $\pi/2$-time corresponding to 3 μsec ($B_1 = 6.5$ mT). A nutation transient was obtained pointwise by applying a nutation pulse followed by a spin-lock pulse on a single nuclei and detected as DC depolarization (fig. 14). The nutation pulse was incremented by 1 μsec for each repetition of the pulse sequence. The spin-lock pulse used a B_1 field of 0.65 mT to avoid overheating the rf coils. The DC signal, integrated over the duration of the spin-lock pulse (5 seconds) for each nutation pulse increment is shown in fig. 15 as a function of the nutation pulse length. For figure 15 and 16, only the difference ($I_+ - I_-$) is measured with the heterodyne NMR spectrometer used essentially as an audio lock-in detector. Here the spectrometer is demodulating the signal which possess a time dependence (at 50 kHz) only because the PEM in the polarization detection apparatus, but the measured luminescence polarization is the DC part of ρ. The first point of the data is normalized to equal the steady state value of ρ in the absence of rf fields.

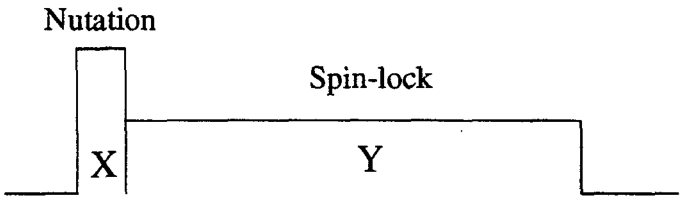

Figure 14. Nutation pulse sequence.

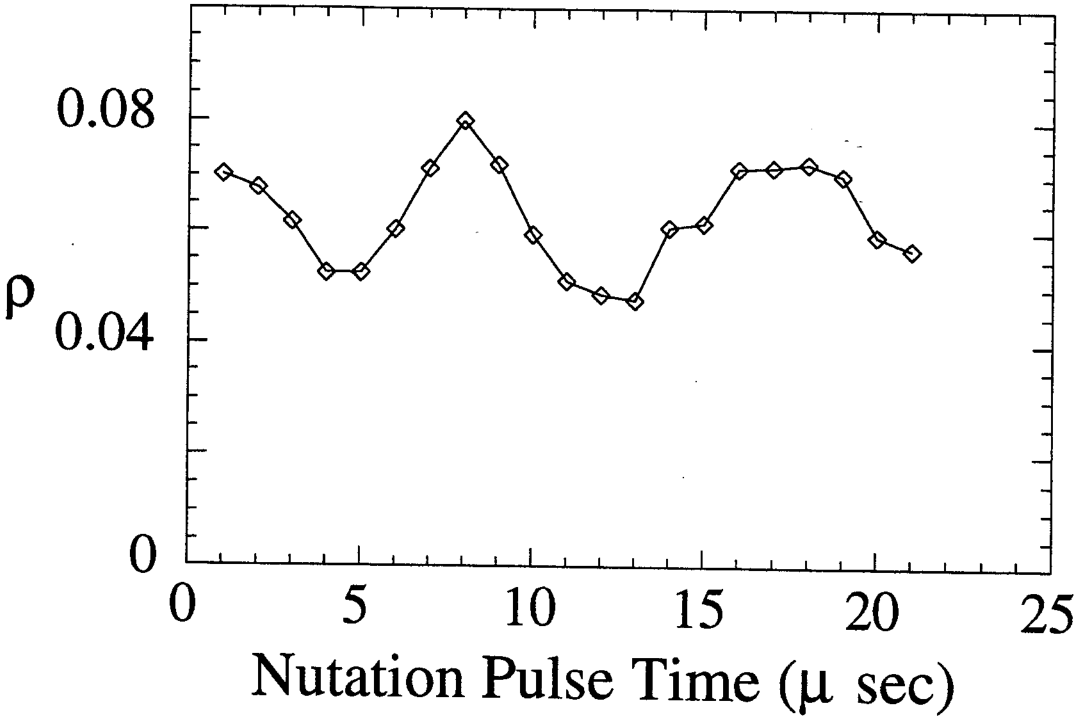

Figure 15. ^{71}Ga nutation experiment in the heterojunction.

It is important to note that fig. 15 represents the rectified nutation spectrum because Hanle detection can't distinguish between I_y and $-I_y$. Figure 16 shows a pulsed spin lock experiment with DC detection, i.e. one such transient of the sort from which Fig. 15 was constructed.

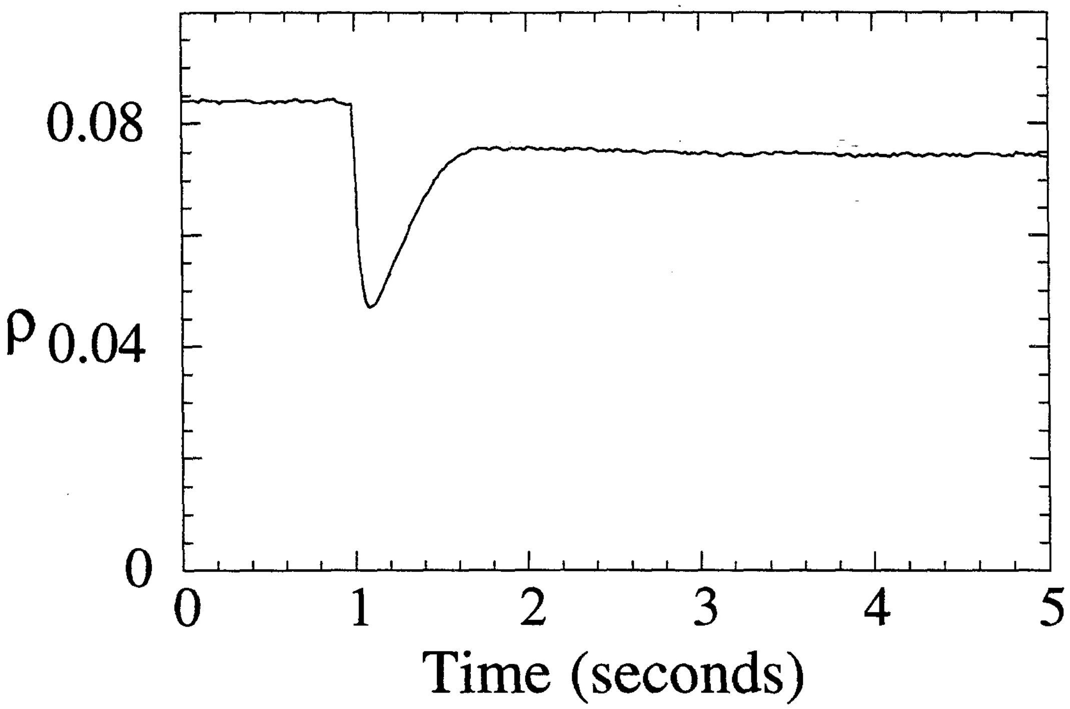

Figure 16. ^{71}Ga pulsed spin lock following a π/2 pulse.

Subsequent experiments on ^{75}As yielded a π/2 pulse time of 5 μsec which corresponds to the same B_1 field. This shows that the frequency response of the rf electronics is approximately flat across the frequency range used in the experiments.

When both nuclei are spin-locked following a π/2 pulse, the luminescence polarization oscillates at the Zeeman beat frequency which is demodulated by a heterodyne NMR spectrometer (fig. 17). At long times, the rf signal approaches a steady-state amplitude at a frequency equal to the Zeeman beat frequency. At short times, a null is observed which is hypothesized to result from spin locking the nuclear magnetization with opposite rf polarity. During the decay of the magnetization with time constant $T_{1\rho}$, the nuclear magnetization passes through 0 before reaching steady state in phase with the resulting rf-pulse.

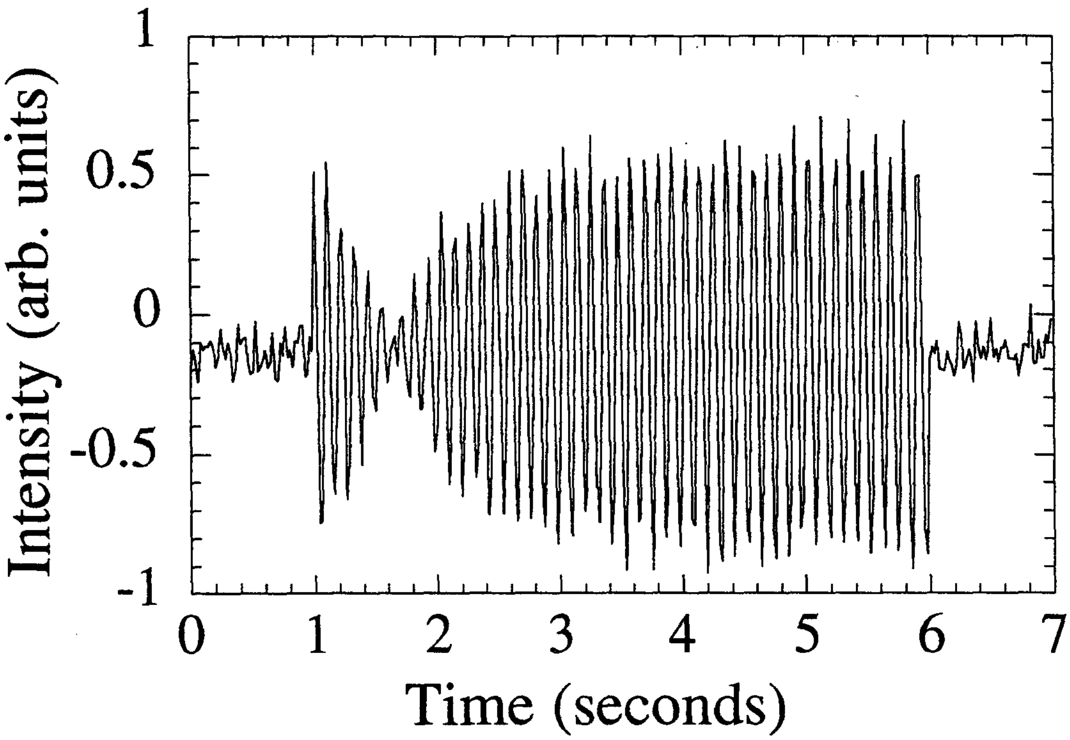

Figure 17. rf detected NMR with π/2 pulse preceding spin-lock.

Figure 18 was recorded with the same experimental conditions, but the π/2 pulse to the ^{71}Ga was replaced by a π/4 pulse. The resulting signal has a null in the signal which occurs at an earlier time. This is consistent with the fact that by applying a π/4 pulse, a smaller value of spin-locked magnetization is expected so that the zero crossing occurs sooner.

The results of these investigations show the feasibility of real-time optically detected NMR. The current experiments performed with a bandwidth of 500 Hz, resulting in signal to noise ratio of approximately 20. In FT-NMR experiments, typical bandwidths of 40 kHz are common. This will lead to a corresponding drop in the signal to noise (S/N) to approximately 1 to 2. Although a single shot experiment would be difficult to interpret, signal averaging could be performed to yield a high resolution spectrum. This would make the acquisition of a real-time optically detected FT-NMR spectrum feasible, and the preliminary results have been encouraging.

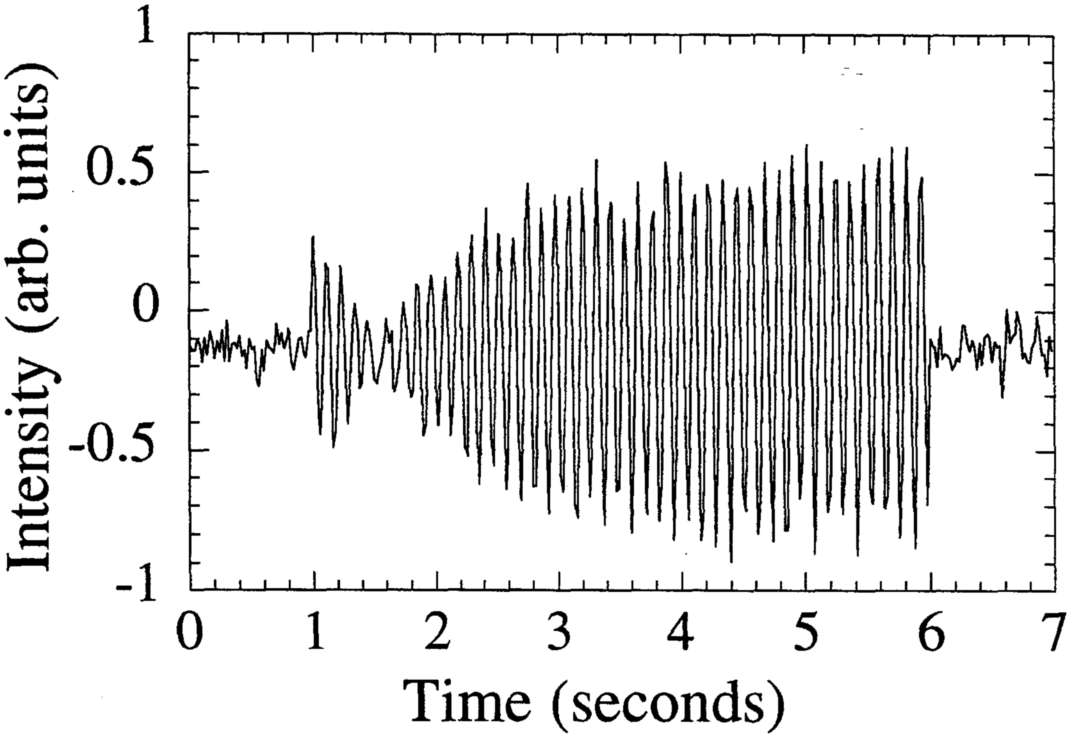

Figure 18. Rf detected pulsed spin lock signal following a π/4 pulse to ^{71}Ga.

5.4 Conclusion

After 25 years of research, the novel phenomenon of optical orientation in semiconductors is well understood. However, the widespread application of this technique has been hampered by the restriction of NMR to quasi-steady state methods. The culmination of this technique would be the full implementation of real-time optically detected FT-NMR for the study of semiconductor nanostructures. The acquisition of real-time optically detected spin-lock transients reported here represents a key step towards achieving this goal.

5.5 References

[1] Krapf, M., Denninger, G., Pascher, H., Weimann, G., and Schlapp, W., *Optically Detected Nuclear Magnetic Resonance and Knight Shift in* $Al_xGa_{1-x}As/GaAs$ *Heterostructures,* Solid State Communications, **78**, 459 (1991).

[2] Paget, D., *Optical Detection of NMR in High-Purity GaAs: Direct Study of the Relaxation of Nuclei Close to Shallow Donors,* Phys. Rev. B, **25**, 4444 (1982).

[3] Flinn, G.P., Harley, R.T., Snelling, M.J., Tropper, A.C., and Kerr, T.M., *Optically detected nuclear magnetic resonance of nuclei within a quantum well,* Semicond. Sci. Technol., **5**, 533 (1990).

[4] Kalevich, V.K., Korenev, V.L., and Fedorova, O.M., *Optical Polarization of Nuclei in GaAs/AlGaAs Quantum Well Structures,* JETP Letters, **52**, 349 (1990).

[5] *Optical Orientation*, edited by Meier, F., and Zakharchenya, B.P. (North-Holland, Amsterdam, 1984), Vol. 8.

[6] Ossau, W., Bangert, E., and Weimann, G., *Radiative Recombination of a 3D-Electron with a 2D-Hole in P-Type GaAs/(GaAl)As Heterojunctions,* Solid State Communications, **64**, 711 (1987).

[7] Yuan, Y.R., Pudensi, M.A.A., Vawater, G.A., and Merz, J.L., *New Photoluminescence Effects of Carrier Confinement at an AlGaAs/GaAs Heterojunction Interface,* J. Appl. Phys., **58**, 397 (1985).

[8] The sample was fabricated by J. Liu of the JPL microdevices laboratory in collaboration with F.J. Grunthaner.

[9] Ksendzov, A., *Personal Communication,* (1993).

[10] Krapf, M., Denninger, G., Pascher, H., Weimann, G., and Schlapp, W., *Optically Detected Conduction Electron Spin Resonance, Overhauser Shift and Nuclear*

Magnetic Resonance in p-GaAlAs/GaAs Heterostructures, Superlattices and Microstructures, **8**, 91 (1990).

[11] The PL was obtained by A. Ksendzov of the JPL microdevices fabrication laboratory in collaboration with F.J. Grunthaner.

[12] Paget, D., Lampel, G., Sapoval, B., and Safarov, V.I., *Low Field Electron-Nuclear Spin Coupling in Gallium Arsenide Under Optical Pumping Conditions,* Phys. Rev. B, **15**, 5780 (1977).

[13] Jackson, J.D., *Classical Electrodynamics* (John Wiley & Sons, New York, 1975).

[14] Fleisher, V.G., and Merkulov, I.A., *Optical orientation of the coupled electron-nuclear spin system of a semiconductor* (North-Holland, Amsterdam, 1984), 173.

[15] Marohn, J., *personal communication*, 1993.